MECHANICAL PROPERTIES OF FIBER LASER WELDED AND FRICTION STIR (SPOT)

WELDED LIGHTWEIGHT ALLOYS

by

MOHAMMED SHAFIUL HASIB CHOWDHURY

Bachelor of Science in Mechanical Engineering

Bangladesh University of Engineering and Technology (BUET)

Dhaka, Bangladesh, 7th October 2009

A thesis

presented to Ryerson University

in partial fulfillment of the

requirements for the degree of

Master of Applied Science

in the program of

Mechanical Engineering

Toronto, Ontario, Canada, 2012

© Mohammed Shafiul Hasib Chowdhury 2012

AUTHOR'S DECLARATION

I hereby declare that I am the sole author of this thesis. This is a true copy of the thesis, including any required final revisions, as accepted by my examiners.

I authorize Ryerson University to lend this thesis to other institutions or individuals for the purpose of scholarly research

I further authorize Ryerson University to reproduce this thesis by photocopying or by other means, in total or in part, at the request of other institutions or individuals for the purpose of scholarly research.

I understand that my thesis may be made electronically available to the public.

MECHANICAL PROPERTIES OF FIBER LASER WELDED AND FRICTION STIR (SPOT) WELDED LIGHTWEIGHT ALLOYS

Mohammed Shafiul Hasib Chowdhury

MASc., Mechanical Engineering

Ryerson University, Toronto, 2012

ABSTRACT

Mechanical properties of fiber laser welded (FLWed), friction stir welded (FSWed), and friction stir spot welded (FSS weld) AZ31B-H24 Mg and Al 5754 alloys were studied. After welding, grains at the weld centre became recrystallized. β-$Mg_{17}Al_{12}$ particles appeared in the fusion zone of the joints during laser welding, while a characteristic interfacial layer consisting of $Al_{12}Mg_{17}$ and Al_3Mg_2 was observed in the Al/Mg dissimilar FSS weld. In FLWed joints, a joint efficiency of ~91% with superior yield strength, ultimate tensile strength and fatigue strength was achieved at a higher welding speed. In FSWed joints, a higher welding speed of 20 mm/s and lower rotational rate of 1000 rpm led to higher YS, but lower ductility, strain-hardening exponent and hardening capacity. In FSS weld joints, Mg/Mg, Al/Al FSS welds and Al/Mg adhesive, Mg/Al adhesive FSS welds had a significantly higher lap shear strength and fatigue life than the Al/Mg FSS weld.

ACKNOWLEDGEMENTS

To

My Parents

Late Md. Ayub Ali Chowdhury and Mrs. Farida Yeasmin

TABLE OF CONTENTS

LIST OF TABLES

LIST OF FIGURES

xix

NOMENCLATURE

Acronym	Definition
Al	Aluminum
ASTM	American society for testing and materials
BM	Base metal
CDZ	Columnar dendrite zone
EDS	Energy dispersive X-ray spectrometry
FSW	Friction stir welding
FSWed	Friction stir welded
FSSW	Friction stir spot welding
FSS weld	Friction stir spot welded
FLW	Fiber laser welding
FLWed	Fiber laser welded
FZ	Fusion zone
GHG	Green house gas
HAZ	Heat affected zone

HCP	Hexagonal close packed
Mg	Magnesium
Mn	Manganese
ND	Normal direction
RPM	Revolution per minute
RD	Rolling direction
Si	Silicon
SZ	Stir zone
S-N	Stress vs. number of cycle to failure
SEM	Scanning electron microscopy
TD	Transverse direction
TMAZ	Thermo-mechanically affected zone
UTS	Ultimate tensile strength
XRD	X-ray diffraction analysis
YAG	Yttrium-Aluminum-Garnet
YS	Yield strength
Zr	Zirconium

Zn   Zinc

Symbol	Definition
K	Strength coefficient according to Hollomon equation
K_1	Strength coefficient according to Ludwik equation
K^*	Strength coefficient according to modified equation
n	Strain hardening exponent according to Hollomon equation
n_1	Strain hardening exponent as per Ludwik equation
n^*	Strain hardening exponent as per modified equation
P	Laser power, KW
P_{max}	Maximum applied load by fatigue tester on test samples, KN
P_{mean}	Average load applied by fatigue tester on test samples, KN
R	Stress ratio or Load ratio
T_0	Ambient temperature, K
T_{max}	Maximum temperature, K
σ	True stress, MPa
σ_{min}	Minimum stress, MPa
σ_{max}	Maximum stress, MPa

σ_a	Stress amplitude, MPa
σ_m	Mean stress, MPa
σ_y	Yield strength, MPa
σ_ε	Effective stress, MPa
ε_ε	Effective strain
ε	True strain
ε_y	Yield strain
μ	Co-efficient of friction
F	Compressive force, KN
r_0	Radius of the shoulder of the friction stir weld tool, mm
r_i	Radius of the pin of the friction stir weld tool, mm
h	Height of the pin of friction stir weld tool, mm
ω	Angular velocity of the friction stir weld tool, rpm
v_o	Welding speed of the friction stir weld tool, mm/s
s	Scale factor
H_c	Hardening capacity

CHAPTER 1

INTRODUCTION

As the global resource and environmental problems tend to be increasingly severe in recent years, considerable attention has been paid to the weight reduction of aerospace structures, automotive bodies, and high speed passenger cars in order to improve the fuel economy and reduce the damaging effect of anthropogenic greenhouse gas emissions [1-8]. To achieve such goals and meet legislative regulations, the manufacturers in the automotive and aerospace sectors have to reduce the vehicle weight via applying advanced lightweight materials [4,5,9-15]. Recently, the development and application of the ultralight-weight magnesium alloys have been significantly increasing in the transportation sectors due to their low density, high strength-to-weight ratio, and superior damping capacity [1,9-13,16,17]. In contrast, design and manufacturing with aluminum alloys is longstanding in aerospace and automotive structures and becoming increasingly significant in heavyweight vehicles and high speed passenger rail bodies to take advantage of the light weight and good strength properties [8,18]. The structural application of magnesium and aluminum alloys inevitably involves welding and joining in the manufacturing process, understanding the weldability of magnesium and aluminum alloys plays an essential role in determining the viability of component lightweighting through replacement with magnesium and aluminum alloys. In this regard, mechanical properties such as strength (tensile and fatigue), ductility, strain-hardening behavior, etc., of all welded joints used in structural applications must be evaluated to ensure the integrity and safety of the joint and structure. However, until now, the evaluation of different welded joints in Mg and Al alloys using novel welding techniques in terms of mechanical properties is very limited. Some limited

work on the fiber laser welding (FLW) of Mg alloys has recently been reported [19-21]. For the friction stir welding (FSW) of Mg alloys, relatively little attention has been paid as to how the mechanical properties of the FSWed joints change with different processing parameters. On the other hand, the integrity and durability issues of similar Mg and Al friction stir spot (FSS) welds and dissimilar Al-to-Mg FSS welds with and without adhesive especially under cyclic loading have not been systematically studied, and no fatigue behavior for such FSS welds in relation to the change in the failure mode has been reported in the open literature. Thus, the aim of the present study was to evaluate different welded joints of AZ31B Mg alloy and Al 5754-O alloy in terms of microstructural evolution, texture, micro-hardness, tensile properties, strain hardening and fatigue properties.

A literature survey is presented in Chapter 2 on Mg and Al alloys and their properties. Basic principles of different welded joints along with the published results of microstructural evaluation, tensile and fatigue properties of the welded joints are also discussed. Chapter 3 gives the experimental procedures involved in this study. Chapters 4, 5, 6, and 7 present the test results obtained in this thesis work. Microstructural characterization, micro-hardness, tensile and fatigue properties of AZ31B-H24, Al 5754-O and welded joints are presented and analyzed in those four Chapters. Chapter 8 presents summary and future scope of the relevant work.

CHAPTER 2

LITERATURE REVIEW

2.1 Magnesium and Its Alloys

Magnesium is rapidly winning recognition as an important engineering material. Practically unknown over 100 years ago, except in the university laboratories, it is now widely accepted in real commercial structural applications. Recent advances have changed magnesium from a laboratory product to an important engineering metal [22]. It is the lightest metal known to processing properties of permanence and stability for structural applications. It has long been a material of fascinating possibilities to engineers, but any commercial application on a large scale was forced to wait upon lower manufacturing costs and the development of high strength alloys. Both of these preliminary steps have now been gradually accomplished. Since 1993, there has been a renewed interest in using magnesium-based alloys in automobile, aerospace and household and sport applications. Their ultra-lightness makes them of particular value in the automotive and aircraft industries [23]. Of the prevalent materials for the next-generation transportation vehicles in the automotive and aerospace industries, magnesium alloys represent a lucrative option for the weight reduction owing to their low density, high strength-to-weight ratio, environmental friendliness, castability and recyclability [24].

2.2 Aluminum and Its Alloys

In the last century, aluminum became the most widely used metal after iron. This dramatic rise to prominence is a result of the qualities of the aluminum and its alloys as well as its economic

advantages [25].The principal characteristic of aluminum is its low density, being second only to magnesium, and, for this reason, it is especially valuable for the aircraft and automotive industries. Aluminum would be ideal if this lightness could be combined with the mechanical properties of the ferrous metals [26]. Although pure aluminum only possesses a low strength which prohibits its use for articles subjected to great stresses but its mechanical properties can be improved by the addition of other constituents, and in some of the alloys formed the density has a slight change. These are the so-called light alloys, in which aluminum is a main constituent. The most significant properties of these alloys are: high strength to weight ratio, easier fabrication, corrosion resistance, high electrical and thermal conductivity, high toughness at cryogenic temperatures, reflectivity, non-toxicity and recyclability.

2.3 Physical Metallurgy and Properties

Magnesium and aluminum alloys have been employed in a wide variety of structural applications because of their favorable combination of tensile strength, elastic modulus and low density. Both magnesium and aluminum alloys have high strength-to-weight ratios and relatively good electrical conductivity and thermal conductivity.

Both magnesium and aluminum are silvery white metals. Table 2-1 shows the physical properties of magnesium and aluminum compared to the other structural materials. In comparison, the density of magnesium is less than one quarter that of iron and two-thirds that of aluminum. The melting point and specific heat of magnesium are almost the same as those of aluminum. The Young's modulus and shear modulus of magnesium are about two-thirds of those of aluminum. Another aspect of magnesium is its good damping behavior. Pure magnesium shows even higher

damping properties than cast iron, although these properties are highly dependent on the prior heat treatment [27].

Table 2-1 Physical properties of metals [27].

	Mg	Al	Ti	Fe	Cu
Lattice Structure	HCP	FCC	HCP	BCC	FCC
Density (gm/cm^3)	1.74	2.70	4.51	7.87	8.98
Melting Point (^{o}C)	650	660	1668	1535	1083
Specific Heat (cal/m.^{o}C)	0.24	0.22	0.13	0.11	0.09
Young's Modulus (GPa)	45	76	114	190	136
Shear Modulus (GPa)	17	26	45	80	44
Thermal Conductivity (W/m.K)	167	238	16	73	394
Yield Strength (MPa)	130	100	140	50	33
Ultimate Tensile Strength (MPa)	220	250	220	540	210

2.4 Types of Magnesium and Aluminum Alloys

For the materials where alloying can significantly enhance strength for structural purposes, for practical design different types of magnesium and aluminum alloys are usually used:

-**Magnesium alloys**: Aluminum is the most commonly used alloying element and forms the basis of the die casting magnesium alloys. Maximum solubility of Al in magnesium is 12.7 wt % and alloys in excess of 6 wt % can be heat treated. Aluminum improves strength, with an optimum combination of strength and ductility being observed at about 6%. The alloys are readily castable [23]. Zinc is used as an alloying element to increase the strength of the magnesium alloys by solid solution and precipitation. However, it reduces the ductility of the Mg alloys [28]. Manganese is usually not employed alone but with other elements, e.g., Al. In this case, compounds such as MnAl, $MnAl_6$ or $MnAl_4$ are formed. Mn reduces the solubility of iron and produces relatively safe compounds. It increases the yield strength and improves salt water corrosion resistance of Mg-Al and Mg-Al-Zn alloys. Binary alloys are used in forgings or extruded bars. The maximum amount of manganese is 1.5-2.0 wt %. [23]. Till now, the main fabrication route of magnesium alloy parts remains die-casting because of its high productivity and dimensional accuracy. It is well known that wrought magnesium alloys have superior mechanical properties than cast alloys. Often these superior properties are attained through hot working such as rolling, forging and extrusion during which the grains are greatly refined.

-**Aluminum alloys**: The main alloying elements are copper, zinc, magnesium, silicon, manganese and lithium. The primary alloying elements and the properties of the resulting wrought alloys are listed below [26]:

1xxx: This series is for commercially pure aluminum, defined in the industry as being at least 99% aluminum. **2xxx:** The primary alloying element for this group is copper, which produces high strength but reduced corrosion resistance. **3xxx:** Manganese is the main alloying element for the 3xxx series, increasing the strength of unalloyed aluminum by about 20%. **4xxx:** Silicon is added to alloys of the 4xxx series to reduce the melting point for welding and brazing

applications. **5xxx:** The 5xxx series is produced by adding magnesium, resulting in strong, corrosion-resistant, high-welded-strength alloys. The strength of alloys in this series is directly proportional to the magnesium content, which ranges up to about 6%. **6xxx:** Alloys in this group contain magnesium and silicon in proportions that form magnesium silicide (Mg_2Si). These alloys have a good balance of corrosion resistance and strength. 6061 is one of the most popular of all aluminum alloys, and it has yield strength comparable to mild carbon steel. **7xxx:** The primary alloying element of this series is zinc. The alloys of this group include the strongest aluminum alloy, 7178, which has a minimum tensile ultimate strength of 84 ksi (580 MPa), and are used in aircraft frames and structural components. Casting alloys contain larger proportions of alloying elements than wrought alloys. This results in a heterogeneous structure, which is generally less ductile than the more homogeneous structure of the wrought alloys. Cast alloys also contain more silicon than wrought alloys to provide the fluidity necessary to make a casting [26].

2.5 Friction Stir Welding

Friction stir welding (FSW) is a green solid-state joining process and is used for applications where the original metal characteristics must remain unchanged as far as possible. It was invented and experimentally proven by Wayne Thomas and a team of his colleagues at The Welding Institute, UK in December 1991 [29]. Fig. 2.1 presents a schematic of the FSW process. In this process, a cylindrical-shouldered tool, with a profiled threaded/unthreaded probe (nib or pin) is rotated at a constant speed and fed at a constant traverse/welding speed into the joint line between two pieces of sheet or plate material, which are butted together. The parts have to be clamped rigidly onto a backing bar in a manner that prevents the abutting joint faces from being

forced apart. The length of the nib is slightly less than the weld depth required and the tool shoulder should be in intimate contact with the work surface. The nib is then moved against the work, or vice versa. Frictional heat is generated between the wear-resistant welding tool shoulder and nib, and the material of the work pieces. This heat, along with the heat generated by the mechanical mixing process and the adiabatic heat within the material, cause the stirred materials to soften without reaching the melting point, allowing the traversing of the tool along the weld line in a plasticized tubular shaft of metal. As the pin is moved in the direction of welding, the leading face of the pin, assisted by a special pin profile, forces plasticized material to the back of the pin while applying a substantial forging force to consolidate the weld metal. The welding of the material is facilitated by severe plastic deformation in the solid state, involving dynamic recrystallization of the base material [30].
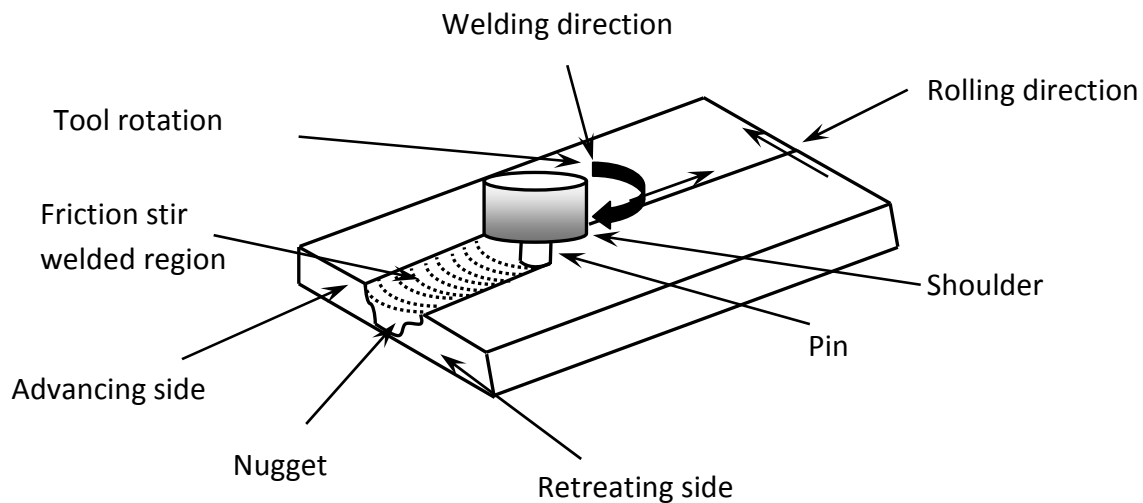
Fig.2.1 A schematic of friction-stir welding process [24].

The total energy generated per unit length of the weld is the sum of the energy generated due to friction between the tool and the workpiece surface and the plastic deformation within the workpiece. Thus, the total energy generated during FSW can be expressed as follows [30],

$$E_{total} = 2\mu F(\frac{1}{3}r_o + \frac{r_i^2}{r_o^2}h)\frac{\omega}{v_o} + s\sigma_\varepsilon\varepsilon_\varepsilon(2r_ih)$$

(2.1)

where μ is the coefficient of friction, F is the compressive force, r_o is the radius of the shoulder, r_i is the radius of the pin, h is the height of the pin, ω is the tool angular velocity in rpm (rev/min), v_o is the welding speed, s is a scale factor, σ_ε is the effective stress and ε_ε is the effective strain. In Chapter 5 the effect of heat input along with transverse speed ω and welding speed v_o are discussed in detail.

2.6 Fiber Laser Welding

Fiber laser welding, first used in materials processing in 2000 [31], is best employed for keyhole welding. The laser is finely focused so as to achieve a very high power density (typically at least 1 MW/cm^2) at the work piece. At the center of the focused beam, metal actually vaporizes, opening up a blind keyhole into the molten metal pool. Vapor pressure holds back the surrounding molten metal and keeps this keyhole open during the process. This metal vapor also re-radiates laser energy into the molten metal along the side of the keyhole, thus transferring energy through the entire depth of the keyhole and resulting in a weld with a deep aspect ratio. The small size of keyhole region results in a relatively small fusion zone (FZ) and heat-affected zone (HAZ). Furthermore, the highly localized application of heat means that the work piece both heats up and cools down rapidly which can minimize grain growth in high strength low alloy steels (HSLA). Even though no filler material is typically used in keyhole welding, the high

temperatures of keyhole welding can vaporize volatile materials, producing a different composition in the fusion zone than in the base metal [31]. Fig 2.2 presents a schematic of the fiber laser welding process.
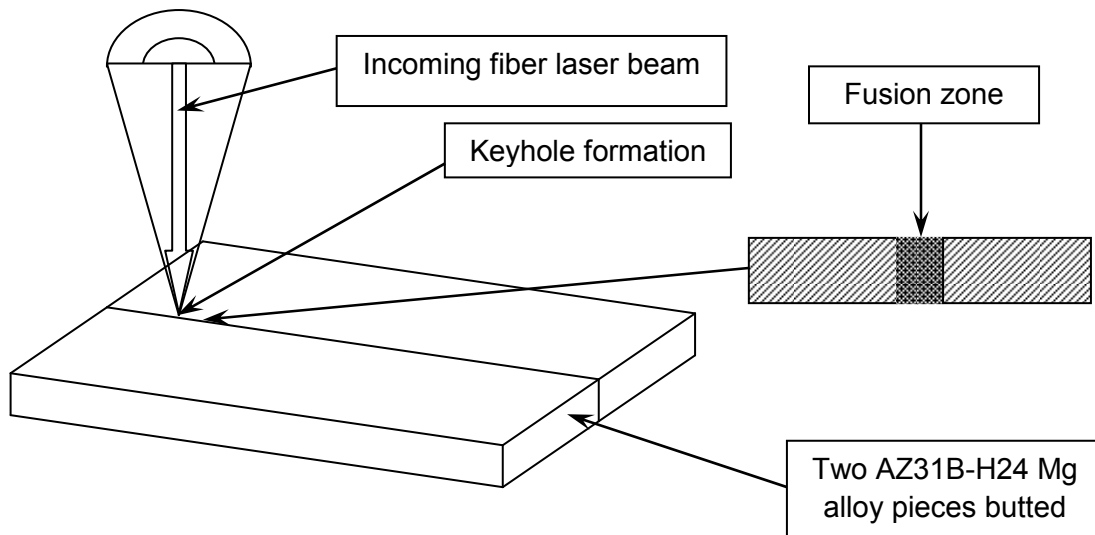
Fig.2.2 Schematic illustration of fiber laser welding [32].

2.7 Friction Stir Spot Welding

In 1993, based on the linear friction stir welding (FSW), Mazda Corporation of Japan proposed a friction stir spot welding (FSSW) process which has successfully been applied to the production of hood and rear door of the sport vehicle Mazda RX-8 [8]. For aluminum and magnesium alloys, the conventional resistance spot welding process poses some technical issues, including weld porosity, electrode wear, high energy consumption, low production efficiency, and inconsistency in failure modes [33-38]. Therefore, the automotive industry is on the lookout for some alternative and relatively new methods, such as structural adhesives, rivets, and toggle-locks, to join aluminum and magnesium sheets. The FSSW process provides a potential solution in terms of joint strength performance, weld quality, and operation cost without adding extraweight [34]. A schematic illustration of the FSSW process is shown in Fig.2.3, where

FSSW process is applied to a lap joint consisting of upper and lower sheets. A rotating tool with a probe is plunged into the material from the top surface for a certain time to generate frictional heat. At the same time, a backing plate contracts the lower sheet from the bottom side to support the downward force. Heated and softened material adjacent to the tool causes plastic flow. In addition, the tool shoulder gives a strong compressive force to the material. After the tool is drawn away from the material, a solid phase is made between the upper and lower sheets [39].
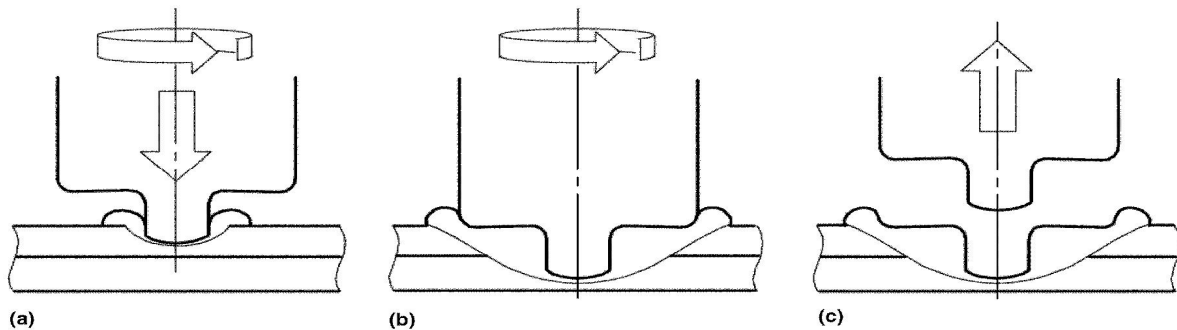
Fig.2.3 Friction stir spot welding illustration, (a) Plunging (b) Bonding (c) Drawing out [39].

2.8 Previous Studies

A lot of studies on the fusion welding of Mg alloys have been reported. Weisheit *et al*. [40] performed CO_2 laser welding of different Mg alloys and showed that most Mg alloys can be easily welded without serious defects, except AZ series and AM series which exhibited extremely high levels of porosity. Zhao and Debroy [41] investigated the formation of porosity in an AM60 Mg alloy during laser welding and concluded that hydrogen in the parent material was the main origin of porosity in the welds. Sun *et al*. [42] evaluated TIG, CO_2 and pulsed Nd:YAG laser welded joints of AZ31 sheet and reported that TIG welding could be used to

achieve welds without defects, but noted that coarser grain sizes in TIG welds could diminish the mechanical properties. Quan *et al.* [43] studied the effects of heat input on microstructure and tensile properties of a laser welded AZ31 Mg alloy. Liu and Dong [44] reported the effect of microstructural changes on the tensile properties of a non-autogenous gas tungsten arc welded AZ31 magnesium alloy. Zhu *et al.* [45] presented the effect of welding parameters on the welding defects and microstructural evolution in CO_2 and diode laser welded AZ31 magnesium alloy.

Recently, among the several types of lasers, attention has been paid to fiber lasers, because this type of lasers presents a number of benefits for industrial applications, namely high power with small beam divergence, flexible beam delivery, low maintenance costs, high efficiency of laser generation and compact size of laser apparatus [46]. Limited work on the fiber laser welding (FLW) of Mg alloys has recently been reported. Sakai *et al.* [19] conducted welding on a 2 mm thick extruded sheet of Mg-6Al-2Ca alloy at a welding speed of 10 m/min using a 3 kW fiber laser, and obtained the tensile strength of welded joints reaching about 84~88% of that of the base metal. Liu *et al.* [20] also performed welding of an ACM522 Mg alloy using a fiber laser and showed that sound welds without major defects could be achieved. However, porosity in the fiber laser welds of two thixomolded Mg alloys AE42 and AS41 occurred, and the volume fraction of porosity in the welds decreased with increasing welding speed [21]. A lot of studies on the FSW of magnesium alloys have been reported, including microstructural evaluation [47-52] and tensile properties [47,50,53-59] in relation to the welding parameters. Some earlier results on the microstructural changes and strength of various FSWed magnesium alloys have been well documented in references [60-63]. Several authors have studied the strain hardening

behavior of magnesium alloys with emphasis on the relationship between the grain size strengthening and dislocation strain hardening of the material [58,64-67].The progressive developments in electron backscatter diffraction (EBSD) over the last decade or so have promoted research work on the microtexture of FSWed materials [62,68,69]. By analyzing X-ray diffraction (XRD) patterns, Chang *et al.* [70] studied the grain orientation of FSWed AZ31 and found that the tool rotational rate played an important role in the orientation of the basal plane (0002). Park *et al*. [62] reported that the development of the texture was due to the basal slip $(0002)<11\bar{2}0>$, which was favored over prismatic or pyramidal slip at the room temperature, and the strain rates during plastic deformation.

On the other hand, a number of papers on the joining of Mg and Al alloys using FSSW have recently been reported [8,18,71,72], only limited studies have been done on lap shear strength and especially fatigue resistance of the FSSW joints, a topic of vital importance for the safe and reliable applications. With regards to FSS welds made of similar Al alloys, the failure modes at quasi-static and cyclic loads vary with loading type. Lin *et al*. [73] observed some differences in the fracture path between quasi-static loads and fatigue loads for AA6111-T4 alloy. Latabhai *et al*. [74] indicated that the shear strength first increased and then decreased with increasing tool rotational rate for AA6061-T5 FSSW joints, while Tozaki *et al.* [75] reported that the tensile shear strength monotonically increased with increasing tool rotational rate. Mallick and Agarwal [76] evaluated the fatigue performance of FSS welds made of AM60 and AA 5754 alloys but the failure mechanisms were not studied in detail. FSS welds of dissimilar Al and Mg alloys were observed to exhibit different failure modes compared with those with identical alloys for both top and bottom sheets [18,71,77]. Recently, some new kinds of hybrid welding techniques have been

used to join dissimilar Al-to-Mg alloys, such as laser adhesive welding [15,78-80]. Liu and Ren [78] indicated that the lap shear strength increased in the MIG spot adhesive welded AZ31B to Al 6061 joints, while Wang *et al.* [15] found that the addition of the adhesive increased the weld penetration depth in the Al alloy side for Nd:YAG laser adhesive welds of dissimilar Mg-to-Al alloys.

2.9 Research Objectives

Based on the above literature survey, it is clear that a suitable welding method for Mg and Al alloy has not yet been fully established. The fatigue properties are critical in design considerations as the automotive and aerospace components are inevitably subjected to dynamic or cyclic stresses in service; however, no or very limited studies of fatigue behavior of fiber laser welded (FLWed) Mg joints, friction stir spot welded (FSS welds) and friction stir spot adhesive welded Mg and Al joints were reported in the open literature. Thus, the aim of the present investigation was to:

- Evaluate the microstructure, tensile properties, strain hardening, and fatigue properties of fiber laser welded AZ31B Mg alloy sheet with particular focus on the effect of welding speed.

- Identify the effect of welding parameters on the microstructure, texture and mechanical properties of friction stir welded AZ31B-H24 Mg alloy sheets.

- Determine the lap shear strength and fatigue resistance of the friction stir spot welded similar AZ31B-H24 and AA5754-O alloy, and dissimilar AZ31-to-AA5754 alloy joints.

- Evaluate the lap shear strength and fatigue resistance of the friction stir spot adhesive welded AZ31B-H24 alloy to AA5754-O alloy and compare the results with those of the dissimilar AZ31-to-AA5754 alloy joints.

CHAPTER 3

MATERIALS AND EXPERIMENTAL PROCEDURE

3.1 Materials and Composition

AZ31B-H24 Mg alloy and Al 5754-O Al alloy were selected in this study. The AZ31B Mg alloy material for fiber laser welding was provided by General Motors Research and Development Center (GM R&D) through the University of Waterloo, Waterloo, Ontario, Canada. The chemical composition of the alloy is listed in Table 3-1.

Table 3-1 Chemical composition of AZ31Mg alloy (wt.%).

Al (wt%)	Zn (wt%)	Mn (wt%)	Fe (wt%)	Ni (wt%)	Mg (wt%)
3.000	1.000	0.600	0.005	0.005	Balance

The FSWed joints of AZ31B-H24 Mg alloy and FSSW of AZ31B-H24 Mg alloy and Al 5754-O alloy were received from Aerospace Manufacturing Technology Centre, Institute for Aerospace Research, National Research Council of Canada, Montreal, Quebec, Canada. The chemical composition of the Al 5754-O alloy is listed in Table 3-2.

Table 3-2 Chemical composition of Al 5754-O alloy (wt.%).

Mg (wt %)	Sc (wt%)	Zr (wt%)	Al (wt%)
3.42	0.23	0.22	Balance

Three different types of welding, namely, friction stir welding (FSW), friction stir spot welding (FSSW) with or without adhesive, and fiber laser welding (FLW) were employed to make autogenous welds between the work-pieces in the butt and lap joint configurations. All welded joints were made with the welding direction perpendicular to the rolling direction of the sheet. Prior to welding, surface oxides were removed with a steel brush and then the surface was cleaned using ethanol as well. The welding parameters for those welding methods are listed in Table 3-3. In addition, for the friction stir spot adhesive weld, Mg and Al alloy sheets were cut into small coupons of 35 mm × 100 mm with the loading axis along the rolling direction. Two coupons were overlaid over an area of 35 mm × 35 mm between which Terokal 5089 adhesive had been applied and cured at a temperature of 170°C for 20 min. FSSW was then performed at the centre of the overlapped area.

Table 3-3 Welding parameters of all welded joints used in the present study.

Welding Method	Welding speed(mm/s)	Rotational rate (clockwise)rpm	Thread of the weld tool	Welding power (KW)
FSW	20	2000	Left-hand	
	20	1000		
	5	1000		
FSSW	-	2000	Left-hand	-
FLW	100	-	-	2
	50	-	-	2

3.2 Sample Preparation and Testing

The experimental tests were conducted and metallographic sample were prepared in the laboratories of Mechanical Engineering Department at Ryerson University.

3.2.1 Metallography

All metallographic samples for microstructural characterization were taken from the cross section perpendicular to the welding direction and were cold mounted using Lecoset 7007 resin (mixing ratio: 2 parts of resin added to 1 part of catalyst). The mounted samples were manually ground with SiC papers up to a grit of #1200 with water as the lubricant and then polished with 6 μm, 3 μm, and 1 μm diamond paste followed by 0.5 μm finer MasterPrep solution. The polishing

lubricant for the diamond paste was a mixture of rust inhibiting solution and distilled water (10% solution by volume). Due to the reactive nature of magnesium in the presence of water, ethanol was used as a cleaning agent during the polishing stages. Two etchants were used individually - etchant 1: acetic picral (10 ml acetic acid (99%), 4.2 g picric acid, 10 ml H_2O, 70 ml ethanol (95%)) for Mg alloy, and etchant 2: Keller's reagent (2.5 ml nitric acid, 1.5 ml hydrochloric acid, 1 ml hydrofluoric acid and 100 ml distilled water) for Al alloy.

3.2.2 Quantitative Image Analysis

Microscopic images were taken using a light microscope and image analysis was subsequently performed using Clemex software to obtain the grain size. The Clemex image analysis system was composed of Clemex CMT software adaptable to ASTM standards, a Nikon optical microscope (10× eye piece, five different object lenses with magnifications of 5×, 10×, 20×, 40×, and 100×), a high-resolution digital camera, and a high performance computer to carry out the detailed analysis.

3.2.3 Microhardness Tests

A computerized Buehler microhardness testing machine was used for the micro-indentation hardness tests where a load of 100 g and duration of 15 s were used. The test results were recorded in the computer using a Hyper Terminal. Vickers microhardness tests were performed on the unetched samples. All the indentations were adequately spaced to avoid any potential effect of strain fields caused by adjacent indentations.

3.2.4 Tensile Tests

All butt joint samples for tensile tests were prepared according to the ASTM E8M standard [81] using sub-sized sheet type specimens (i.e., a gauge length of 25 mm and a gauge width of 6 mm). The specimen dimensions are shown in Fig. 3.1. All samples for the tensile tests were taken parallel to the rolling direction, with the weld positioned in the middle of the specimens. The tests were carried out using a computerized United testing machine at four different strain rates: $1\times10^{-2}\,s^{-1}$, $1\times10^{-3}\,s^{-1}$, $1\times10^{-4}\,s^{-1}$ and $1\times10^{-5}\,s^{-1}$. Lap shear tensile tests were conducted using the lap joint samples at a crosshead displacement speed of 10 mm/min. All the tests were conducted at room temperature.
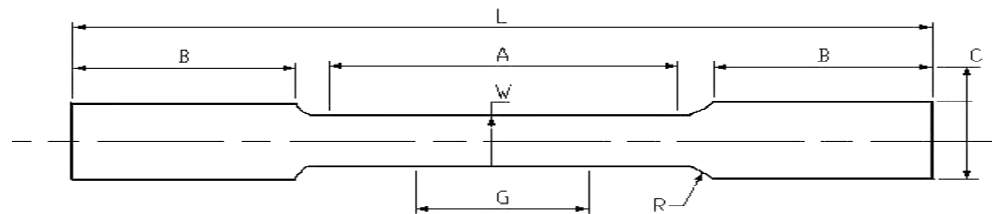
Dimensions in mm	
G − Gauge length	25
W − Width	6
R − Radius	6.35
L − Overall length	140
A − Length of the reduced section	32
B − Length of the Grip Section	50
C − Width of the grip section	9.52

Fig.3.1 Geometry and dimensions of the sub-sized tensile/fatigue test specimen according to ASTM E8M [81].

3.2.5 Fatigue Tests

Fatigue tests were performed using a fully computerized servo-hydraulic Instron 8801 fatigue testing system. The butt joint samples for fatigue tests were similar to the tensile testing samples, as shown in Fig. 3.1. The tests were carried out in a load control mode at different stress amplitudes. A stress ratio of R ($\sigma_{min}/\sigma_{max}$) equal to 0.1, sinusoidal waveform, and frequency of 50 Hz were selected in all the tests. Fatigue tests for the lap joint samples were carried out using similar testing system under load control. A load ratio of R=0.2, sinusoidal waveform, and a frequency of 50 Hz were applied in all the tests. At least two samples were tested at each stress or load level. The fracture surfaces of the welded joints after fatigue tests were examined via a JSM-6380LV scanning electron microscope (SEM) equipped with Oxford energy dispersive X-ray spectroscopy (EDS) system and three-dimensional (3D) fractographic analysis capacity.

3.2.6 X-ray Diffraction Tests

A multi-functional PANalytical X'Pert PRO X-ray diffractometer was used to identify the formation of phases in the fusion zone, heat-affected zone of the FLWed samples and intermetallic compounds in the dissimilar Al-to-Mg FSS welds from the fracture surface (both Mg side and Al side) after fatigue tests. X-ray diffraction (XRD) was performed using CuK_α radiation (wavelength λ=0.15406 nm) at 45 kV and 40 mA. The diffraction angle (2θ) at which the X-rays hit the sample varied from 20° to 110° with a step size of 0.05-0.2° and 3-10 s in each step. Furthermore, crystallographic texture of the FSWed specimens was measured by XRD using CuK_α radiation at 45 kV and 40 mA as well, with a sample tilt angle ranging from 0 to 70°. The specimens for the pole figure measurements were mounted on the XRD sample stage in such an orientation that the sheet rolling direction (RD) was always parallel to the X-axis of the

sample stage. The pole figures were measured and analyzed by 'X-pert texture' software, where the results were represented as (0002), (10$\bar{1}$0), and (10$\bar{1}$1) color-scale intensity poles.

CHAPTER 4

FIBER LASER WELDED AZ31 MAGNESIUM ALLOY: EFFECT OF WELDING SPEED ON MICROSTRUCTURE AND MECHANICAL PROPERTIES

4.1 Microstructure

Typical microstructures of AZ31B-H24 Mg alloy base metal and fiber laser welded joints are shown in Fig. 4.1 for a welding speed of 50 mm/s and Fig. 4.2 for a welding speed of 100 mm/s, respectively. As shown in Fig. 4.1(a), elongated and pancake-shaped grains with varying sizes were observed in the base metal. The heterogeneity in the grain structure of the base metal was due to both deformation of the 2 mm thick sheet by rolling and incomplete dynamic recrystallization (partial annealing). A similar result has been reported for AZ31B-H24 Mg alloy in [53]. Laser welding led to a considerable change in the microstructure. Due to the high power density in fiber laser welding that led to a deep and narrow fusion zone, the weld bead was fairly narrow at both the top and bottom and no distortion or drop-through was observed across the weld (Fig.4.1(b)). However, the lower welding speed of 50 mm/s resulted in a slightly wider fusion zone (Fig. 4.1(b)), in comparison with that of the welded joint made at a welding speed of 100 mm/s (Fig. 4.2(a)). This was due to the higher energy input at the lower welding speed. The fusion zone exhibited typical equiaxed dendritic structures in both welding conditions, containing a large number of divorced eutectic β-$Mg_{17}Al_{12}$ precipitates existing basically in the interdendritic and intergranular regions (Fig. 4.1(c) and Fig. 4.2(b)). Such divorced eutectic β-$Mg_{17}Al_{12}$ precipitates only appeared in the fusion zone, as revealed by the XRD micro-diffraction

(Fig. 4.3). The presence of the eutectic structure was due to the non-equilibrium rapid cooling of the weld pool during welding. Such β-Mg$_{17}$Al$_{12}$ precipitates were also observed in the fusion zone of diode laser [82], laser/arc hybrid [83], double-sided arc [84], and resistance spot welded [85] Mg joints. However, the grain size (or dendrite cell size) in the fusion zone appeared larger at a lower welding speed of 50 mm/s (Fig. 4.1(c)) than at a higher welding speed of 100 mm/s (Fig. 4.2(b)). As the fiber laser welded joint at a welding speed of 50 mm/s had more heat energy deposited in the welding area and a lower cooling rate, the temperature in the fusion zone would be expected to be higher [86]. This would result in larger sizes of equiaxed dendrite cells along with a relatively fewer divorced eutectic β-Mg$_{17}$Al$_{12}$ precipitates formed in the fusion zone, in comparison with the fiber laser welded joint at a welding speed of 100 mm/s, as shown inFig.4.1(d) and Fig. 4.2(c) taken at a higher magnification. A similar effect of welding speed on the dendrite cell sizes in the fusion zone in a CO_2 laser welded AZ31 magnesium alloy joint was reported in [87] as well. It was reported that the higher the casting temperature (or pouring temperature during casting), the larger the dendrite cell/grain size and the secondary dendrite arm spacing were for aluminum alloys [88,89] and a superalloy [90]. Gilath *et al.* [91] proposed the following expression,

$$d = \frac{C}{\sqrt{v}},\qquad(4.1)$$

Where d is the dendrite spacing, v is the welding speed, and C is an empirical constant. Based on the above equation, a larger dendrite cell/grain size should be observed in the fusion zone at the lower welding speed of 50 mm/s.

Near the fusion boundary, columnar dendrites formed in both welded joints (Fig. 4.1(e) and 4.2(d)). The width of columnar dendrite zone (CDZ) increased with decreasing welding speed from 100 mm/s to 50 mm/s (Fig. 4.1(e) and Fig.4.2(d)), respectively. Similar results have been reported in [43]. The formation of columnar dendrites was due to the presence of a larger temperature gradient near the fusion boundary than in the weld pool center, as reported by Kou [92]. In the heat-affected zone, the originally elongated and partially-deformed base metal structure had become equiaxed grains in both welded joints (Fig. 4.1(f) and 4.2(e)), suggesting that recrystallization and grain growth occurred in the heat-affected zone where no divorced eutectic β-$Mg_{17}Al_{12}$ precipitates were present in contrast to the fusion zone microstructure. This is also visible in from the XRD micro-diffraction spectra shown in Fig.4.3. It is clear that the size of grains in the heat-affected zone was larger at a slower welding speed of 50 mm/s (Fig. 4.1(f)) than at a faster welding speed of 100 mm/s (Fig. 4.2(e)). Again, this was attributed to the higher energy input leading to a higher temperature in the heat-affected zone which sustained a longer time at the slower welding speed. It should be noted that some small pores were observed in the fusion zone, which is more visible on the fracture surface in the later section.
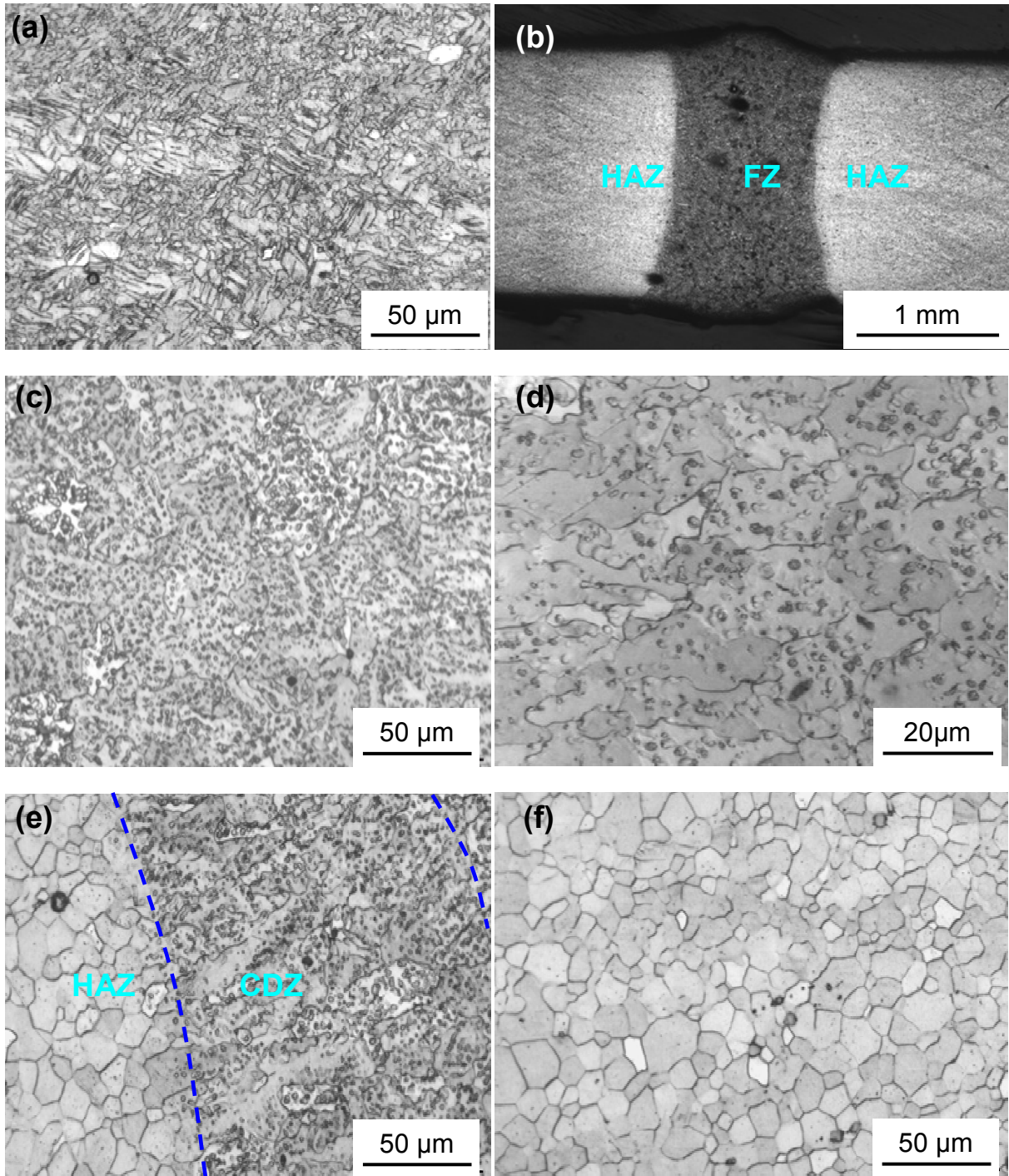
Fig.4.1 Typical microstructures of a fiber laser welded joint made at a welding speed of 50 mm/s.(a) base metal AZ31-H24, (b) cross section of the welded joint, (c) fusion zone (FZ), (d) fusion zone at a higher magnification, (e) columnar dendrites near the boundary of fusion zone, (f) recrystallized heat-affected zone (HAZ).
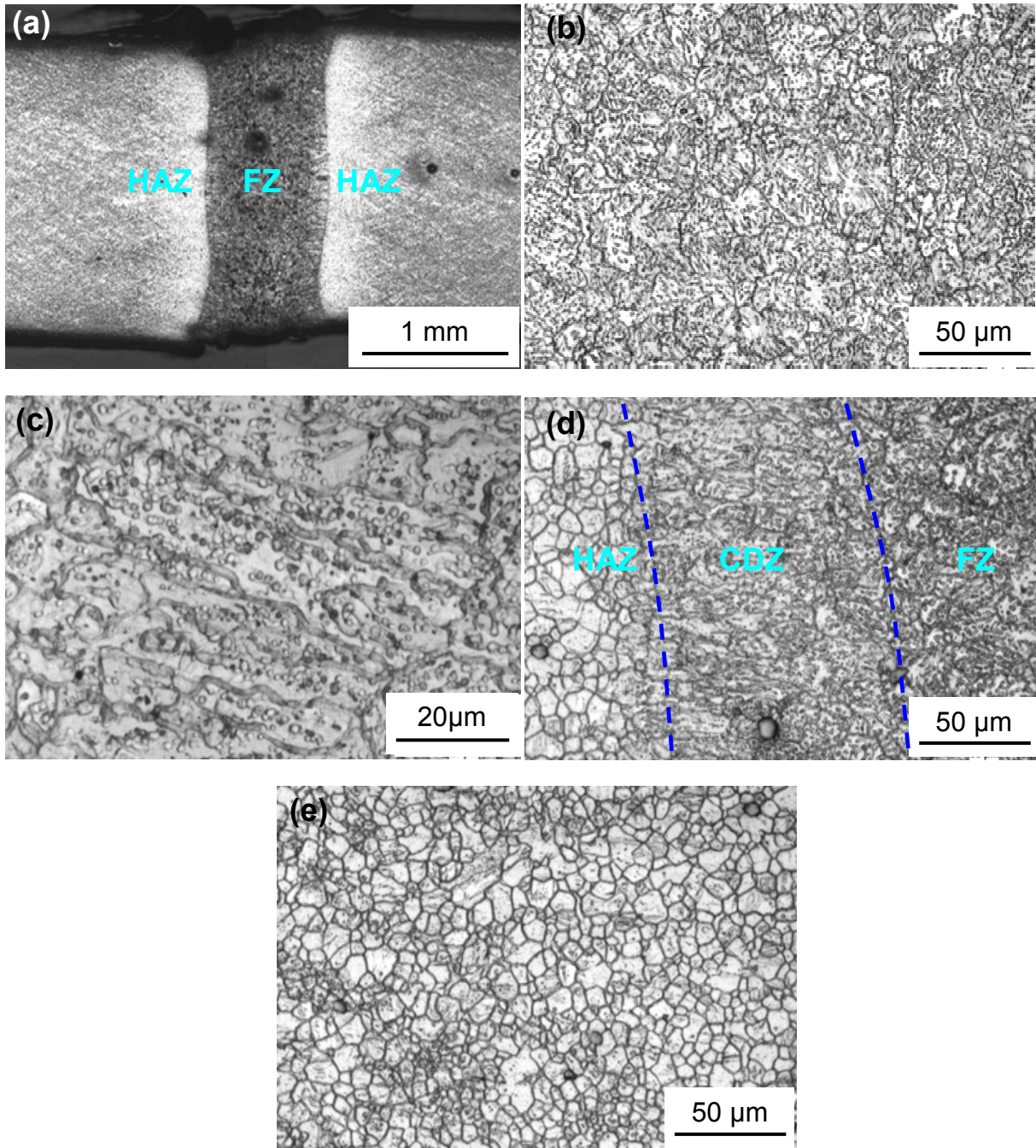
Fig.4.2 Typical microstructures of a fiber laser welded joint made at a welding speed of 100 mm/s. (a) cross section of the welded joint, (b) dendrites in the fusion zone (FZ), (c) fusion zone at a higher magnification, (d) columnar dendrites near the boundary of fusion zone, (e) recrystallized heat affected zone (HAZ).
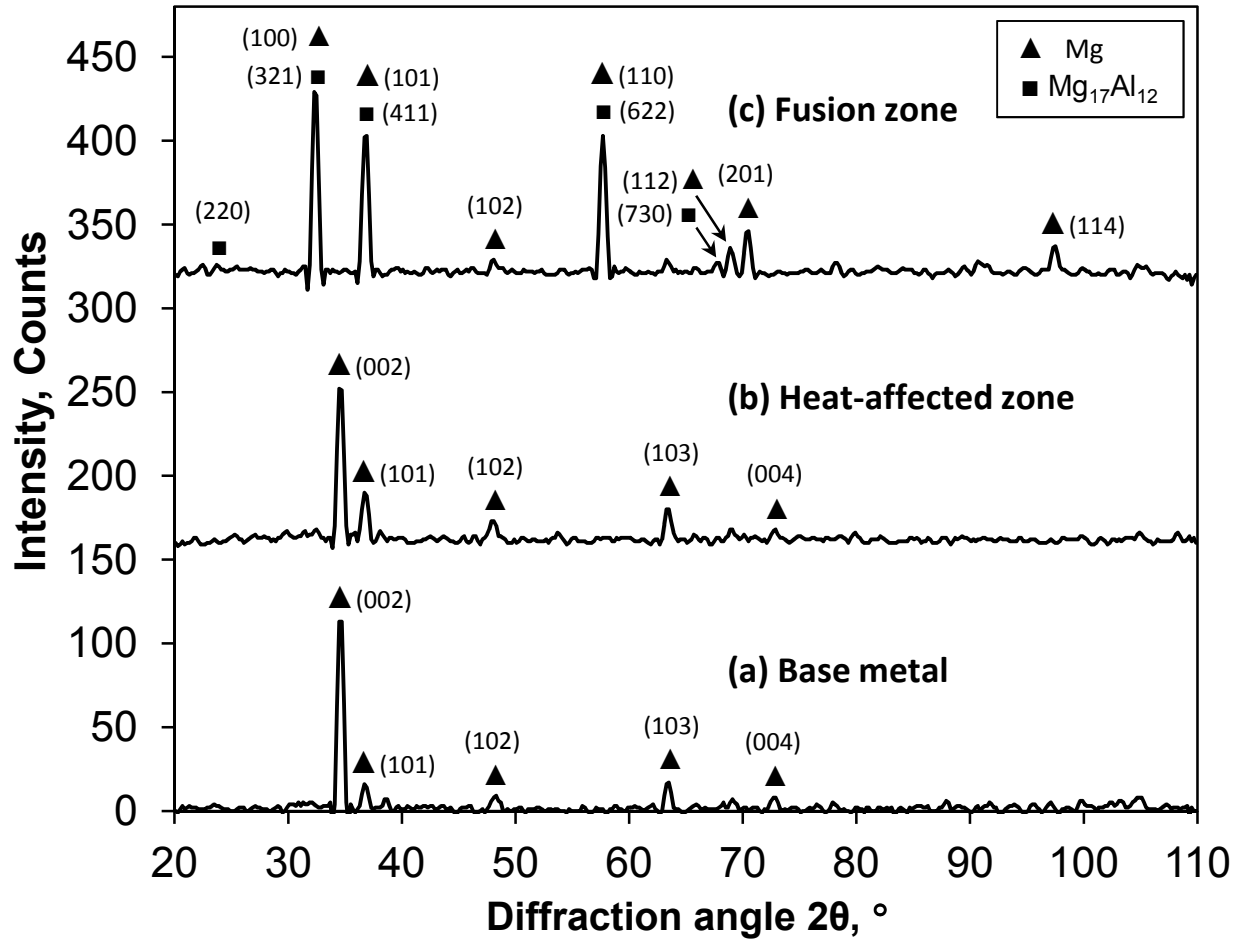
Fig.4.3 X-ray diffraction patterns obtained from (a) base metal, (b) heat-affected zone, and (c) fusion zone of a fiber laser welded joint made at a welding speed of 50 mm/s.

Some particles were also seen in the fiber laser welded joints (Fig.4.4(a)). EDS analysis revealed that these particles were unmelted Mn- and Al-containing inclusions (Fig.4.4(b)),which were still present in the weld pool. These particles could act as nuclei and block off the epitaxial columnar dendrite grains. Similar results were also reported by Xiao *et al.* [36], where they observed that more unmelted Mn-Al particles resulted in a more efficient nucleation, giving rise to a finer grain size in the fusion zone of the weld. Again, a large number of divorced eutectic β-$Mg_{17}Al_{12}$

precipitates were visible nearly uniformly in fusion zone in conjunction with Mn-Al particles (Fig. 4.4(a)).
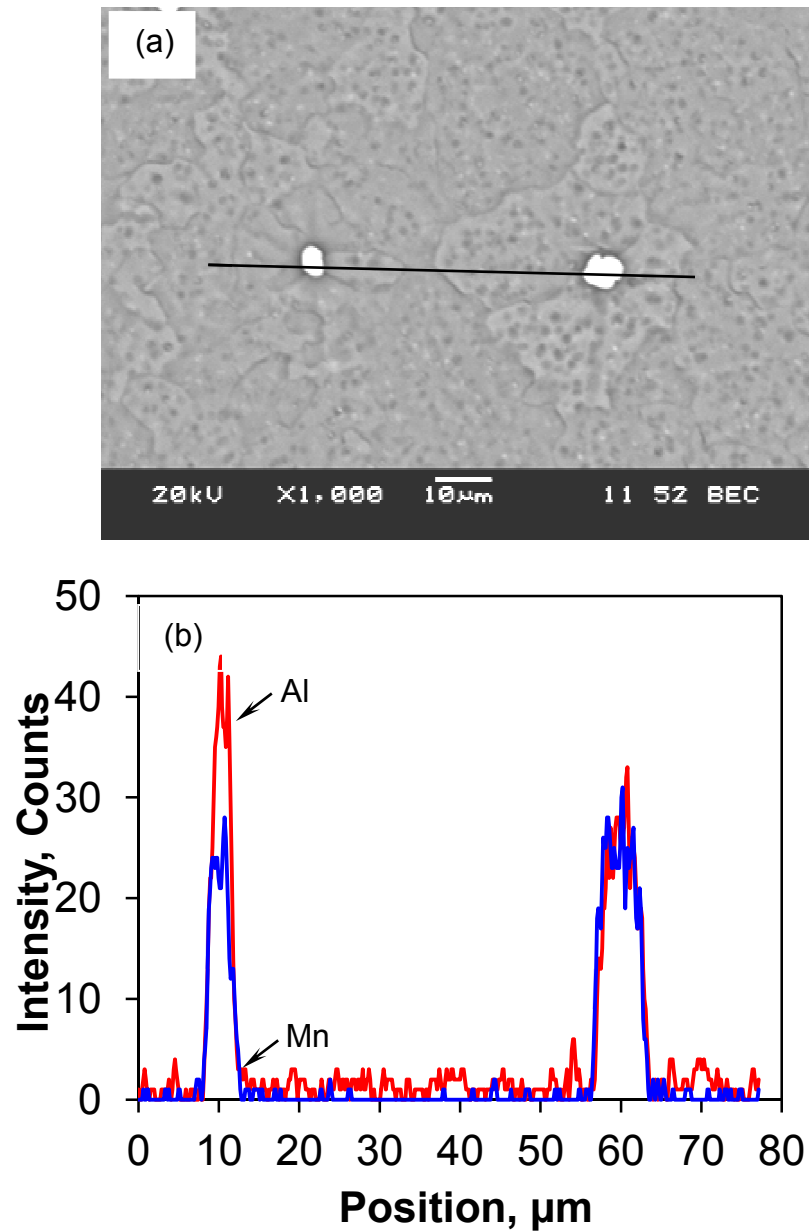
Fig.4.4 (a) SEM micrograph of particles in the fusion zone of fiber laser welded joint made at a welding speed of 50 mm/s, (b) EDS line scan across the two particles in (a) showing Al and Mn compositional variations across the particles in the fusion zone.

4.2 Microhardness profile

Fig. 4.5 shows a typical hardness profile along the mid-thickness of the 2 mm thick fiber laser welded AZ31B-H24 Mg joints that were welded at a welding speed of 50 mm/s and 100 mm/s with a 2 kW laser power. The lowest hardness appeared at the center of fusion zone after laser welding. The hardness value decreased gradually from about 73HV of the base metal in the half-hardened H24 temper to approximately 54HV at the center of fusion zone across the heat-affected zone for the welding speed of 100 mm/s, and about 51HV for the welding speed of 50 mm/s. The hardness of the fiber laser welded joint made at a welding speed of 100 mm/s was generally higher than that made at a welding speed of 50 mm/s, with the lowest hardness in the fusion zone varied from 70% to 74% of the base metal when the welding speed increased from 50 to 100 mm/s. This is due to the larger sizes of equiaxed dendrite grains formed in the fusion zone (Fig. 4.1(c) vs. 4.2(b)) and larger grain sizes in the heat-affected zone (Fig. 4.1(f) vs. 4.2(e)) at the lower welding speed. There was a strong grain size dependence of microhardness, following the Hall-Petch type relationship in the welded AZ31B-H24 Mg alloy [53]. Since the grain boundaries were the main obstacle to the slip of dislocations, the material with a smaller grain size would have a stronger resistance to the localized plastic deformation due to the presence of more grain boundaries, giving rise to a higher hardness or strength. Another reason for the higher hardness would be related to the formation of finer dendrite arm spacing at a higher welding speed, as reported by Turhal and Kan [93].The overall reduction in the hardness after laser welding, shown in Fig. 4.5, is attributed to the remarkable changes in the microstructure from the deformed and elongated grains in the base metal in the half-hardened and partially-annealed H24 state (Fig. 4.1(a)) to the non-equilibrium dendritic solidification structure (Fig. 4.1(c) and 4.2(b)) in conjunction with divorced eutectic β-$Mg_{17}Al_{12}$ particles in the

fusion zone (Fig.4.1(d), Fig. 4.2(c), and Fig. 4.3), and recrystallized equiaxed grains in the heat-affected zone (Fig.4.1(f) and 4.2(e)). Due to the narrower fusion zone and heat-affected zone, the hardness profile at a welding speed of 100 mm/s appeared sharper, as shown in Fig. 4.5.
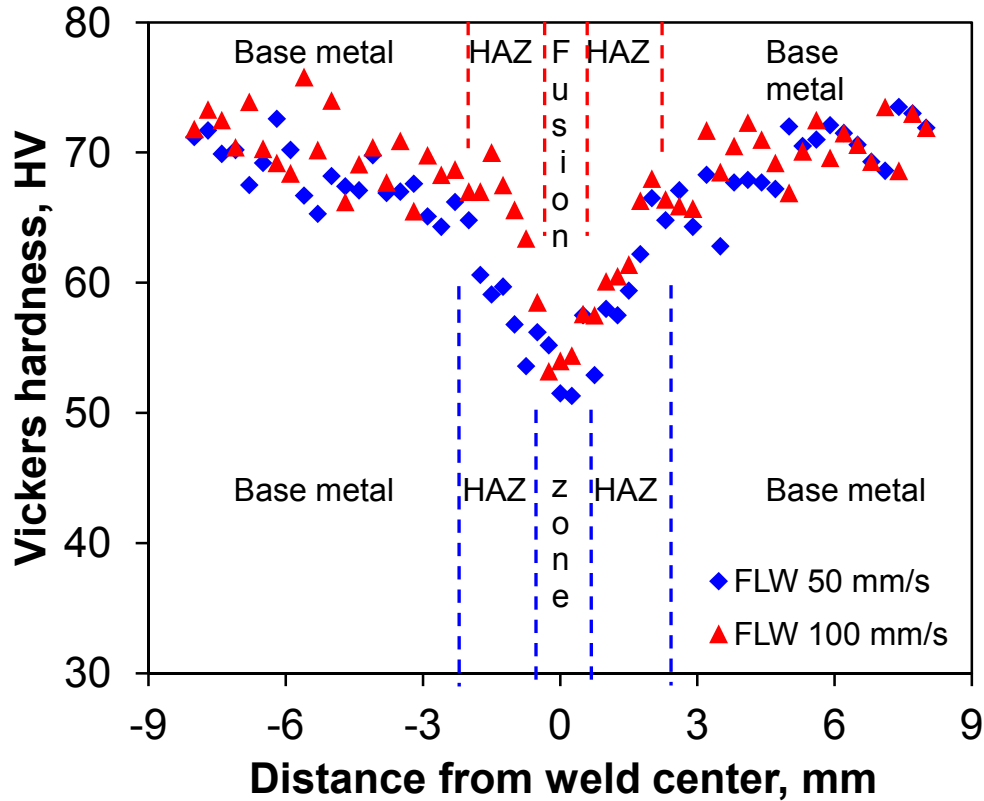
Fig.4.5 Typical microhardness profile of fiber laser welded butt joints at a welding speed of 50 mm/s and 100 mm/s, where HAZ abbreviates heat-affected zone.

4.3 Tensile properties

Fig. 4.6 shows typical stress-strain curves for the base metal, fiber laser welded AZ31B-H24 Mg alloy joints made at different welding speeds of 50 mm/s and 100mm/s and tested at a strain rate

of 1×10^{-4} s^{-1}. It is seen that after welding, both the strength and the elongation (%El) decreased. More reduction in the yield strength (YS) and ultimate tensile strength (UTS) occurred in the fiber laser welded joint at the welding speed of 50 mm/s than 100 mm/s. This was due to the larger dendrite cells/grains in the fusion zone (Fig.4.1(c)) and equiaxed recrystallized grains in the heat-affected zone (Fig. 4.1(f)) at the slower welding speed. As mentioned earlier, the weld exhibited a typical dendritic solidification structure containing a large number of brittle divorced eutectic β-$Mg_{17}Al_{12}$ particles (Fig. 4.1(d) and 4.2(c)), which was significantly different from the microstructure of the rolled and partially-annealed BM (Fig. 4.1(a)).
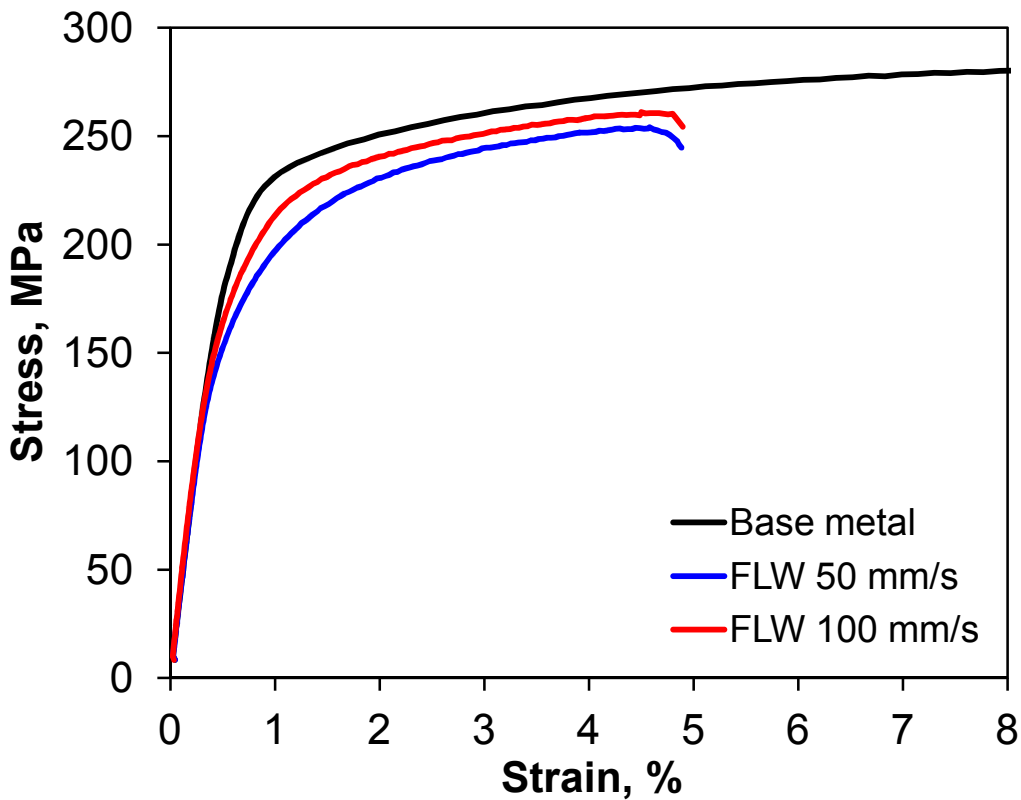
Fig.4.6 Typical engineering stress-strain curves of the AZ31B-H24 Mg base alloy, fiber laser welded joints made at a welding speed of 50 mm/s and 100 mm/s, tested at a strain rate of 1×10^{-4} s^{-1}.

All of the fiber laser welded joints were observed to fracture in the fusion zone during the tensile tests, corresponding to the lowest hardness there (Fig. 4.5). As a result, the ductility of the AZ31B-H24 Mg alloy after laser welding diminished. The evaluated YS, UTS and percent elongation of the base metal, fiber laser welded AZ31B-H24 Mg alloy joints are plotted in Fig. 4.7. It is shown that at all the strain rates both the YS and UTS became lower after laser welding. While the welding led to a relatively larger decrease in the YS, the reduction of the UTS was moderate with a joint efficiency of about 89% at a welding speed of 50 mm/s and about 91% at a welding speed of 100 mm/s. Some values of joint efficiency for different Mg alloys are summarized in Table 4.1, where the joint efficiency is the ratio of the UTS of welded joints to the UTS of the corresponding base alloy. It is shown that a wide range of joint efficiency between ~59% and 97% could be obtained, which was associated with the welding processes and parameters as well as the initial state (or initial strength) of the material. The joint efficiency of the 2 mm thick AZ31B-H24 Mg alloy achieved in the present study using a 2 kW fiber laser at a welding speed of either 50 mm/s or 100 mm/s was higher than that of about 84~88% for the same thickness extruded sheet of Mg-6Al-2Ca alloy using 3 kW fiber laser at a welding speed of 67 mm/s to 167 mm/s [19]. As the strain rate increased from 1×10^{-5} s^{-1} to 1×10^{-2} s^{-1}, the YS and UTS of the base metal increased to a certain degree but the ductility decreased considerably. This indicated the presence of stronger strain rate sensitivity in the base metal due to the smaller grain size (Fig. 4.1(a)). Similar results about the effect of grain size on the strain rate sensitivity were also reported in an extruded AZ31 Mg alloy [64]. As dislocations tend to pile-up at grain boundaries during deformation, the smaller grains with more grain boundaries would facilitate the dislocation pile-ups. Del Valle and Ruano [67] reported a relationship between the strain rate sensitivity ($\partial\sigma/\partial\ln\dot{\varepsilon}$) and grain size ($d$) as follows,

$$\frac{\partial \sigma}{\partial \ln \dot{\varepsilon}} = \frac{k}{2} d^{-1/2} (M_c - 2M_{cg}) + \sigma M_{cg} ,\qquad(4.2)$$

Where σ is flow stress, $\dot{\varepsilon}$ is strain rate, k is Boltzmann's constant, and M_{cg} ($\partial \ln \sigma_{cg}/\partial \ln \dot{\varepsilon}$) and M_c($\partial \ln \tau_c/\partial \ln \dot{\varepsilon}$) can be treated as constants [64,67]. This equation expresses a linear relationship between the strain rate sensitivity and grain size in the form of $d^{-1/2}$, similar to the well-known Hall-Petch equation. It follows that the strain rate sensitivity increases with decreasing grain size. Since the grain size in the AZ31B-H24 base metal was smaller (Fig. 4.1(a)), the strain rate sensitivity would be higher, as shown in Fig. 4.7.After laser welding, the strain rate sensitivity became relatively weaker, as demonstrated by the small increase of the YS and UTS and the slight decrease in the ductility with increasing strain rate (Fig. 4.7). Another reason for the reduction in the tensile properties after welding is related to the formation of new crystallographic texture in the weld zone as reported by Park *et al.* [62]. Further studies on the texture change after laser welding are needed.
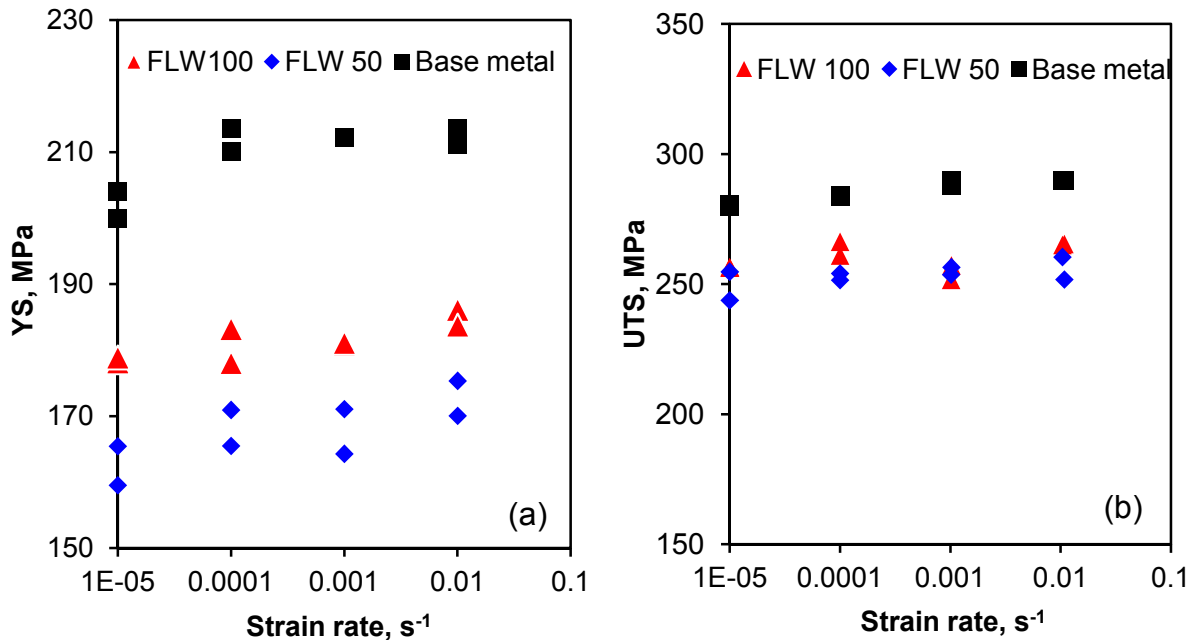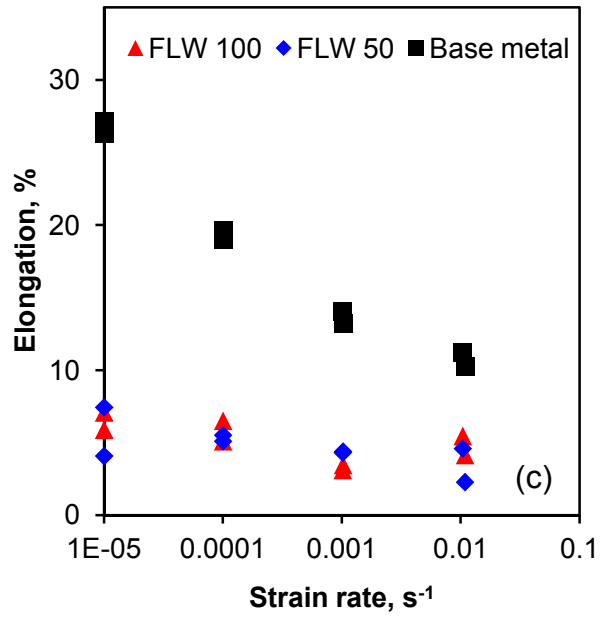
Fig.4.7 Effect of strain rate on (a) yield strength (YS), (b) ultimate tensile strength (UTS), and (c) ductility of the AZ31B-H24 base metal, fiber laser welded joints made at a welding speed of 50 mm/s and 100 mm/s.

Table 4.1 Joint efficiency for the welded joints of different Mg alloys.

Material condition	Welding process	Base metal		Welding parameter	Welded joint		Joint efficiency, %	Ref.
		YS, MPa	UTS, MPa		YS, MPa	UTS, MPa		
AMC602 extruded sheet	Fiber laser welding	-	250	3000 W-66.67~166.67 mm/s	-	209~220	84~88	[19]
AZ31-H24	Friction stir welding	208	309	1000 rpm-4 mm/s	-	201	65	[53]
AZ31-H24	Diode laser welding	209	285	3000 W-8.33 mm/s	91	169	59	[82]
AZ31-H24	Double sided arc welding	209	285	1400 W-25 mm/s	128	236	83	[84]
	Friction Stir Welding	209	285	1000~2000 rpm 10~30 mm/s	120~161	212~239	74~84	
AZ31 wrought	CO_2 laser welding	-	315	800~1000 W 25~41.66 mm/s		205~305	65~96	[43]
AZ31-H24	Friction stir welding	227.6	307.7	1500~2000 rpm 1.3~3.4 mm/s	94.9~115.3	200~225.6	65~73	[54]
AM50	Friction stir welding	117	260	-	110	224	86	[94]
AZ31B	Gas tungsten arc welding	171	215	3 mm/s	148	183	85	[95]
	Friction stir welding			1600 rpm - 0.66 mm/s	171	208	95	
	CO_2 laser welding			2500 W-91.66 mm/s	174	212	97	

4.4 Strain hardening behavior

The fiber laser welding was anticipated to affect the strain (or work) hardening characteristics of AZ31B-H24 Mg alloy as well. The hardening capacity of a material, H_c, has been defined as a normalized parameter [58],

$$H_c = \frac{\sigma_{UTS} - \sigma_y}{\sigma_y} = \frac{\sigma_{UTS}}{\sigma_y} - 1,$$ (4.3)

where σ_y is the yield strength, and σ_{UTS} is the ultimate tensile strength of a material. The obtained hardening capacity of the base metal and the fiber laser welded samples is listed in Table 4.2. The hardening capacity increased after fiber laser welding, especially for the fiber laser welded samples at a lower welding speed of 50 mm/s. There was little effect of strain rate on the hardening capacity. A decrease in the grain size would increase the YS as indicated by the Hall-Petch relationship [96], since it reduced the difference of the flow resistance between the grain boundary and interior, which in turn lowered the hardening capacity [97]. Since the grain size of the fiber laser welded samples at a welding speed of 50 mm/s (Fig. 4.1(c) and 4.1(f)) was larger than that of the fiber laser welded samples at a welding speed of 100 mm/s (Fig. 4.2(b) and 4.2(e)), a higher value of hardening capacity in the fiber laser welded samples at a welding speed of 50 mm/s is expected. Another way of understanding the strain hardening behavior is to determine the strain hardening exponent, since it is a measure of the ability of a material to strain harden; the larger its value, the greater the strain hardening for a given amount of plastic strain. A few equations have been proposed to evaluate the strain hardening exponent. Hollomon [98] proposed the following expression,

$$\sigma = K\varepsilon^n,$$ (4.4)

Table 4.2 Yield strength, ultimate tensile strength, hardening capacity and strain hardening exponents of the base metal and fiber laser welded samples of AZ31B-H24 Mg alloy tested at different strain rates.

Specimen	Welding speed, mm/s	Strain rate, s^{-1}	YS, MPa	UTS, MPa	Hardening capacity	n-value	n_1-value	n^*-value
Base metal	-	1×10^{-2}	212	289	0.37	0.113	0.371	0.368
		1×10^{-3}	212	288	0.36	0.117	0.387	0.347
		1×10^{-4}	211	283	0.36	0.111	0.392	0.358
		1×10^{-5}	201	280	0.41	0.118	0.395	0.357
Fiber laser welding	50	1×10^{-2}	172	256	0.48	0.229	1.306	0.646
		1×10^{-3}	167	255	0.52	0.229	1.223	0.624
		1×10^{-4}	168	252	0.50	0.214	1.407	0.760
		1×10^{-5}	162	249	0.54	0.208	1.073	0.581
Fiber laser welding	100	1×10^{-2}	184	265	0.43	0.234	1.196	0.584
		1×10^{-3}	181	254	0.41	0.221	1.411	0.627
		1×10^{-4}	180	263	0.46	0.181	0.997	0.548
		1×10^{-5}	178	256	0.44	0.174	0.988	0.544

Where n is the strain hardening exponent, K is the strength coefficient, σ is the true stress and ε is the true strain. To better quantify the strain hardening response, Chen and Lu [99] fitted their tensile curves using the Ludwik equation [100],

$$\sigma = \sigma_y + K_1 \varepsilon^{n1}, \qquad (4.5)$$

where n_1 is the strain hardening exponent and K_1 is the strength coefficient which represents the increment in strength due to strain hardening at $\varepsilon = 1$. Afrin *et al.* [58] proposed the following equation by considering only the net flow stress and net plastic strain of a material after yielding,

$$\sigma = \sigma_y + K^*(\varepsilon - \varepsilon_y)^{n^*}, \qquad (4.6)$$

where n^*, σ, ε, σ_y and ε_y are the strain hardening exponent, true stress, true strain, yield strength and yield strain of a material, respectively. K^* is the strength coefficient which reflects the increment in strength due to strain hardening corresponding to $(\varepsilon - \varepsilon_y) = 1$. The strain hardening exponents evaluated according to the above three equations are shown in Fig. 4.8(a), (b) and (c) for the base metal, fiber laser welded joints made at a welding speed of 50 mm/s and 100 mm/s as a function of strain rate. Only the data lying in-between the YS and UTS were used to evaluate the value of n, n_1 and n^*. Almost no effect of strain rate on the strain hardening exponents was seen in the base metal. But for the fiber laser welded samples, the strain hardening exponents increased with increasing strain rate. It is also shown that the n values were the smallest and n_1 values were the highest with n^* lying in-between the two values. The strain hardening exponents evaluated corresponding to all the above three equations were obviously higher after welding, and the fiber laser welded joints made at 50 mm/s exhibited higher strain hardening exponents than the fiber laser welded joints made at 100 mm/s, as shown in Fig. 4.8.
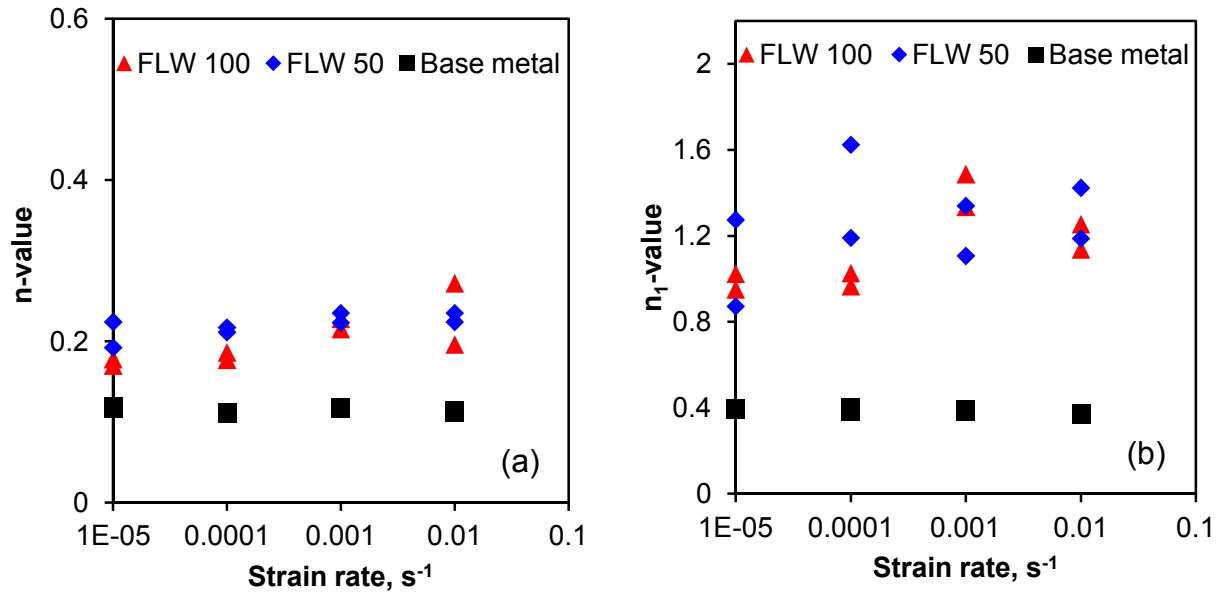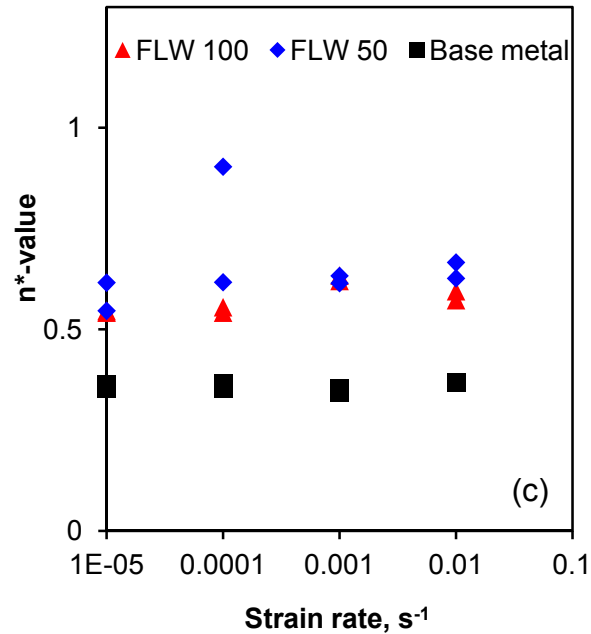
Fig.4.8 Effect of strain rate on the strain hardening exponent (a) *n*-value, (b) n_1, and (c) *n**-value of the AZ31B-H24 base metal, fiber laser welded joints made at a welding speed of 50 mm/s and 100 mm/s.

One of the important contributions to the strain hardening is associated with the formation and multiplication of dislocations. In the plastic deformation stage, the net flow stress in relation to the dislocation density could be expressed as [58,65,66],

$$\sigma - \sigma_y \propto \sqrt{\rho} \tag{4.7}$$

Where ρ is the dislocation density. The net flow stress necessary to continue deformation of a material is proportional to the square root of the dislocation density. The dislocation density in a metal increased with the amount of deformation or cold work due to dislocation multiplication or the formation of new dislocations which in turn decreased the spacing among dislocations and their interactions became repulsive. The net result would be that the movement of a dislocation

was blocked by other dislocations. As the dislocation density increased, the resistance to dislocation movement by other dislocations became more pronounced. Then a higher stress was necessary to deform a material [96]. Fig. 4.9 shows a typical Kocks-Mecking plot of strain hardening rate ($\theta = \mathrm{d}\sigma/\mathrm{d}\varepsilon$) vs. net flow stress ($\sigma$-$\sigma_y$) in the base metal, fiber laser welded samples at a welding speed of 50 mm/s and 100 mm/s tested at a strain rate of 1×10^{-5} s^{-1}. It is seen that stage III hardening occurred after yielding followed by stage IV hardening for both the base metal and fiber laser welded joints. The strain hardening could be understood as a result of the grain size strengthening and dislocation strain hardening [58,65,66],

$$\sigma = \sigma_o + \sigma_{HP} + \sigma_d \,, \tag{4.8}$$

Where σ_o is the frictional contribution, $\sigma_{HP} = kd^{-1/2}$is the Hall-Petch contribution, and $\sigma_d = M\alpha Gb\rho^{1/2}$ is the Taylor dislocation contribution (where G is the shear modulus, b is the Burgers vector, M is the Taylor factor and α is a constant). Sinclair $et\ al.$ [101] and Kovacs $et\ al.$ [102] reported that at lower strains the grain size had a strong contribution to the strain hardening and the influence of the grain size on the strain hardening petered out at higher strains due to dislocation screening and dynamic recovery effects at grain boundaries. Because the base metal had a smaller grain size (Fig. 4.1(a)), the Hall-Petch contribution (σ_{HP}) would be stronger at lower strains, leading to a somewhat higher initial strain hardening rate in comparison to the welded joints. Similar results were reported by Balik $et\ al.$ [103]. Fig. 4.9 further shows that the steepness (or slope) of stage III became increasingly flatter from the base metal to the fiber laser welded joint at 100 mm/s and to that at 50 mm/s, implying that the decrease in the strain hardening rate with increasing net flow stress was more enduring.
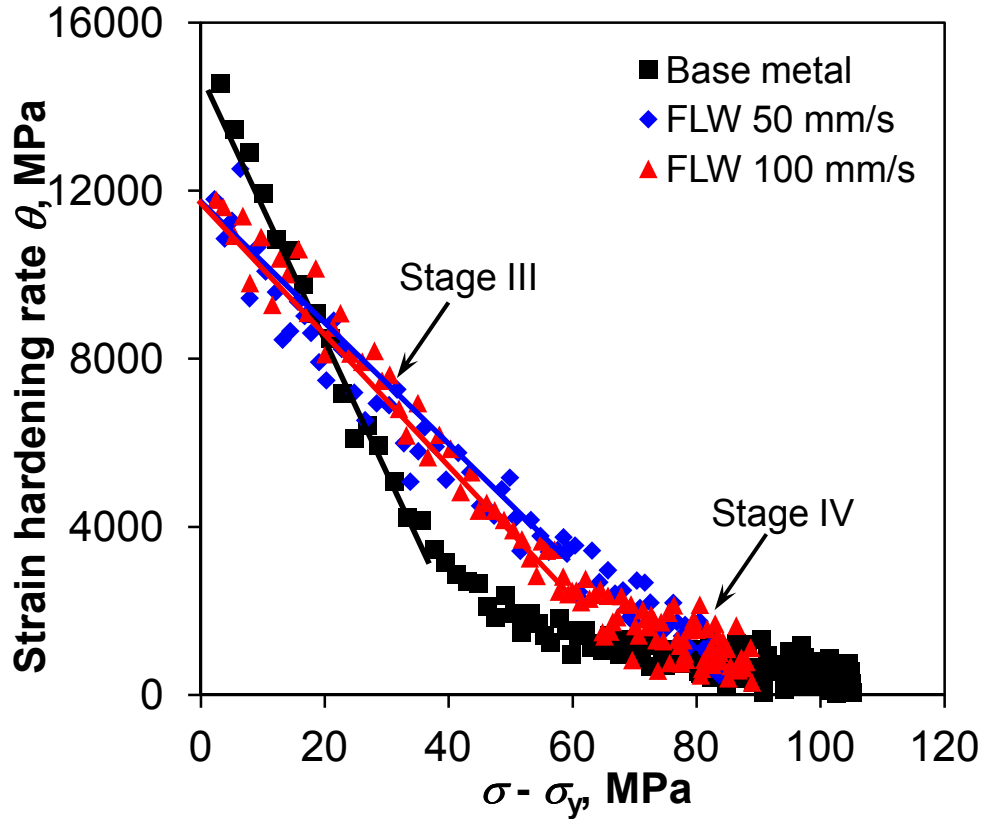
Fig.4.9 Strain hardening rate (θ) as a function of net flow stress (σ-σ_y) of the base alloy, fiber laser welded samples at a welding speed of 50 mm/s and 100 mm/s tested at a strain rate of 1×10^{-5} s^{-1}.

4.5 Fatigue strength

Fig. 4.10 (a) shows S-N curves obtained at R=0.1, 50 Hz and room temperature for the AZ31B-H24 base metal, fiber laser welded joints made at a welding speed of 50 mm/s and 100 mm/s. Similar to the tensile properties (Fig. 4.7), the fatigue life decreased after laser welding, and the fatigue life of the fiber laser welded joints made at a welding speed of 100 mm/s was basically longer than that of the fiber laser welded joints made at a welding speed of 50 mm/s.
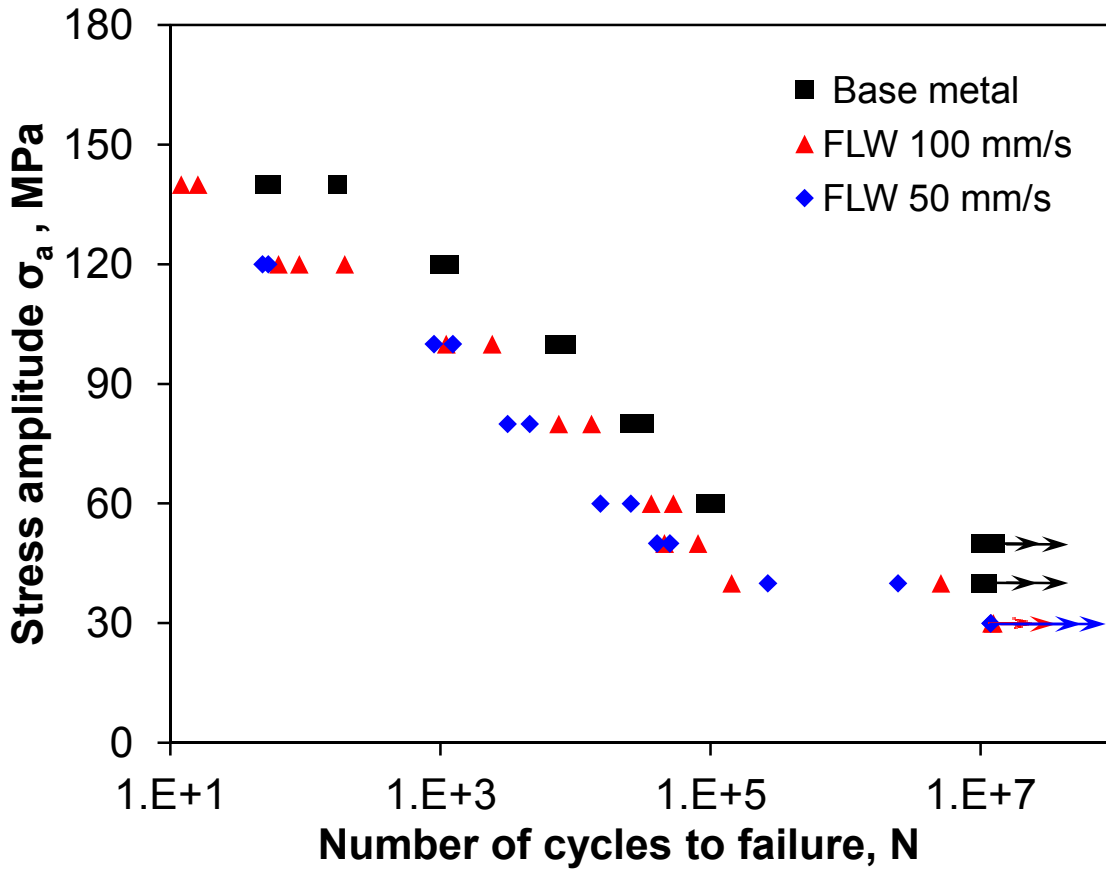
Fig.4.10 S-N curves of the AZ31B-H24 base metal, fiber laser welded joints made at a welding speed of 50 mm/s and 100 mm/s tested at R=0.1, 50 Hz and room temperature. (a) Stress amplitude (σ_a) vs. the number of cycles to failure (N_f) in the semi-log scale.

The obtained fatigue limit (i.e., the fatigue strength at 1×10^7 cycles) and fatigue ratio (the ratio of fatigue limit to UTS) of the base metal and fiber laser welded joints are listed in Table 4.3. The fatigue limit of the fiber laser welded samples at a welding speed of 50 mm/s and 100 mm/s dropped by about 40%, and the fatigue ratio for both fiber laser welded joints decreased by about 32% and 35% relative to that of the base metal. This indicates that the welded joints were more susceptible to the dynamic fatigue loading than quasi-static tensile loading (Table 4.2) where both the YS and UTS exhibited only a moderate reduction after fiber laser welding.

Table 4-3 Fatigue limit, fatigue ratio, fatigue strength coefficient $\sigma_f^{'}$ and fatigue strength exponent b of the base metal and fiber laser welded joints of the AZ31B-H24 Mg alloy tested at R=0.1, 50 Hz and room temperature, where more test data for the welding speed of 100 mm/s are included in the fitting in comparison with our earlier publication [82].

Specimen	Welding speed, mm/s	Fatigue limit, MPa	Fatigue ratio	$\sigma_f^{'}$, MPa	b
Base metal	-	50	0.173	246	-0.105
Fiber laser welding	50	30	0.117	222	-0.121
Fiber laser welding	100	30	0.115	218	-0.113

Again, the decrease in the fatigue resistance after welding was mainly attributed to the microstructural change, as illustrated in Fig. 4.1 and 4.2. The following Basquin-type equation [104] can be used to fit the obtained fatigue data,

$$\sigma_a = \sigma_f^{'}(2N_f)^b, \tag{4.9}$$

where σ_a is the cyclic stress amplitude, $\sigma_f^{'}$ is the fatigue strength coefficient defined by the stress intercept at $2N_f=1$, N_f is the number of cycles to failure, and $2N_f$ is the number of reversals to failure, and b is the fatigue strength exponent which, varying normally between -0.05 and -0.12 for most of the metals, is a predominant factor for estimating the fatigue life of materials. Based on equation (9), a smaller value of b (in the absolute value) corresponds to a longer fatigue life. It is shown from Fig. 4.10(b) that equation (4.9) could be used to characterize the fatigue data

obtained in the present study. It should be noted that the run-out data for which no failure occurred at or over 1×10^7 cycles were not included in the fitting. The obtained b and $\sigma_f^{'}$ values are listed in Table 4.3. It is shown that the absolute value of fatigue strength exponent, b, was in the following sequence: base metal < fiber laser welded joints made at a welding speed of 100 mm/s < fiber laser welded joints made at a welding speed of 50 mm/s. This corresponded well to the longer fatigue life for the base metal and shorter fatigue life for the fiber laser welded joints made at a welding speed of 50 mm/s, while the fiber laser welded joints made at a welding speed of 100 mm/s lay in-between them, as shown in Fig. 4.10(a) and 4.10(b). The longer fatigue life observed in the fiber laser welded samples at a higher welding speed of 100 mm/s was mainly due to the smaller grain sizes in both fusion zone (Fig. 4.2(b) vs. 4.1(c)) and heat-affected zone (Fig. 4.2(e) vs. 4.1(f)), in conjunction with the presence of divorced eutecticβ-$Mg_{17}Al_{12}$particles in the fusion zone. This was consistent with the higher hardness across the weld (Fig. 4.5) and tensile strength (Fig. 4.7) in the welded joint made at a higher welding speed. Similar results were also obtained by Padmanaban and Balasubramanian [105], where the superior fatigue properties of AZ31 magnesium welded joints made using a 2.5 kW CO_2 laser were associated with the formation of smaller grains in weld region, higher fusion zone hardness and uniformly distributed finer precipitates.
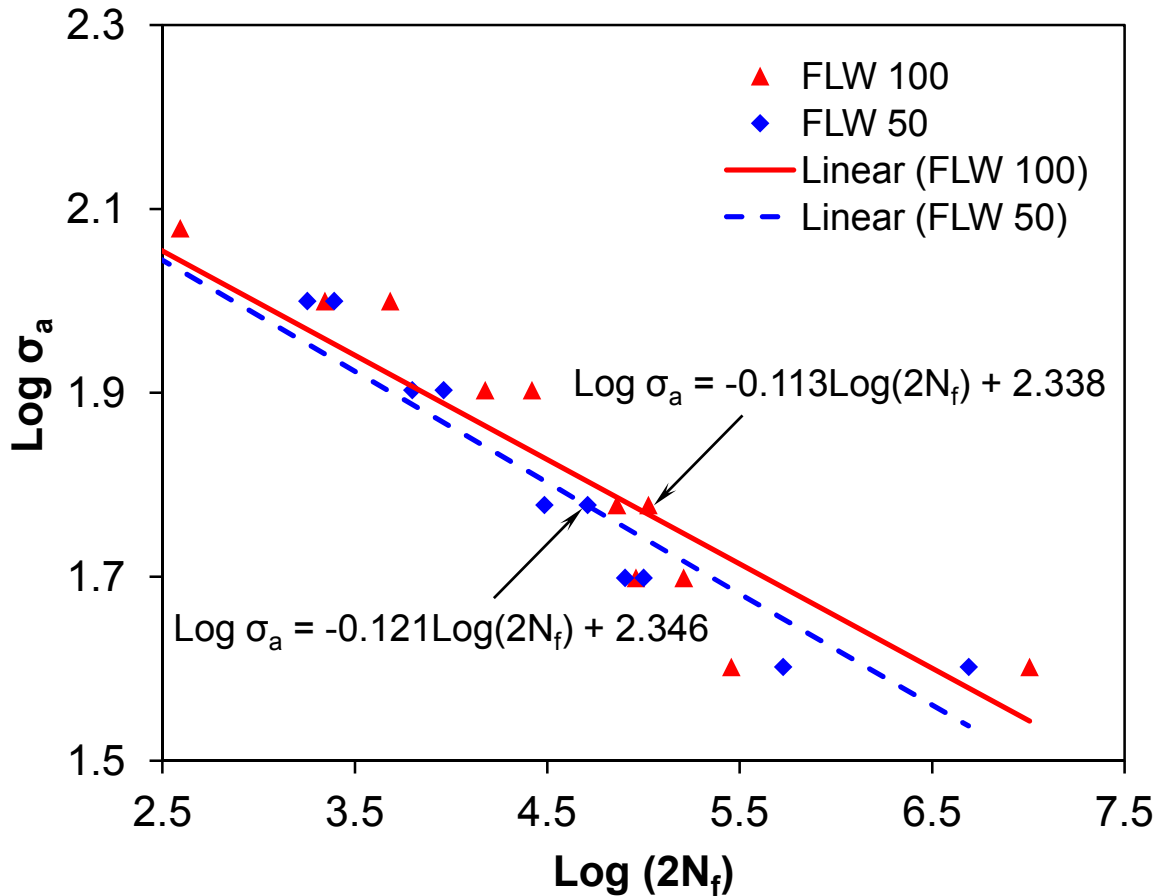
Fig.4.10 S-N curves of the AZ31B-H24 base metal, fiber laser welded joints made at a welding speed of 50 mm/s and 100 mm/s tested at R=0.1, 50 Hz and room temperature. (b) stress amplitude (σ_a) vs. the number of reversals to failure ($2N_f$) in the double-log scale.

4.6 Fractography

Tensile fracture was observed to occur usually from the welding pores or defects in the fusion zone, corresponding well to the lowest hardness shown in Fig. 4.5. Fig. 4.11 shows typical SEM images of the tensile fracture surfaces of the fiber laser welded joints at a welding speed of 50 mm/s and 100 mm/s tested at a strain rate of 1×10^{-4} s^{-1}. The tensile fracture surface characteristics were similar at both welding speeds. A number of small pores, believed to stem

from the air or hydrogen trapped at the solidifying front in the fusion zone during keyhole fiber laser welding, were evident as indicated by arrows in Fig. 4.11(a) and 4.11(c), leading to the decreased tensile and fatigue strength especially ductility (%El) after welding (Fig. 4.7 and 4.10).Some ductile tear ridges together with some cleavage-like brittle fracture characteristics appeared on both fracture surfaces of the welded samples as shown in Fig.4.11(b) and 4.11(d). The fractographic observations corresponded well to the relatively low ductility of ~4% elongation in the fiber laser welded samples (Fig. 4.7(c)).
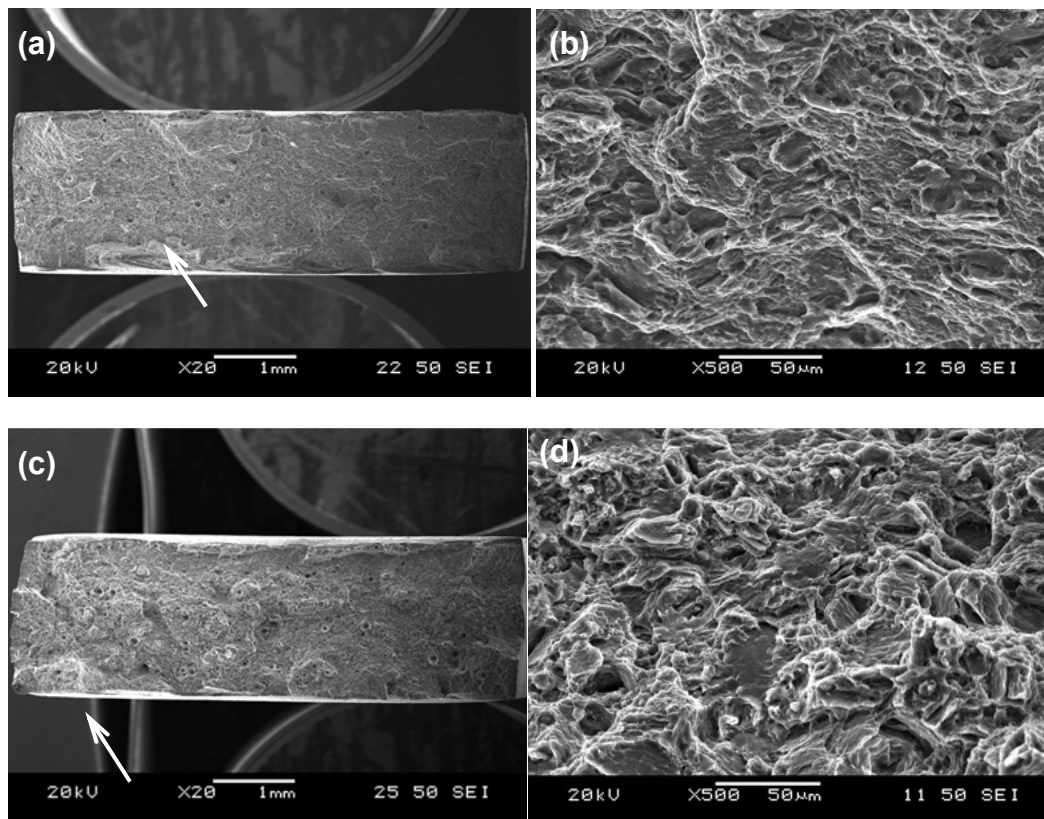
Fig.4.11 Typical SEM images showing the fracture surfaces after tensile testing at a strain rate of 1×10^{-4} s^{-1}, (a) overall view of the entire fracture surface and (b) magnified view at a higher magnification of the fiber laser welded joint at a welding speed of 50 mm/s, (c) overall view of the entire fracture surface, and (d) magnified view at a higher magnification of the fiber laser welded joint at a welding speed of 100 mm/s.

Fig. 4.12 and 4.13 show SEM images of fatigue fracture surfaces of the fiber laser welded joints made at a welding speed of 50 mm/s and 100 mm/s, respectively. Fatigue cracking essentially initiated from the welding defects at or near the surface (Fig. 4.12(a)-(c) and Fig. 4.13(a)-(c)), irrespective of the applied cyclic stress level. Such welding defects were considered to form due to marginal incision or depression of molten pool during solidification [106], or other processing issues such as spatter, sag, undercut, unstable weld pool, liquation and solidification cracking, unstable weld pool, oxide inclusions and loss of alloying elements [107]. At both welding speeds, welding defects and small pores were observed (Fig. 4.12(b), (c) and (e), and Fig. 4.13(b), (c) and (e)). Yu *et al.* [108] has suggested that the formation of the small pores was closely related to the stability of the keyhole and the oscillation of the molten pool during the fiber laser welding. The tip of the keyhole was so tiny that it could be readily closed by the flow of molten metal and formed as a bubble. A bubble usually became a gas cavity in the weld bead, because it was often difficult for bubbles to escape from the molten pool at high solidification rates of laser welding due to the fast cooling [108]. At both welding speeds, single crack initiation basically occurred from the surface defect and failure occurred perpendicular to the loading direction at lower stress amplitudes (Fig. 4.12(a), the lower sample in Fig. 4.12(f), Fig. 4.13(a)), while multiple crack initiation sites were more obvious at higher stress amplitudes as shown in Fig. 4.12(b) and 4.13(b) with fracture occurred mainly at ~45° shear to the loading direction (the upper sample in Fig. 4.12(f)). Even without surface welding defects, surface grains were usually less constrained than the internal grains, thus the occurrence of slip in a few grains near the specimen surface became relatively easier during fatigue [109]. Fatigue crack propagation was mainly characterized by fatigue striations (Fig. 4.12(d) and 4.13(d)) along with

secondary cracks, which appeared usually perpendicular to the fatigue crack propagation direction.
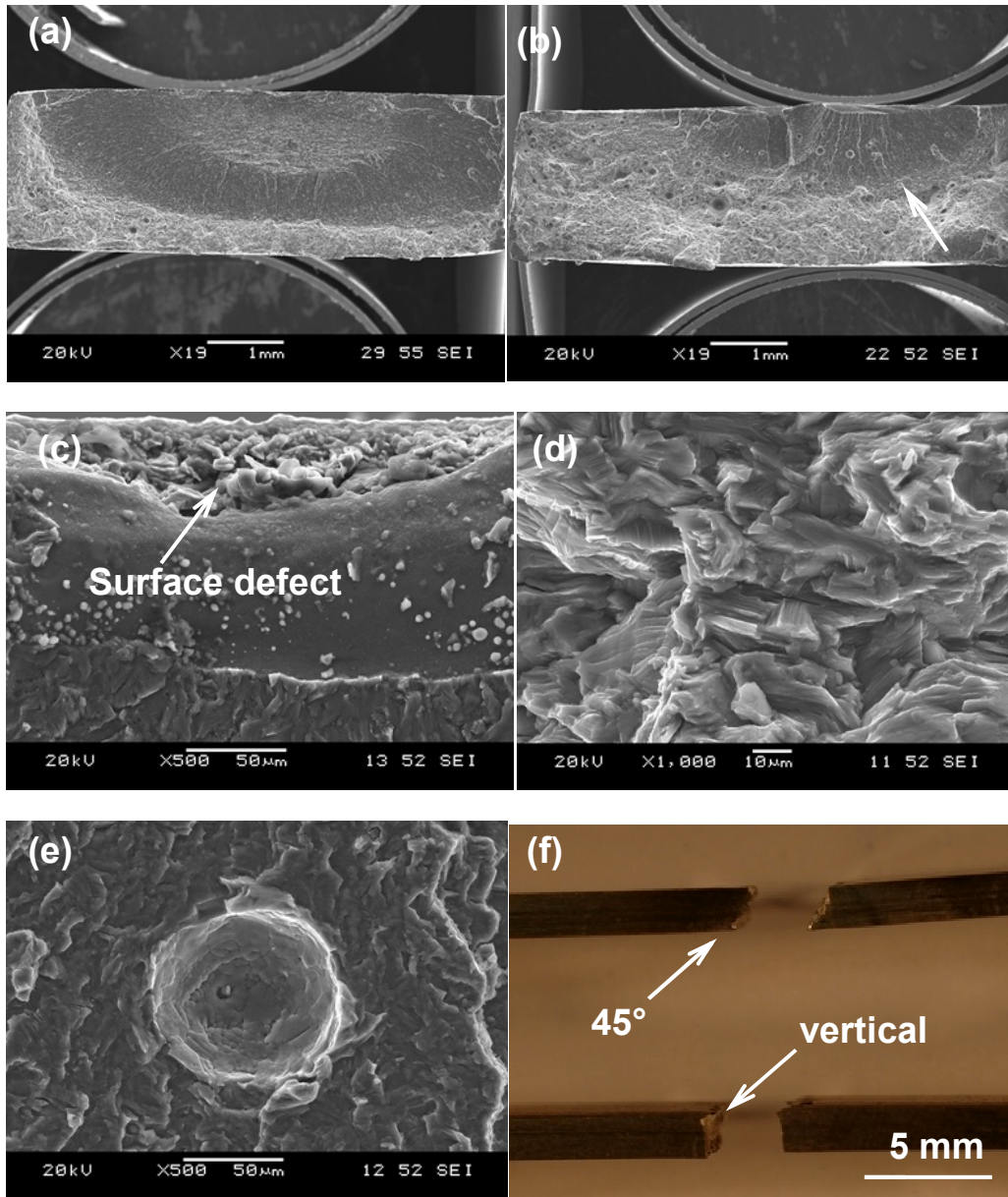
Fig.4.12 Typical SEM images of fatigue fracture surface of fiber laser welded joint at a welding speed of 50 mm/s. (a) overall view of the entire fracture surface at a lower stress amplitude of 40 MPa, (b) multiple crack initiation at a higher stress amplitude of 80 MPa, (c) crack initiation site at a welding defect, (d) fatigue striations at a higher magnification in the propagation area, and (e) a gas pore at a higher magnification as indicated by an arrow in (b) and (f) failure pattern at lower and higher stress amplitudes.
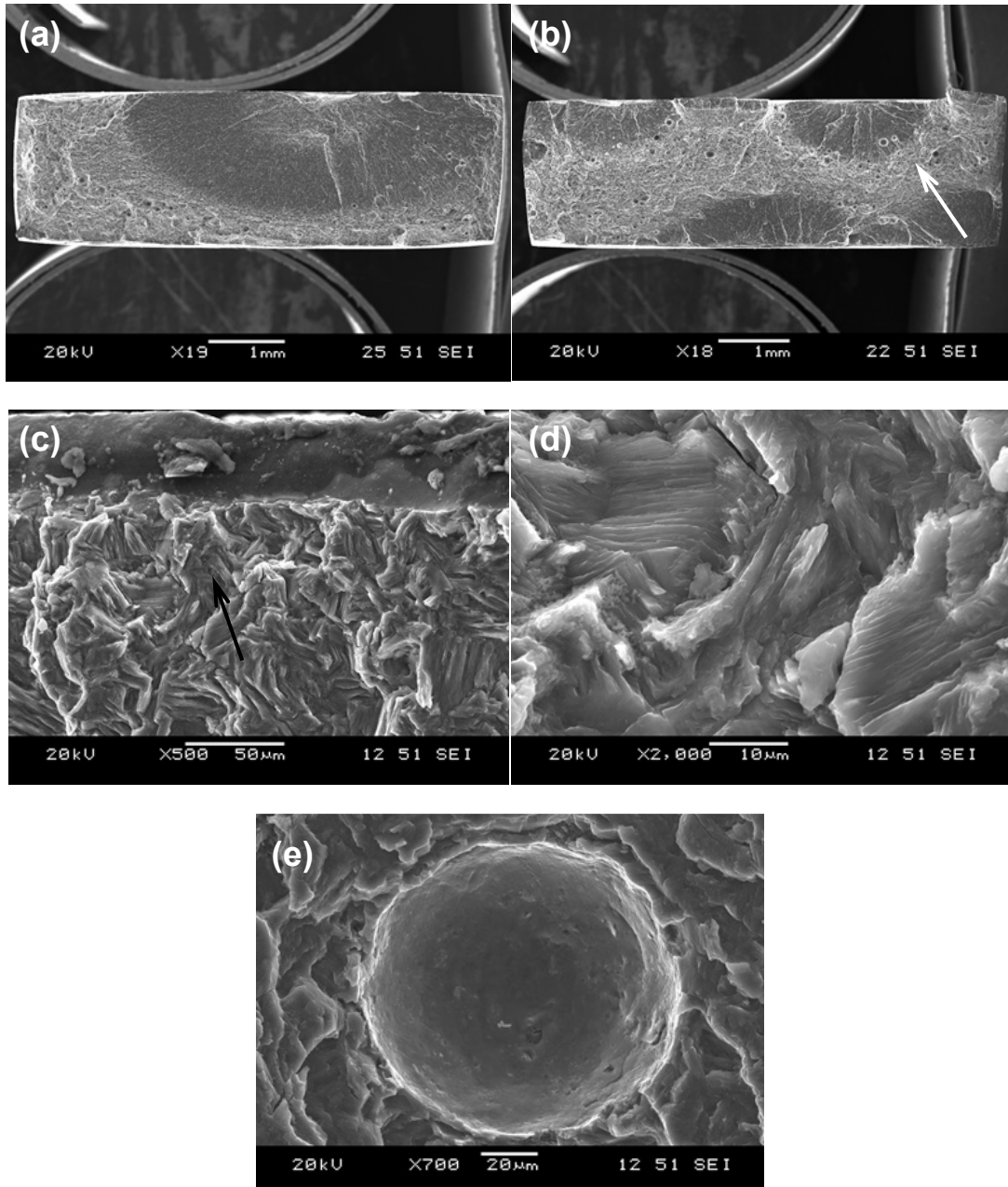
Fig.4.13 Typical SEM images of fatigue fracture surface of fiber laser welded joint at a welding speed of 100 mm/s. (a) overall view of the entire fracture surface at a lower stress amplitude of 40 MPa, (b) multiple crack initiation at a higher stress amplitude of 80 MPa, (c) crack initiation from a surface defect, (d) fatigue striations at higher a magnification in the propagation area as indicated by an arrow in (c), (e) a small pore at a higher magnification as indicated by an arrow in (b).

The fatigue striations normally occurred by a repeated plastic blunting-sharpening process in the face-centered cubic materials due to the slip of dislocations in the plastic zone ahead of the fatigue crack tip [110]. The formation of fatigue striations in the magnesium alloys with a hexagonal close-packed crystal structure was expected to be additionally associated with the occurrence of twinning-detwinning process [111,112], since the number of slip systems in magnesium alloys was limited at room temperature. Further studies of this aspect are needed.

CHAPTER 5

FRICTION STIR WELDED AZ31 MAGNESIUM ALLOY: MICROSTRUCTURE, TEXTURE, AND TENSILE PROPERTIES

5.1 Microstructure

A typical macroscopic image of the welded cross-section is shown in Fig. 5.1. The SZ, TMAZ and heat-affected zone (HAZ) could be identified and the microstructural changes would be expected. The microstructure of the AZ31B-H24 BM, as shown in Fig. 5.2(a), consisted of deformed/twinned and somewhat elongated grains with varying sizes. The heterogeneity in such a grain structure of the BM was due to both heavy deformation by rolling to become a 2 mm thick sheet and incomplete dynamic recrystallization (partial annealing) in the H24 condition [47,52,53,58]. The average grain size of the BM was about 3.6 ± 2.2 µm.

The effect of the welding speed and tool rotational rate on the microstructure in the SZ is shown in Fig. 5.2(b) $\rightarrow$ Fig. 5.2(d). It is seen that, in comparison with the BM microstructure (Fig.5.2(a)), considerable microstructural changes occurred after FSW, with the SZ consisting of an equiaxed grain structure with smooth boundaries, irrespective of the welding speed and rotational rate (Fig.5.2(b)-(d)). This was attributed to the occurrence of dynamic recrystallization that arose from a combination of frictional heating, intense plastic deformation, and viscous dissipation due to the rotation of the welding tool during FSW. Similar results have been reported in [51,52,553,58]. The grain size was observed to decrease with increasing welding speed (Fig.5.2(b) $\rightarrow$ Fig.5.2(c)) but increased with increasing rotational rate (Fig.5.2(c) $\rightarrow$ Fig.5.2(d)). Such a microstructural evolution could be rationalized on the basis of heat input during FSW. Since heat input decreased with increasing welding speed and decreasing rotational

rate, a shorter time or lower peak temperature was available for grain growth at a higher welding speed or at a lower tool rotation rate, which resulted in a smaller grain size. Similar results have been obtained for the thicker (5 mm in thickness) friction stir welded (FSWed) AZ31B-H24 Mg alloy [52,53,58] as well as FSWed 6061 and 7075 Al alloys [113-115].
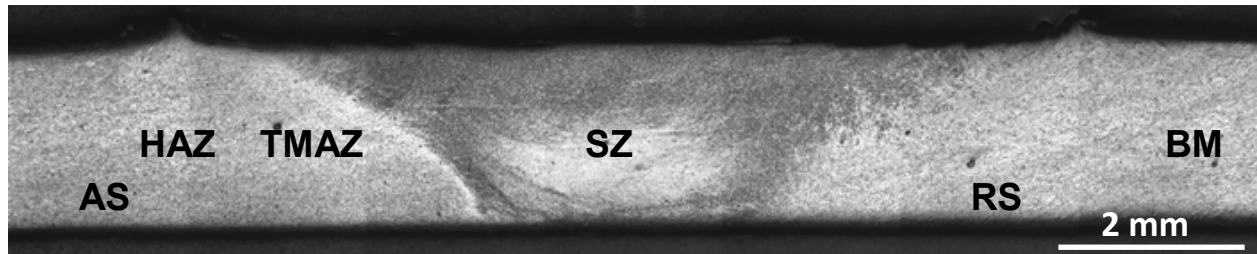
Fig.5.1 A typical macroscopic image of the welded cross-section.
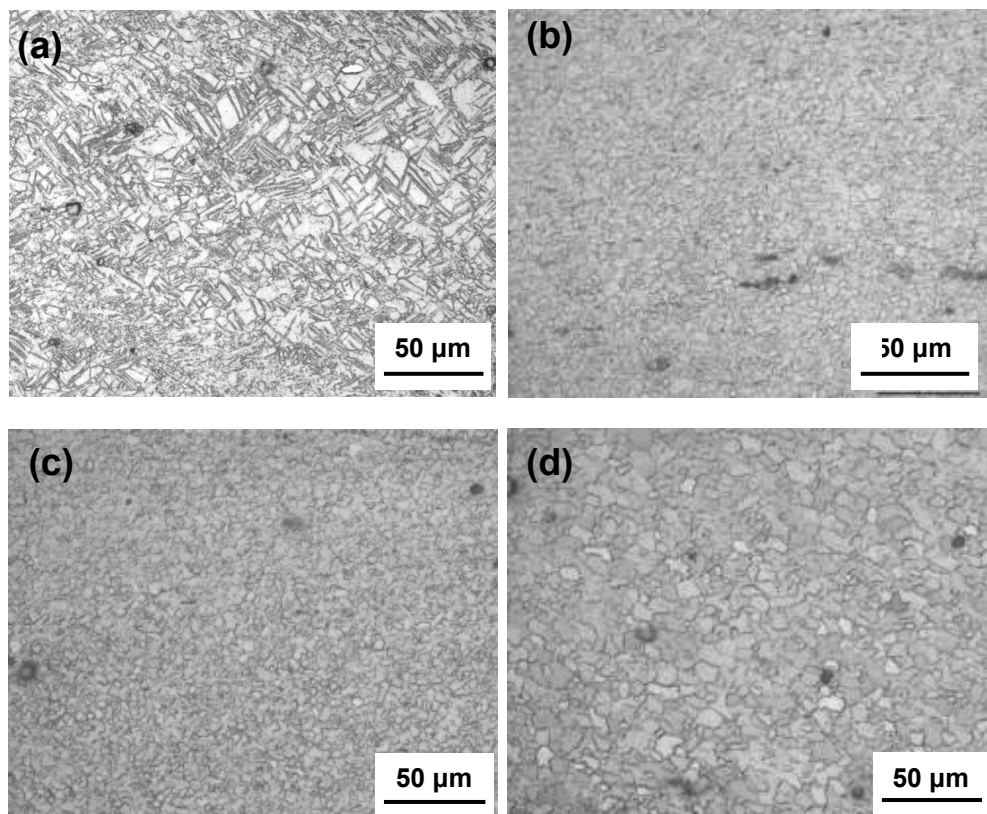
Fig.5.2 Typical microstructures of a FSWed joint made at different rotational rates and welding speeds.(a) AZ31B-H24 BM, (b) SZ at 1000 rpm and 5 mm/s, (c) SZ at 1000 rpm and 20 mm/s, and (d) SZ at 2000 rpm and 20 mm/s.

Some particles were also seen in the SZ of the FSWed joints (Fig.5.3(a)). EDS analysis revealed that these particles were undissolved Mn- and Al-containing inclusions (Fig.5.3(b)), which still remained in the SZ. While the peak temperature during FSW was high enough to bring about the occurrence of dynamic recrystallization (Fig.5.2(b)-(d)), it would be far below the melting point of the Mn- and Al-containing inclusions which were pre-existent in the AZ31B-H24 Mg base alloy. Such inclusions were indeed observed to be present in the fusion zone after laser welding [82], double-sided arc welding [84], and resistance spot welding of Mg alloy [36,38], where the weld liquid pool would have a higher temperature than the solid-state SZ during FSW. Furthermore, Xiao *et al.* [36] reported that the undissolved Mn-Al (Al_8Mn_5) second-phase particles could promote a more efficient nucleation and lead to a finer grain size in the fusion zone of a Mg resistance spot weld.
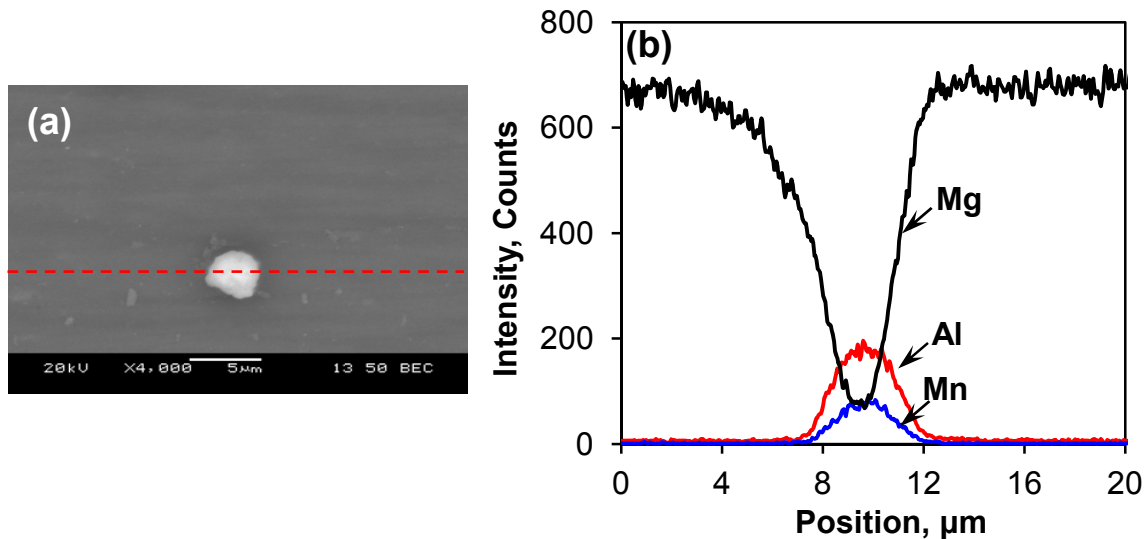
Fig.5.3 (a) SEM micrograph of a particle in the SZ of the FSWed Mg alloy joint made at a welding speed of 5 mm/s and tool rotational rate of 1000 rpm, (b) EDS line scan across the particle in (a) showing Al and Mn compositional variations across the particle.

5.2 Crystallographic texture

The (0002), (10$\bar{1}$0), and (10$\bar{1}$1) pole figures for a FSWed joint made at a welding speed of 5 mm/s and tool rotational rate of 1000 rpm are shown in Fig. 5.4. Fig. 5.4(a)-(c) indicates the pole figures obtained at different locations (A, B, C, D, and E) from the top surface of the sheet, while Fig. 5.4(d) indicates the pole figures from the cross section of the sheet, where A and B were positioned at 30 mm and 5 mm from the centre of the SZ (i.e., location C) at the advancing side (AS), while D and E were located at 5 mm and 35 mm from the centre of the SZ at the retreating side (RS). It is seen that in the BM (position A and E) and position B and D, the basal plane (0002) normal was largely parallel to the ND with some grains slightly tilted in the RD (Fig. 5.4(a)), and the <10$\bar{1}$0> and <10$\bar{1}$1> directions were aligned or tilted in the TD (Fig. 5.4(b) and (c)). It has been reported that two major types of texture components, (0002)<11$\bar{2}$0> and (0002)<10$\bar{1}$0>, are available, depending on the activation of slip systems in the basal plane (either <11$\bar{2}$0> single slip or <10$\bar{1}$0> double slip oriented in the RD) in the Mg alloys [116,117]. In the present study (0002)< 11$\bar{2}$0> texture component was mainly observed. Similar (0002)< 11$\bar{2}$0> texture component in the AZ31 Mg alloy has also been reported in [118-120]. In the SZ there was a weak tendency for the basal plane (0002) normal to tilt toward the TD, as seen from position C in Fig. 5.4(a). Such a texture change occurred in the SZ was attributed to the intense localized shear plastic flow near the stirring shoulder at the trailing side during FSW. The (0002), (10$\bar{1}$0), and (10$\bar{1}$1) pole figures obtained from the cross section at different locations are shown in Fig 4(d). Similar to the previous studies [121,122], the BM had a strong texture with the basal plane (0002) normal parallel to the TD while in the stir zone there was a weak tendency for the basal plane (0002) normal to tilt toward the RD (location C). It is well known that the basal plane (0002) in the SZ tended to distribute around the pin surface due to the shear plastic

flow arising from the pin rotation which made the parent material to rotate around the threaded

pin surface [123]. The orientation of the basal plane (0002) after FSW in different regions of the

welded joints was reported in several studies [51,62,124], where the basal plane (0002) normal in

the SZ was reported to be relocated in-between TD and ND after FSW. This is in agreement with

the present study in which the basal plane (0002) had an inclination in-between the TD and ND,

as shown in Fig. 4(d).Since the preferential slip plane of Mg alloy with a hexagonal close-packed

structure is known to be basal plane (0002) plane for plastic deformation at room temperature

[125], the change in the texture may affect the tensile properties of the FSWed AZ31B-H24 Mg

alloy. As seen from location C in Fig.5.4(b), most prismatic planes $(10\bar{1}0)$ in the SZ were

oriented toward RD in a concentric circular pattern at 90° from the centre of the pole figure,

indicating the formation of basal fiber texture(c-axis in the normal direction) which is also known

as crystallographic fibering produced by crystallographic reorientation of the grains during

deformation [104,126,127]. The maximum pole densities of prismatic planes $(10\bar{1}0)$ shifted from

the TD to the RD was related to the localized plastic deformation in the SZ. The crystallographic

fibering in the SZ could even be better seen from the pyramidal plane $(10\bar{1}1)$ at location C in

Fig.5.4(c), where the normal of pyramidal planes $(10\bar{1}1)$ formed a nearly complete ring at

approximately 45° from the center of the pole figure with more $(10\bar{1}1)$ pole densities distributed

parallel to the TD. Some degree of pyramidal planes $(10\bar{1}1)$ fibering characteristics at D

positioned near the TMAZ/HAZ boundary is also seen in Fig.5.4(c). This was attributed to the

intense stirring plastic flow occurred in the welded region, as also reported by Park *et al.* [62] in

a 6.3 mm thick wrought AZ61 Mg alloy after FSW. For Mg alloys, the critical resolved shear

stress for the basal plane (0002) slip system is much lower than that of prismatic plane $(10\bar{1}0)$

slip system and pyramidal plane $(10\bar{1}1)$ slip system at room temperature [128]. Therefore, only

basal slip would be anticipated when the FSWed Mg alloy was plastically deformed at room temperature, while both the basal and non-basal slip systems might operate during hot deformation at temperatures higher that about 600 K (326.85 °C) [125]. Besides, compared to the BM there was no significant change in the prismatic planes ($10\bar{1}0$) and pyramidal planes ($10\bar{1}1$) in the SZ, except more obvious fiber texture characteristics, as shown Fig 4(d).
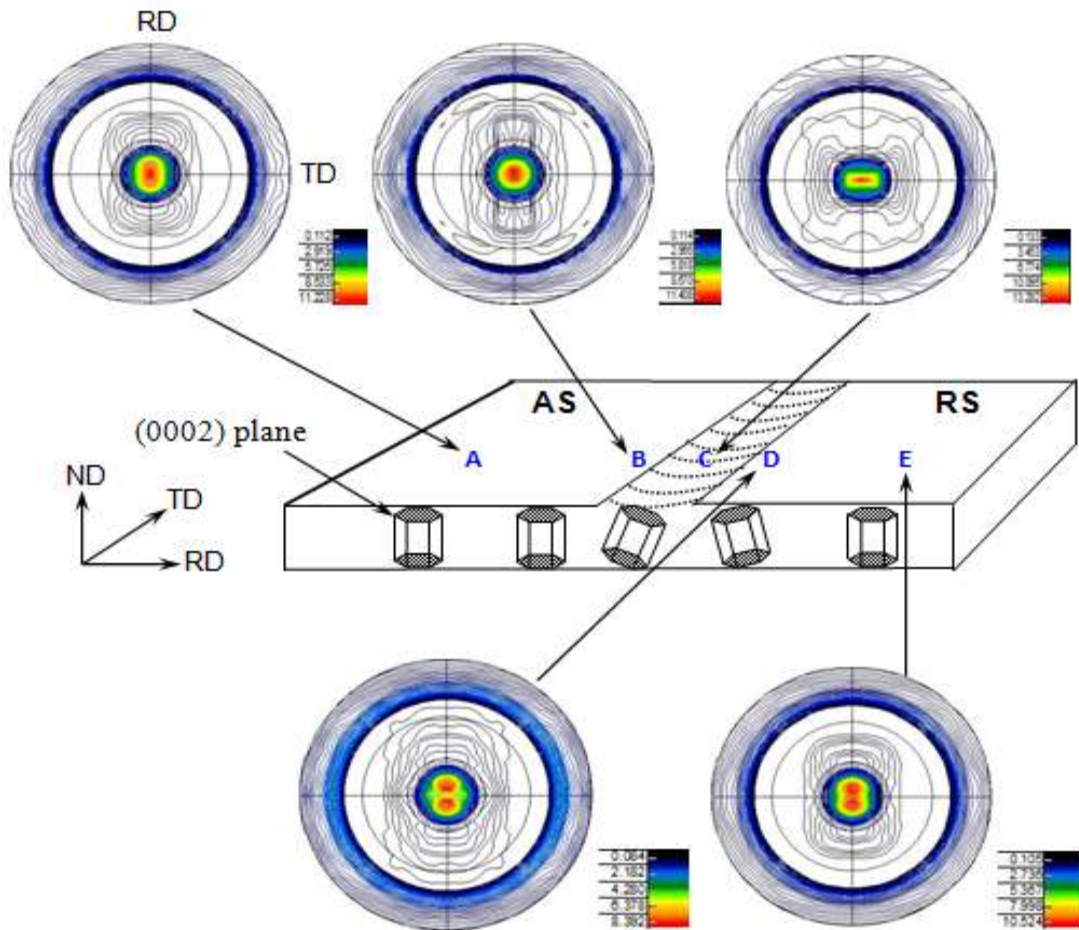
Fig. 5.4(a)

Fig.5.4 Pole figures of a FSWed joint made at a welding speed of 5 mm/s and tool rotational rate of 1000 rpm at different locations. (a) Basal (0002) from the top surface, (b) prismatic ($10\bar{1}0$) from the top surface, (c) pyramidal ($10\bar{1}1$) from the top surface, and (d) basal, prismatic and pyramidal planes from the cross section.
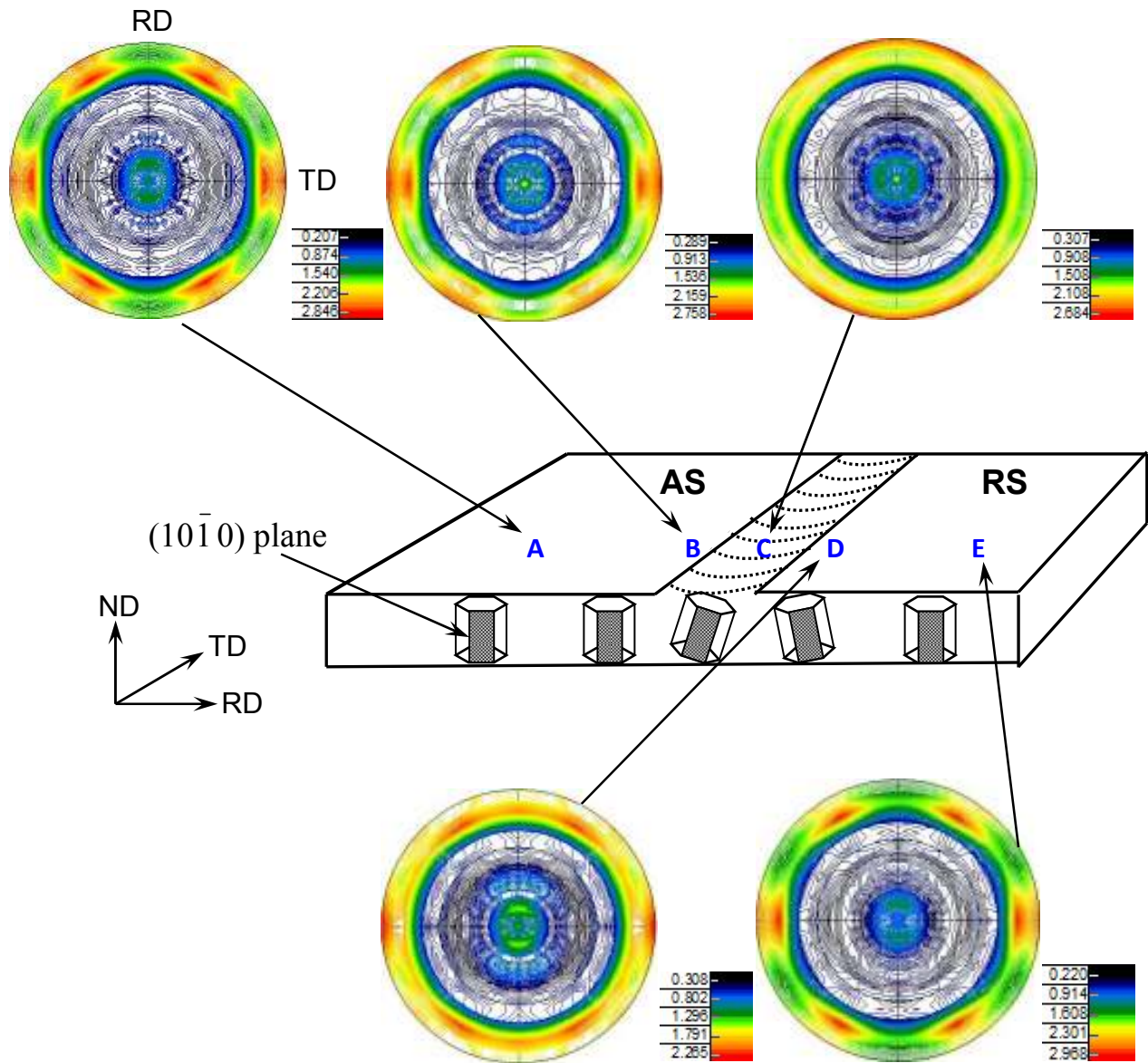
Fig. 5.4(b)

Fig.5.4 Pole figures of a FSWed joint made at a welding speed of 5 mm/s and tool rotational rate of 1000 rpm at different locations. (a) Basal (0002) from the top surface, (b) prismatic ($10\bar{1}0$) from the top surface, (c) pyramidal ($10\bar{1}1$) from the top surface, and (d) basal, prismatic and pyramidal planes from the cross section.
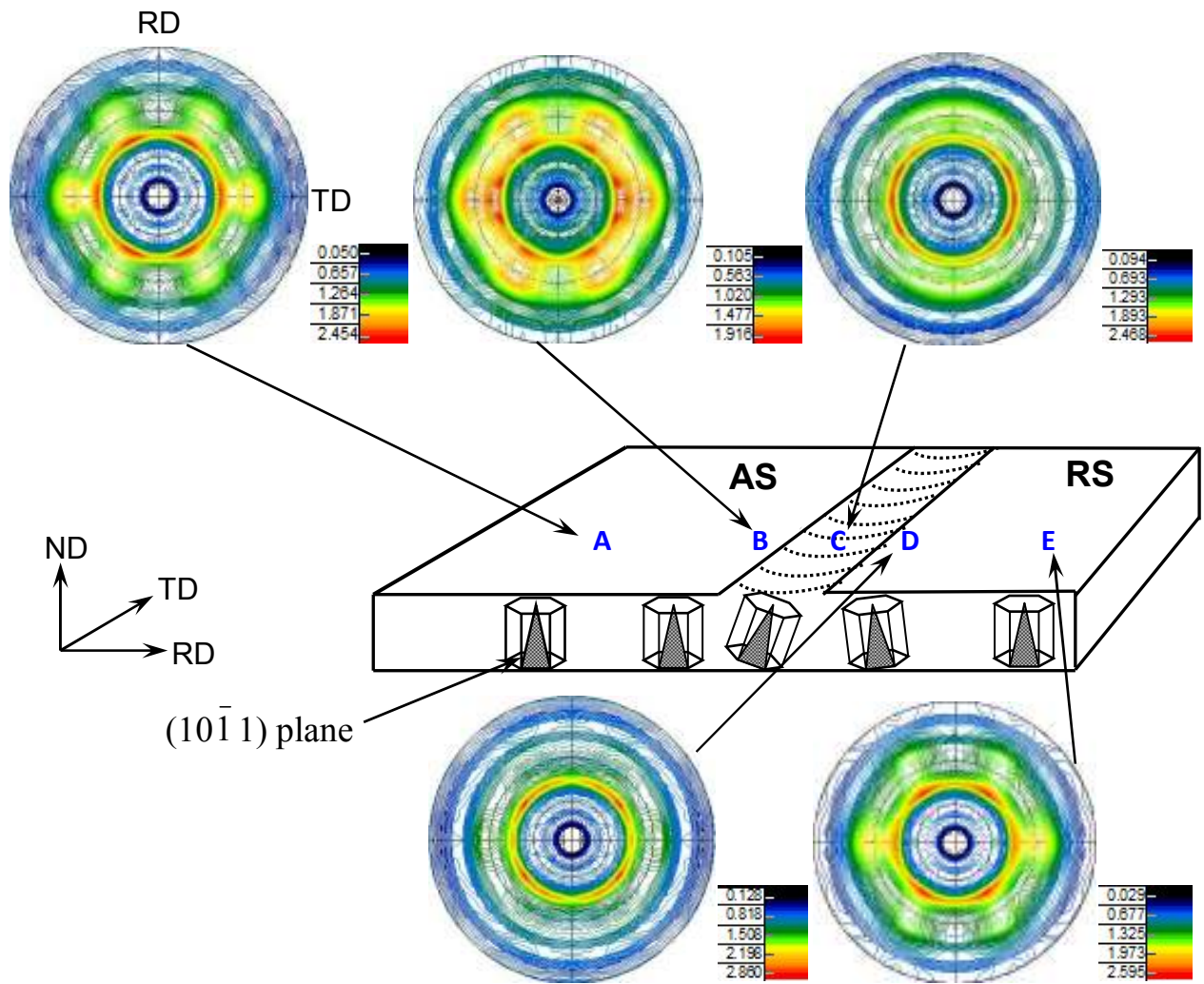
Fig. 5.4(c)

Fig.5.4 Pole figures of a FSWed joint made at a welding speed of 5 mm/s and tool rotational rate of 1000 rpm at different locations. (a) Basal (0002) from the top surface, (b) prismatic ($10\bar{1}0$) from the top surface, (c) pyramidal ($10\bar{1}1$) from the top surface, and (d) basal, prismatic and pyramidal planes from the cross section.

Basal plane (0002)
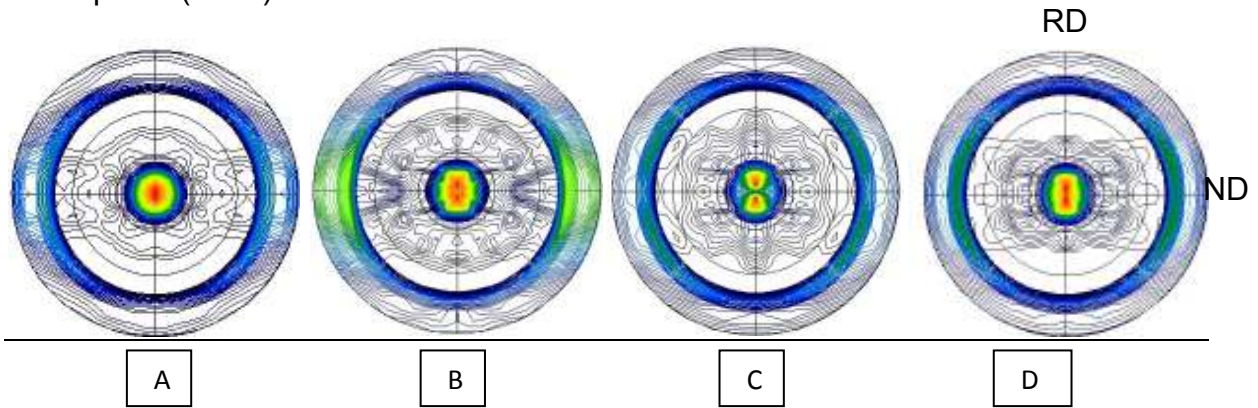
Prismatic plane (10$\bar{1}$0)
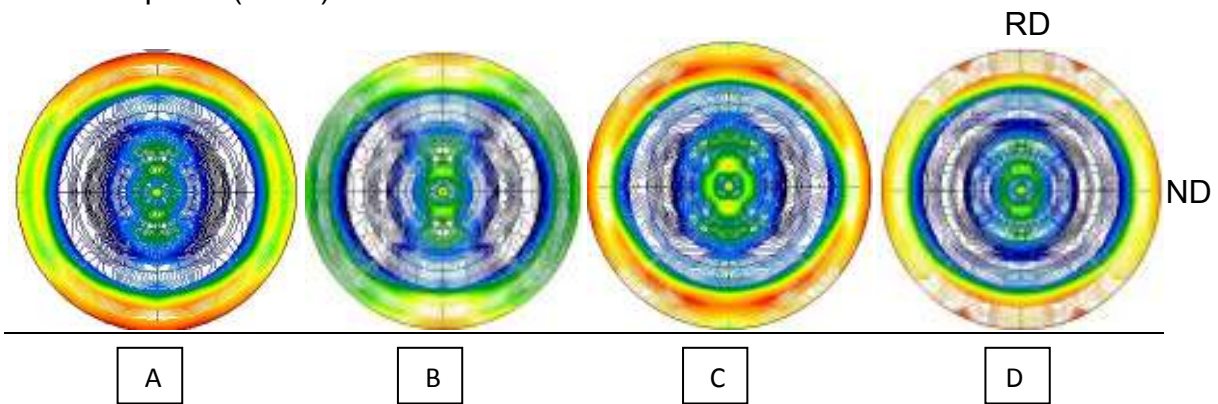
Pyramidal plane (10$\bar{1}$1)
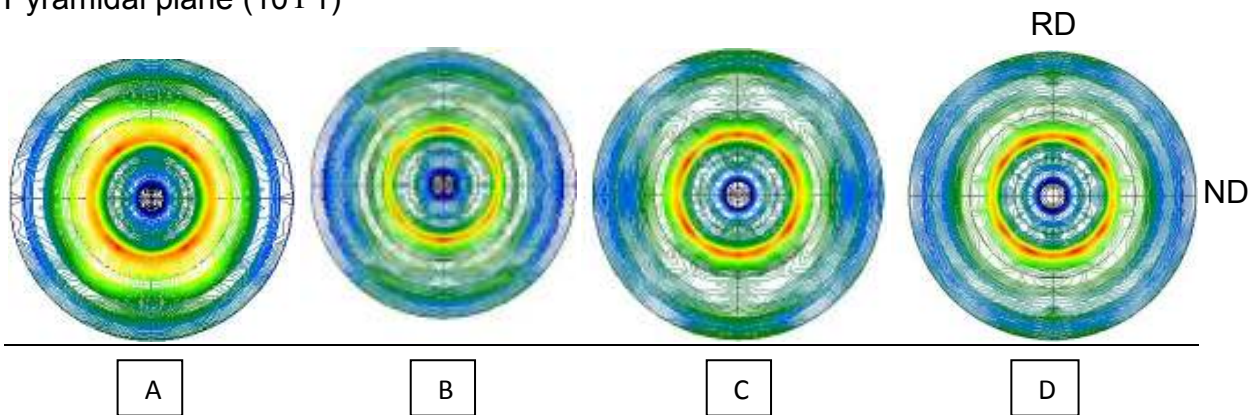
Fig. 5.4(d)

Fig.5.4 Pole figures of a FSWed joint made at a welding speed of 5 mm/s and tool rotational rate of 1000 rpm at different locations. (a) Basal (0002) from the top surface, (b) prismatic (10$\bar{1}$0) from the top surface, (c) pyramidal (10$\bar{1}$1) from the top surface, and (d) basal, prismatic and pyramidal planes from the cross section.

The effect of welding speed and tool rotational rate on the texture is shown in Fig. 5.5, where the basal (0002), prismatic ($10\bar{1}0$) and pyramidal ($10\bar{1}1$) pole figures were obtained from the center of the SZ (i.e., location C indicated in Fig.5.4) for the FSWed joint made at a welding speed of 20 mm/s and rotational rate of 1000 rpm (Fig.5.5(a)) and the FSWed joint made at a welding speed of 20 mm/s and rotational rate of 2000 rpm (Fig.5.5(b)). It is seen from these pole figures that similar texture changes occurred in the AZ31B-H24 Mg alloy after FSW. However, the relative texture intensity in the SZ was different, which is summarized in Table 5.1. It is clear that after FSW the basal plane (0002) was significantly intensified especially at a welding speed of 20 mm/s and rotational rate of 1000 rpm, while there was only a small change in the maximum relative pole intensity for both prismatic planes ($10\bar{1}0$) and pyramidal planes ($10\bar{1}1$) planes. With increasing rotational rate or decreasing welding speed, the maximum (0002) and ($10\bar{1}0$) pole intensities decreased. This was due to the fact that the higher tool rotational rate or lower welding speed generated a higher temperature in the SZ, which resulted in more complete dynamic recrystallization. This would in turn lead to a relatively weaker or more random orientation. Similar observations were also reported in the FSWed AZ31B billet and extruded plate [70], where more random orientation at higher rotational rates was observed.
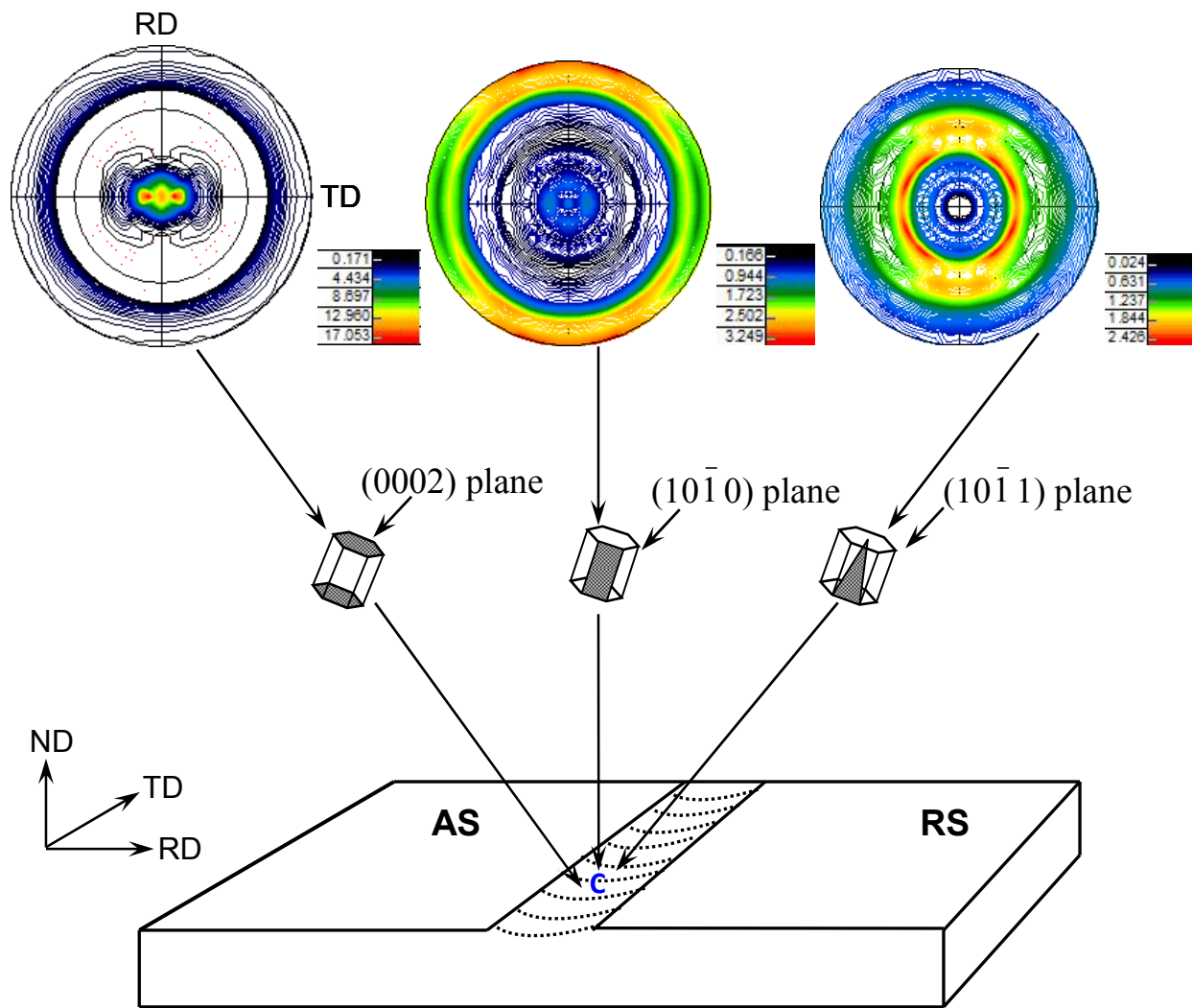
Fig. 5.5(a)

Fig.5.5 Basal plane (0002), prismatic plane (10$\bar{1}$0), and pyramidal plane (10$\bar{1}$1) pole figures at the center of SZ (position C) in a FSWed joint made at a welding speed of 20 mm/s and tool rotational rate of (a) 1000 rpm and (b) 2000 rpm.
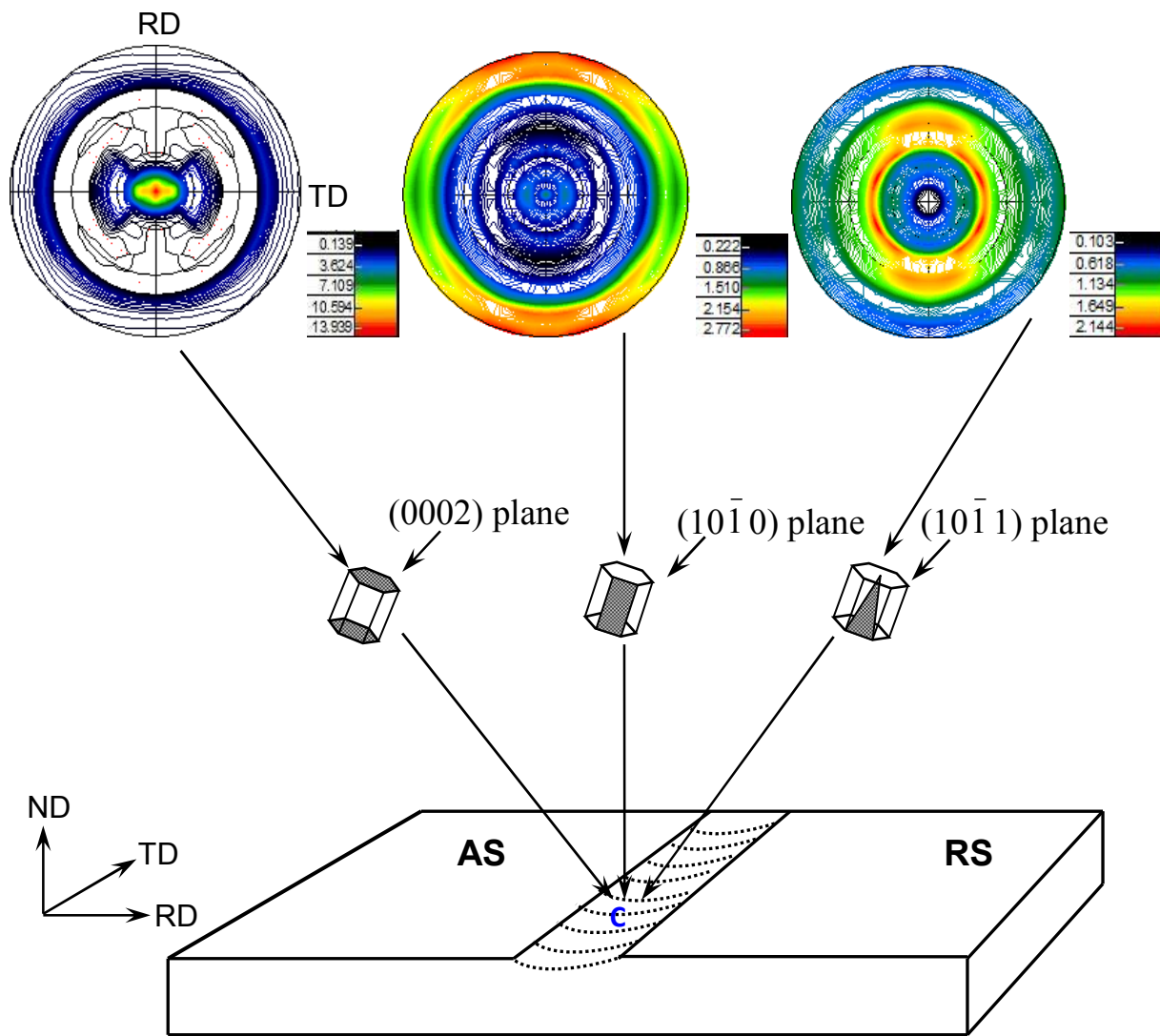
Fig. 5(b)

Fig.5.5 Basal plane (0002), prismatic plane (10$\bar{1}$0), and pyramidal plane (10$\bar{1}$1) pole figures at the center of SZ (position C) in a FSWed joint made at a welding speed of 20 mm/s and tool rotational rate of (a) 1000 rpm and (b) 2000 rpm.

Table 5-1 Effect of the welding speed and rotational rate on the maximum relative pole intensity in the FSWed AZ31B-H24 Mg alloy.

Test material	Welding speed, mm/s	Rotational rate, rpm	Maximum relative pole intensity		
			(0002)	$(10\bar{1}0)$	$(10\bar{1}1)$
Base metal	-	-	10.876*	2.907*	2.525*
FSWed joints	5	1000	13.282	2.684	2.468
	20	1000	17.053	3.249	2.426
	20	2000	13.939	2.772	2.144

* The maximum relative pole intensity for the BM was the average value from positions A and E indicated in Fig.5.4.

5.3 Microhardness

Fig. 5.6(a) and 6(b) shows the typical hardness profiles across the AZ31B-H24 weldments made with different welding parameters. It is seen that the hardness value decreased gradually from about HV 73 for the half-hardened H24 temper BM to approximately HV 62 at the center of the SZ through the HAZ and TMAZ of the welded joints. The decrease in the hardness was a consequence of a combined effect of the grain growth and the change of the material state from the H24 temper to recrystallzation state (Fig.5.2). The hardness in the SZ slightly varied from 84% to 86% of the BM hardness when the tool rotational rate decreased from 2000 rpm to 1000 rpm (Fig. 6(a)) and the welding speed increased from 5 mm/s to 20 mm/s (Fig. 6(b)). Similar changes in the microstructure and the resulting hardness were reported in [52,53,113-115,129].

The hardness of SZ in the weld was mainly associated with the heat input during FSW and the ensuing change in the grain size. Specifically, there was a strong grain size dependence for the microhardness, which followed the Hall-Petch type relationship in the welded AZ31B-H24 Mg alloy [52,53]. Since the grain boundaries were the main obstacle to the slip of dislocations, the microstructure with a smaller grain size would have a higher resistance to localized plastic deformation due to the presence of a greater number of grain boundary area that culminated to a higher hardness or strength [52]. Therefore, the hardness increase with decreasing rotational rate and increasing welding speed was attributed to the smaller sizes of recrystallized equiaxed grains formed in the SZ at a lower rotational rate from 2000 rpm to 1000 rpm (from Fig. 5.2(d) to Fig. 5.2(c)) while keeping the welding speed constant at 20 mm/s, and at a higher welding speed from 5 mm/s to 20 mm/s (from Fig. 5.2(b) to Fig. 5.2(c)) while maintaining the rotational rate constant at 1000 rpm. Another reason for the lower hardness in the SZ would be related to the texture variation. During FSW complex plastic deformation occurred in the welded region, and relatively more random orientation with more obvious fiber texture characteristics (Fig. 5.4(d)) was produced in the FSWed Mg alloy joints, i.e., the basal plane (0002) rotated around the stir pin, thereby producing a soft region around the SZ [62,130]. As a result, the low hardness value observed in the SZ of the FSWed joints in the present study was expected to be also associated with the local texture variation.
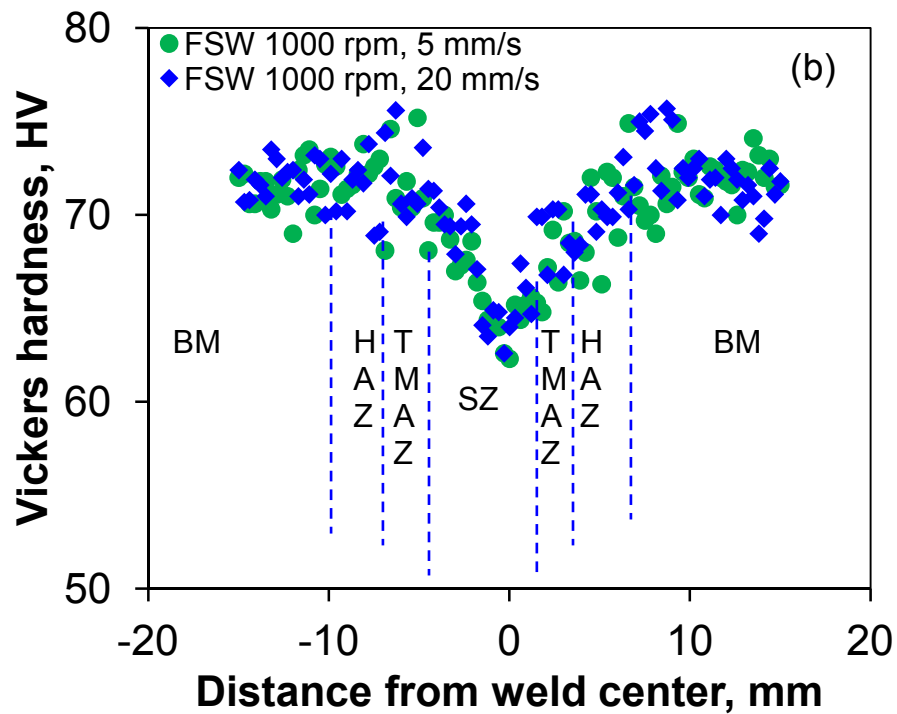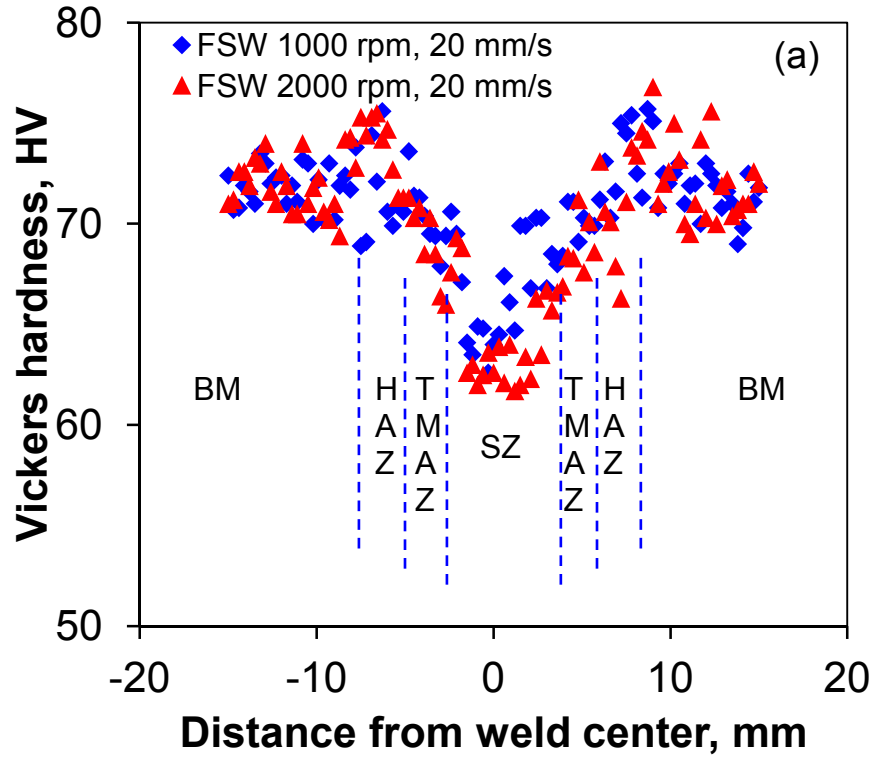
Fig.5.6 Typical microhardness profiles of the FSWed joints made with different welding parameters (a) 1000 rpm, 20 mm/s and 2000 rpm, 20mm/s, and (b) 1000 rpm, 5 mm/s and 1000 rpm, 20 mm/s.

5.4 Tensile properties

Fig. 5.7 shows typical engineering stress versus engineering strain curves of the BM and FSWed AZ31B Mg alloy joints made at different welding speeds and rotational rates tested at a strain rate of 1×10^{-2} s^{-1} at room temperature. It is seen that after FSW both the strength and elongation decreased. The yield strength (YS) and ultimate tensile strength (UTS) of the BM in the RD was obtained to be about 212 MPa and 285 MPa, respectively, which was approximately 6% higher than the minimum YS and UTS of 200 and 269 MPa, respectively, specified in ASTM B90-07 for the present thin gauge section sheet material in the H24 condition. A joint efficiency (i.e., a ratio of the UTS of the welded joints to the UTS of the base alloy) of the FSWed joints was obtained to lie in-between approximately 75% and 82%. The elongation after FSW was relatively low compared to the BM.
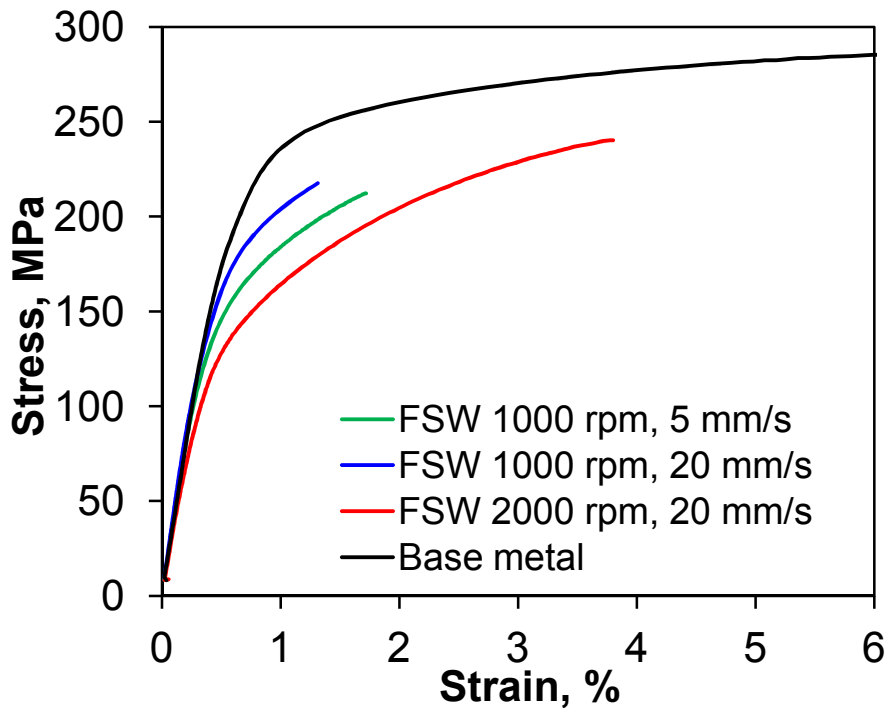
Fig.5.7 Typical engineering stress-strain curves of the AZ31B-H24 Mg base alloy and FSWed joints made with different welding parameters, tested at a strain rate of 1×10^{-2} s^{-1}.

Fig. 5.8 demonstrates the effect of strain rate on the tensile properties of the BM and FSWed joints at varying welding speeds and rotational rates. As expected, both the strength and ductility of the AZ31B-H24 Mg alloy after FSW decreased at all the strain rates. A slight increase of YS and UTS with increasing strain rate in the BM was observed (Fig.5.8(a) and (b)), while the ductility decreased dramatically (Fig.5.8(c)). After FSW the strain rate dependence of the tensile properties became weaker or nearly disappeared within the experimental scatter. The effect of the welding speed and rotational rate on the YS and UTS of the FSWed joints could be seen in Fig. 5.8(a) and Fig.5.8(b) as well. While the FSWed sample made at a rotational rate of 2000 rpm and welding speed of 20 mm/s exhibited a higher ductility of 4~5% elongation (Fig. 5.8(c)) (which was also close to the ductility of 6% specified in the ASTM B90-07 for the AZ31B-H24 Mg alloy), its YS dropped to become 130~135 MPa only, i.e., about 61-64% of the YS of BM. A significant increase in the YS to ~175 MPa (~83% of that of the BM) was achieved when the rotational rate decreased from 2000 rpm to 1000 rpm while keeping a constant welding speed of 20 mm/s (Fig.5.8(a)). However, a decrease in the welding speed from 20 mm/s to 5 mm/s at a constant tool rotational rate of 1000 rpm led to a drop in the YS back to ~155 MPa (~73% of that of the BM). The reason behind this could be explained by the heat generated during FSW. The total energy generated by the rotating pin tool to the workpiece (E_{total}), consisted of the energy due to the plastic deformation of the material ($E_{plastic}$) and the energy created by friction between the tool and workpieces ($E_{friction}$) [52,131]. During FSW lower heat was generated at a higher welding speed and/or lower rotational rate, leading to a smaller grain size of the FSWed joints (Fig. 5.2(c)). It is well known that the YS of a material at room temperature is dependent on the grain size according to the following Hall-Petch relationship,

$$\sigma_Y = \sigma_o + kd^{-1/2},$$
(5.1)

where σ_Y is the YS of the material, d is the grain size, σ_o is the "friction stress" representing the overall resistance of the crystal lattice to dislocation movement (or the YS corresponding to a material with infinitely large grain size, which is similar to that of a single crystal), and k is a constant called "locking parameter" reflecting the relative hardening contribution of grain boundaries as obstacles to the slip of dislocations across the grain boundaries [53,104,131]. Grain boundaries were the major obstacle to the slip of dislocations and the material with a smaller grain size would impose more restrictions to the dislocation movement and have a higher resistance to localized plastic deformation stemming from the presence of a greater number of grain boundaries that led to a higher YS. Since the grain size of the FSWed samples at a welding speed of 20 mm/s and rotational rate of 1000 rpm (Fig. 2(c)) was smaller than that of the FSWed samples at a welding speed of 5 mm/s and rotational rate of 1000 rpm (Fig. 2(b)) and FSWed samples at a welding speed of 20 mm/s and rotational rate of 2000 rpm (Fig. 2(d)), a higher value of YS in the FSWed samples at a welding speed of 20 mm/s and rotational rate of 1000 rpm would be expected. As shown in Fig. 5.8(b) the UTS increased with increasing welding speed and rotational rate as well. However, the extent of its increase was not so significant in comparison with the change in the YS. Similar results were observed by several researchers [47,53,55]. Besides the effect of grain sizes or grain boundaries, crystallographic orientation/texture distribution also strongly influenced the tensile strength since plastic deformation arose from the slip on the closed-packed basal planes with the minimum critical resolved shear stress as mentioned earlier. When the FSWed joints was deformed at room temperature along the RD (loading direction), the basal planes would rotate to lie parallel to the rolling sheet surface and the tensile axis. This might be a result of basal dislocation activity in favorably oriented grains. Similar correlation between the texture and tensile behavior for

FSWed of AZ31 alloy were reported by Yang *et al.* [124], Woo *et al.* [130,132], and Yu *et al.* [133]. In comparison with other two welding conditions, the stronger intensity of basal plane (0002) present in the low-hardness SZ at a welding speed of 20 mm/s and rotational rate of 1000 rpm (Table 5.1) implied that the basal planes were more oriented parallel to the rolling sheet surface, i.e., the basal plane normal of more grains was perpendicular to the sheet surface which resulted a stronger pole intensity. As a result, less extent of rotation of the basal planes was required during tensile deformation, leading to a higher YS (Fig.5.8(a)) and a lower ductility (Fig.5.8(c)). As shown in Fig. 5.7 and Fig. 5.8(c), the percent elongation increased with increasing rotational rate, which was in good agreement with the results reported in [53,58,134]. The hardening capacity (as discussed in Chapter 4) of the BM and the FSWed samples are evaluated by using Equation 4.3 listed in Table 5.2. It is seen that the hardening capacity of the FSWed samples made at a higher welding speed of 20 mm/s and higher rotational rate of 2000 rpm was about twice the hardening capacity of the BM. While the hardening capacity of the FSWed samples made at a welding speed of 5 mm/s and rotational rate of 1000 rpm was slightly higher than that of BM, it became lower for the FSWed samples made at a welding speed of 20 mm/s and rotational rate of 1000 rpm than for the BM. To understand the strain hardening behavior in an alternative way, the strain hardening exponent of different materials was evaluated. The strain hardening exponent is a measure of the ability of a metal to strain harden; the larger its magnitude, the greater the strain hardening for a given amount of plastic strain [96].
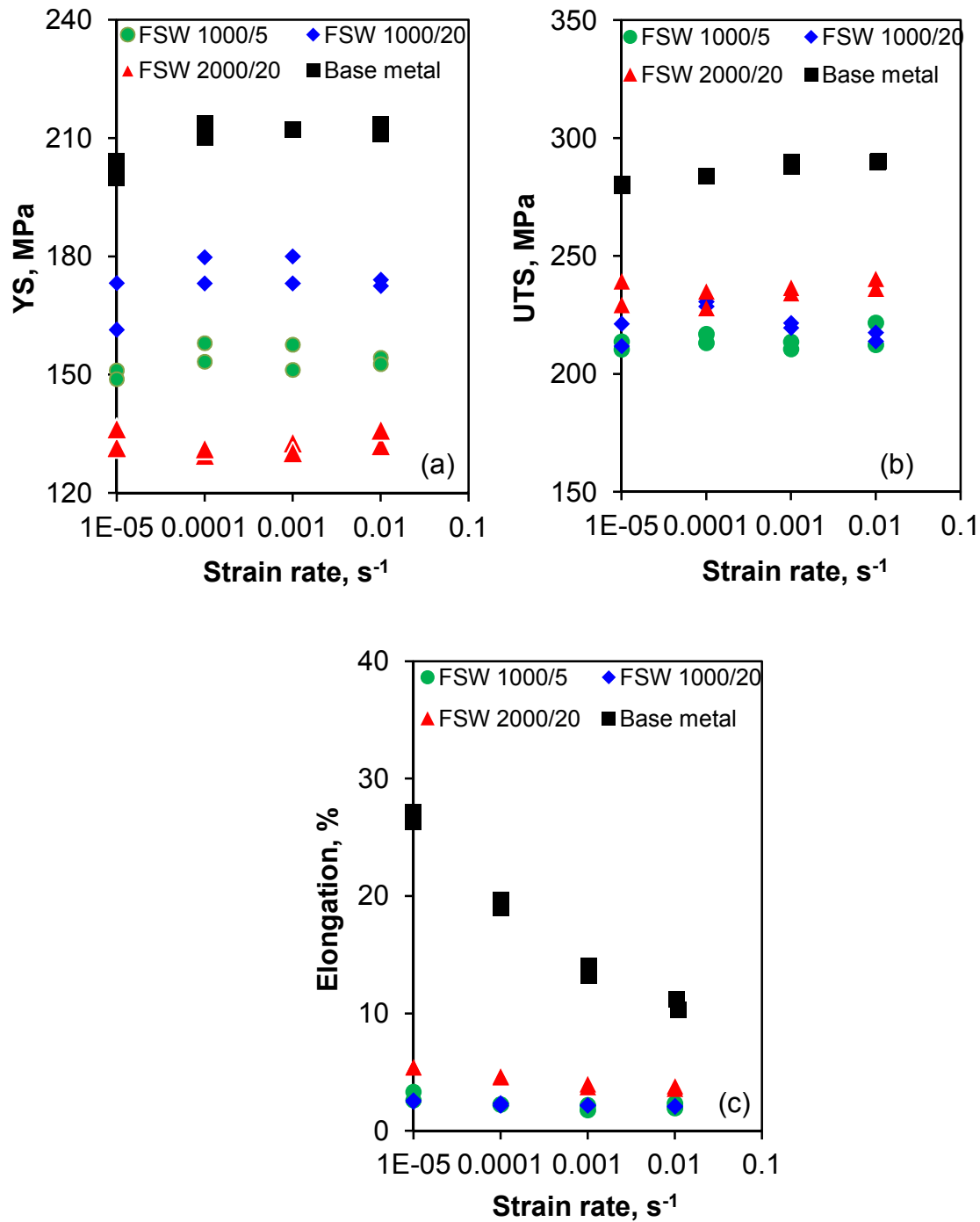
Fig,5.8 Effect of strain rate on (a) yield strength (YS), (b) ultimate tensile strength (UTS), and (c) ductility of the AZ31B-H24 base metal and FSWed joints made with different welding parameters.

Table 5.2 Hardening capacity of the BM and FSWed samples of AZ31B-H24 Mg alloy tested at different strain rates.

	Hardening capacity, H_c			
Strainrate, s^{-1}	Base metal	FSW 1000 rpm, 5 mm/s	FSW 1000 rpm, 20 mm/s	FSW 2000 rpm, 20 mm/s
1×10^{-2}	0.36	0.41	0.24	0.78
1×10^{-3}	0.36	0.38	0.25	0.79
1×10^{-4}	0.34	0.38	0.3	0.75
1×10^{-5}	0.39	0.41	0.29	0.75

Several researchers have proposed different equations to evaluate the strain hardening exponent. Fig. 5.9 shows the evaluated strain hardening exponents (n and n^* as discussed in Chapter 4) as a function of strain rate for the BM and FSWed joints at different welding speeds and rotational rates. Only the tensile test data lying in-between the YS and UTS were used to evaluate the values of n and n^*. It is clear that the strain hardening exponent after FSW became much higher due to the significant changes in both the microstructure (Fig. 5.2(b)-(d) vs. Fig.5.2(a)) and texture in the SZ (Fig.5.4 and Fig.5.5). While a similar trend for both n and n^* values in relation to the welding parameters and strain rates was seen in Fig. 5.9(a) and Fig. 5.9(b), the values of n^* were more than twice larger than those of n due to the exclusion of elastic deformation in the evaluation of n^* values via Equation. (4.6). This suggests that the n^* value was more sensitive in characterizing the strain hardening behavior of materials. While the strain hardening exponent of

the BM was nearly independent of the strain rate (i.e., n=~0.12 and n^*=~0.35), the strain hardening exponent of the FSWed joints at different welding speeds and rotational rates increased slightly with increasing strain rate. The strain hardening exponent increased as the welding speed decreased from 20 mm/s to 5 mm/s while the rotational rate was kept constant at 1000 rpm. On the other hand, the strain hardening exponent increased with increasing rotational rates from 1000 rpm to 2000 rpm while the welding speed remained constant at 20 mm/s. These changes corresponded well to those of the YS, UTS, and ductility shown in Fig. 5.8. The main reason why both high welding speed of 20 mm/s and rotational rate of 2000 rpm gave rise to a significantly higher hardening capacity (Table 5.2) and higher strain hardening exponent (Fig.5.9) was associated with the obviously larger grain size (Fig.5.2(d)), since the larger recrystallized grains had a larger dislocation storage capacity during plastic deformation [58].
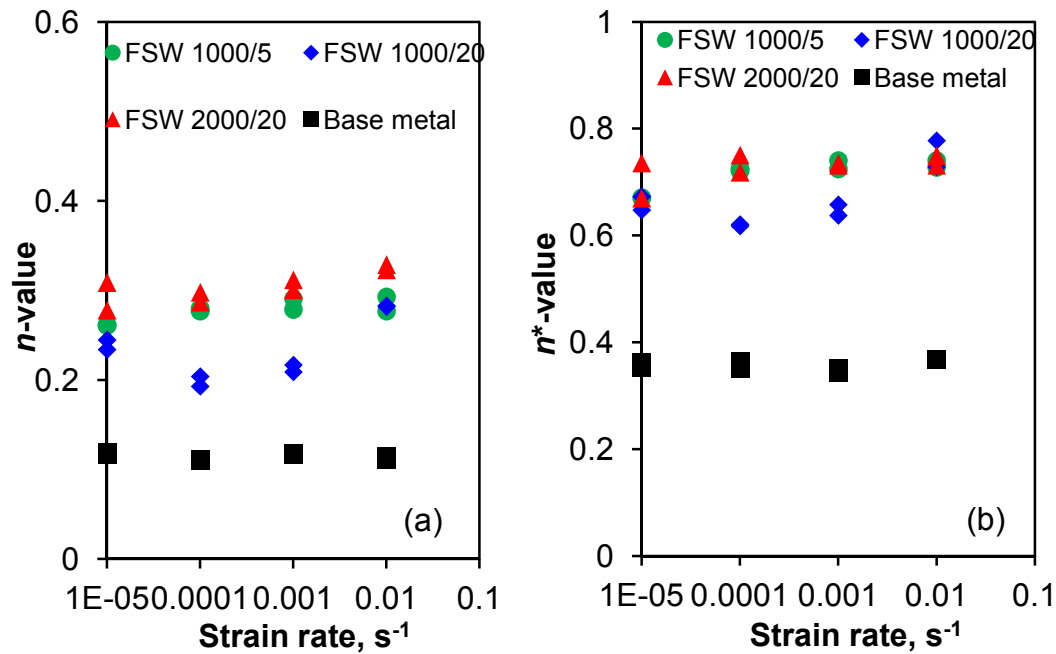
Fig.5.9 Effect of strain rate on the strain hardening exponent of (a) n-value and (b) n*-value of the AZ31B-H24 base metal and FSWed joints made with different welding parameters.

CHAPTER 6

LAP SHEAR STRENGTH AND FATIGUE LIFE OF FRICTION STIR SPOT WELDED AZ31 MAGNESIUM AND 5754 ALUMINUM ALLOYS

6.1 Microstructure

Typical microstructures of the base metal (BM) of AZ31B-H24 Mg alloy and Al 5754-O Al alloy are shown in Fig. 6.1(a) and Fig. 6.1(b), respectively. The cross section of a weld can usually be divided into four regions, i.e., BM, heat-affected zone (HAZ), thermomechanical-affected zone (TMAZ) and stir zone (SZ). The typical microstructures of these regions are shown in Fig. 6.1(a), (c), (d) and (e), respectively for a Mg/Mg similar weld. As shown in Fig. 6.1(a), elongated and pancake-shaped grains with varying sizes were observed in the BM of the Mg alloy due to both the deformation of the 2 mm thick sheet by rolling and incomplete dynamic recrystallization (partial annealing) [52,53,58]. The elongated grains in the BM of the Mg alloy have experienced recrystallization and become equiaxed in the SZ (Fig. 6.1(e)) of the Mg/Mg similar weld. The grains in the HAZ and TMAZ (Fig. 6.1(c) and Fig. 6.1(d)) were partially recrystallized and appeared less uniformly sized, compared with those in the SZ. Condense grain structure was observed in the SZ due to the dynamic recrystallization occurring in the periphery of the pin tool because of the stirring movement and friction thermal cycle [8]. In the SZ, the intense plastic deformation and high temperatures caused dynamic recrystallization, inducing the appearance of fine and homogenous grains, whereas the grains in the HAZ and TMAZ became coarser because of the predominant effect of the friction heating. A similar compact equiaxed grain structure in the SZ and coarse grains in the TMAZ and HAZ for FSS weld of AZ31 alloy

73

was reported by Jordon *et al.* [72], Shen *et al.* [135] and Ding *et al.* [136].A typical optical image at the interface of a dissimilar Al-to-Mg (Al/Mg) weld is shown in Fig. 6.1(e).The interface was marked by the presence of an interfacial layer that covered most of the boundary but varied in thickness. Fig. 6.2(a) shows a SEM image of the interface taken from the cross-section of an Al/Mg dissimilar weld. It is seen that a distinguishable interlayer with a thickness up to ~20 μm occurred in-between the Mg alloy (at the left side in Fig. 6.2(a)) and the Al alloy (at the right side in Fig. 6.2(a)). The EDS line analysis result shown in Fig. 6.2(b) revealed the mutual presence of Al and Mg across the reaction layer, suggesting that an intermetallic (IMC) layer formed at the Al/Mg interface during FSSW. X-ray diffraction patterns obtained from the two matching fracture surfaces, one on the Al alloy side and the other on the Mg alloy side, are shown in Fig. 6.3(a) and Fig. 6.3(b). Besides Mg, Al_3Mg_2 and $Al_{12}Mg_{17}$were observed on the fracture surface of Mg alloy side, while Al and Al_3Mg_2 were identified on the fracture surface of Al alloy side with the absence of $Al_{12}Mg_{17}$. Similar results were also reported by Sato *et al.* [71] for the FSSW of AZ31 to AA5083 alloys. The formation of such intermetallic compounds in the Al/Mg dissimilar welds was due to the constitutive liquation during FSSW [137,138]. Gerlich *et al*. [139] conducted FSSW of AA6111 to AZ91 alloys and reported that the peak temperature in the vicinity of the tool rapidly reached the α-Mg and $Al_{12}Mg_{17}$ eutectic temperature of 437°C, at which the eutectic microstructure formed. According to the Al-Mg phase diagram [140], a wide range of chemical composition that exhibited a low melting temperature in the Al-Mg system could assist in the formation of the inhomogeneous interfacial layer between the Al/Mg dissimilar weld.
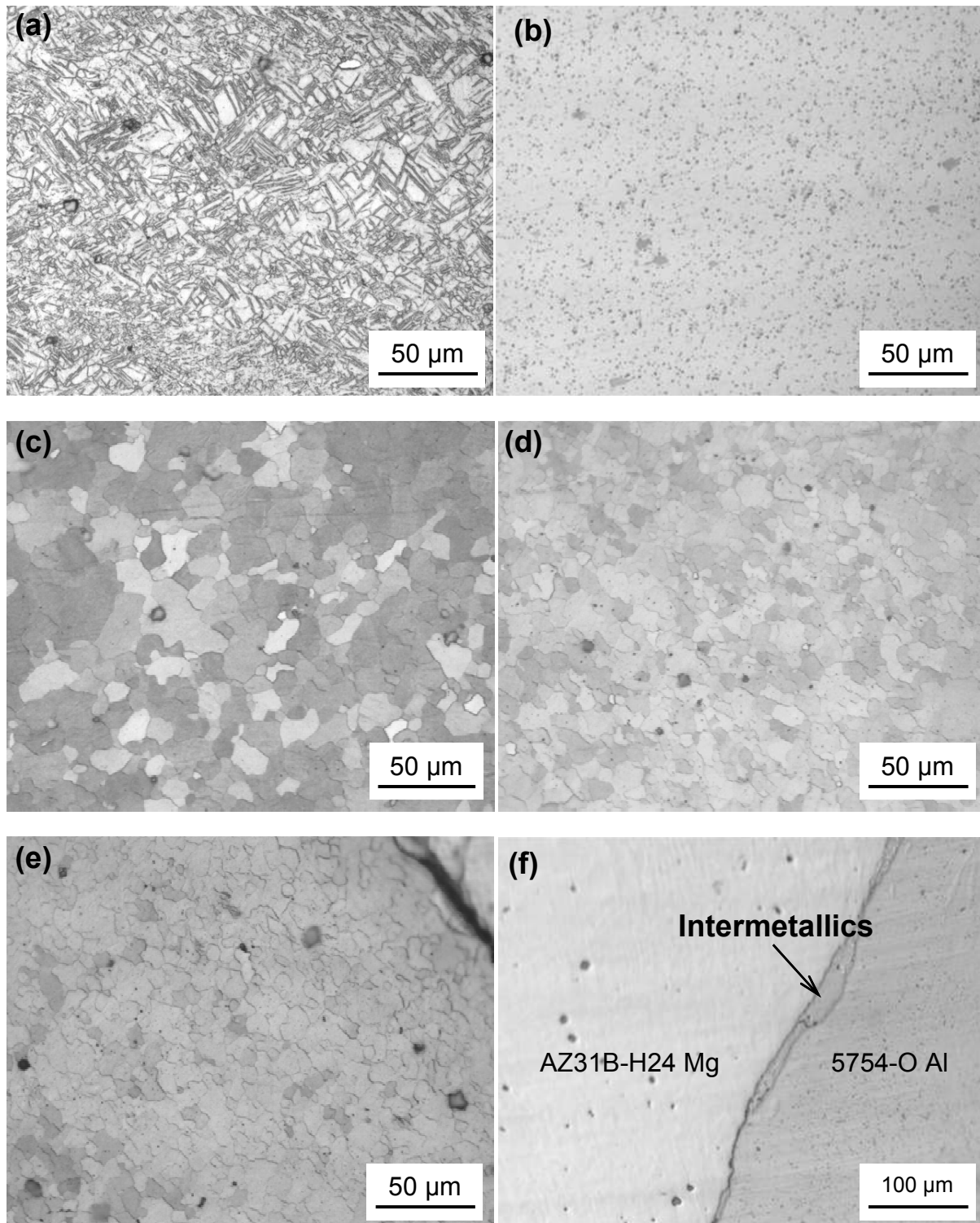
Fig.6.1 Typical microstructures of a friction stir spot welded lap joint (a) AZ31B-H24 Mg base metal, (b) Al 5754-O base metal,(c) heat-affected zone (HAZ) of Mg/Mg weld, (d) thermo-mechanical affected zone (TMAZ) of Mg/Mg weld, (e) stir zone (SZ) of Mg/Mg weld which was taken just below the bottom of keyhole, and (f) presence of intermetallics in the Al/Mg dissimilar weld in the stir zone (SZ).
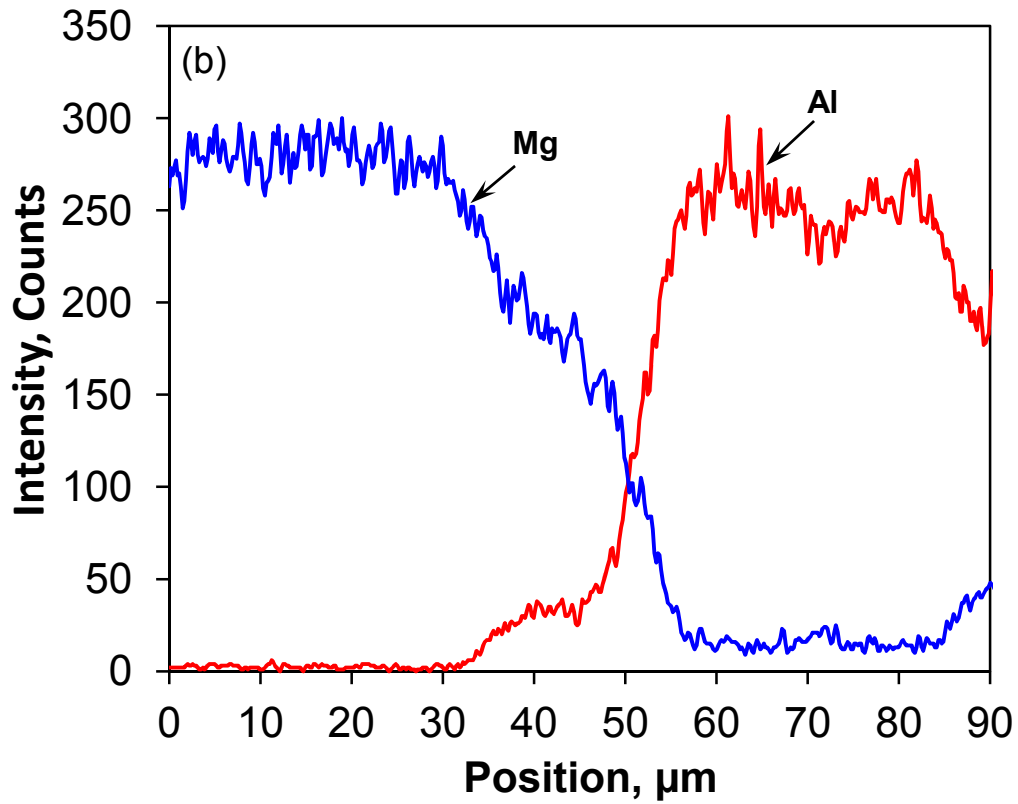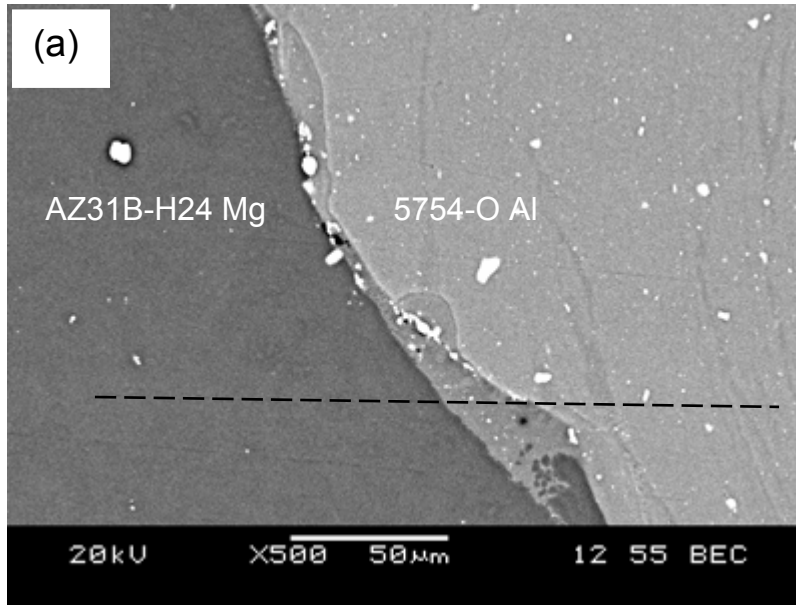
Fig.6.2 (a) SEM micrograph showing an interlayer present between the Al/Mg dissimilar FSS weld, and (b) EDS line scan across the interlayer indicated in (a) showing the Al and Mg compositional variations.
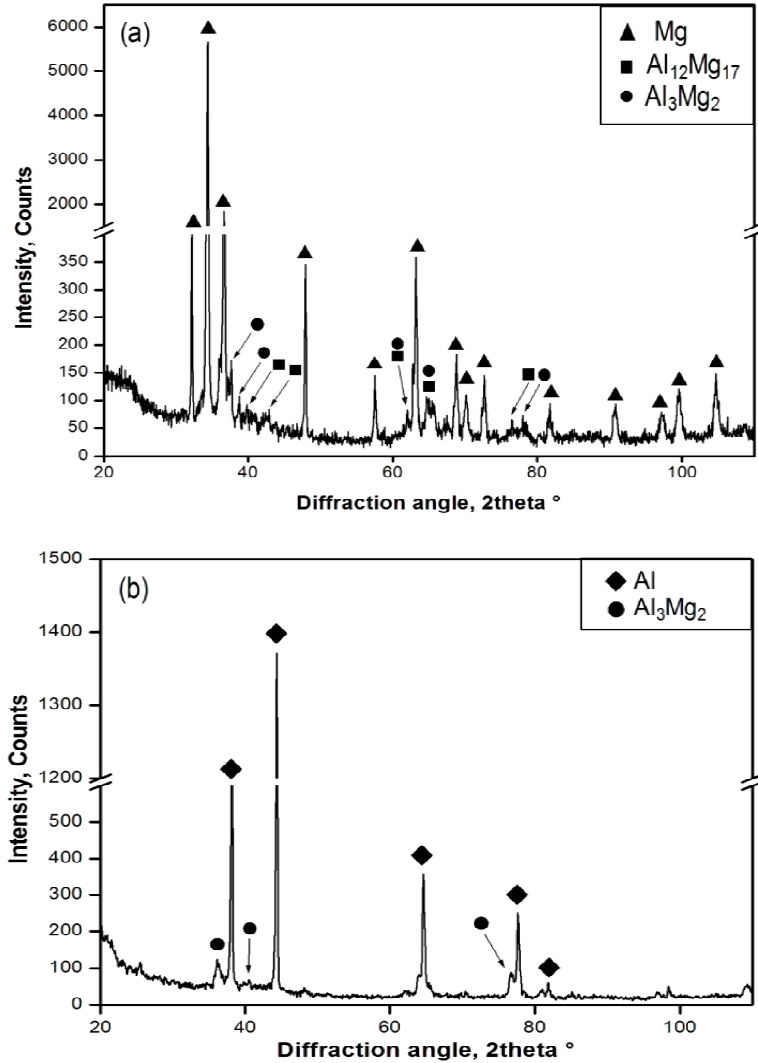
Fig.6.3 X-ray diffraction patterns obtained from the matching fracture surfaces of the Al/Mg dissimilar FSS weld, (a) Mg side, and (b) Al side.

In addition, some particles were also seen in the SZ of the Al/Mg dissimilar weld (Fig. 6.4(a)). EDS analysis revealed that these particles were unmelted Mn- and Al-containing (~67 at.% Al and ~33 at.% Mn) intermetalics (Fig. 6.4(a) and Fig. 6.4(b)). Similar results were also reported by Xiao *et al.* [36,38] for resistance spot welding of a Mg alloy, where they observed that many unmelted Mn-Al (Al_8Mn_5) second-phase particles resulted in effective nucleation sites, giving rise to a fine grain size in the fusion zone of the resistance spot weld.
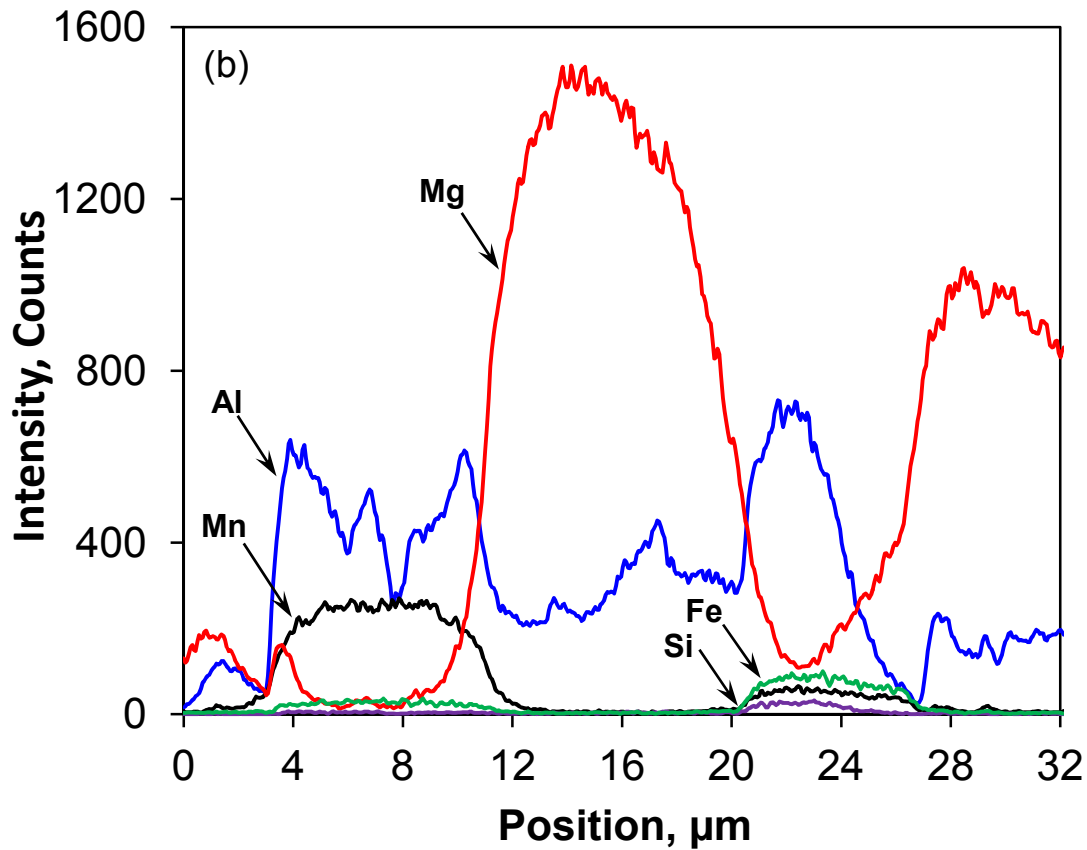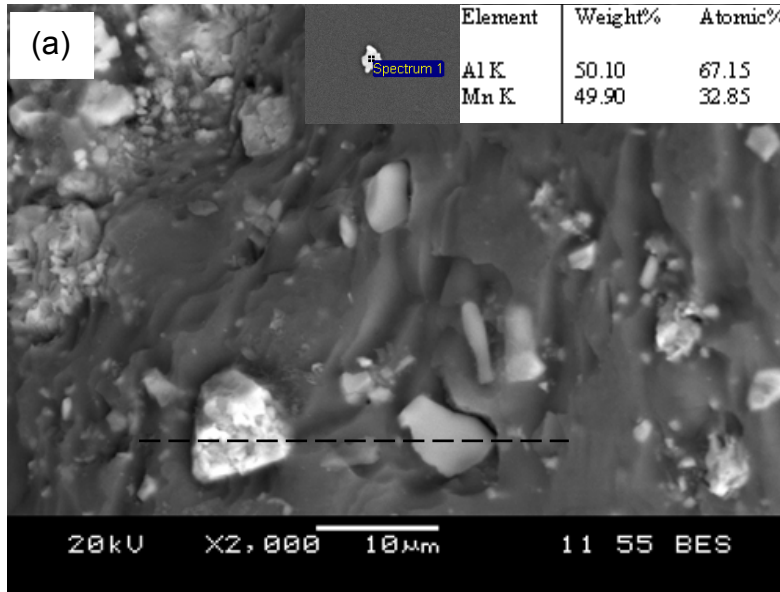
Fig.6.4 (a) SEM micrograph showing Al-Mn particles on the fracture surface of the Al/Mg dissimilar FSS weld along with a EDS point analysis showing the atom percent of Al and Mn in a particle, (b) EDS line scan across the two particles in (a) showing Al and Mn compositional variations across the particles.

6.2 Microhardness

The hardness distribution across the Al/Al and Mg/Mg similar welds obtained from the upper and lower sheets is shown in Figs 6.5 and 6.6, respectively. Compared to the hardness of the base metal of Al and Mg alloys, the hardness was lower in a region approximately 7-10 mm in diameter centered in the welded region. There was only a small difference in hardness between the upper and lower sheets, with the minimum hardness appearing below the shoulder and the hardness increasing progressively closer to the keyhole periphery. As shown in Fig. 6.6, the hardness distribution of the Mg/Mg similar weld was observed to be nearly symmetric with respect to the center of the keyhole, showing a W-shaped appearance. The hardness in the HAZ and TMAZ was lower than that of the base Mg alloy, and reached a minimum value of ~52 HV in the TMAZ which was equivalent to ~70% of the base metal hardness. The hardness in the SZ located just below the pin bottom (just beneath the bottom of the keyhole) was indeed higher than that in the TMAZ and HAZ of Mg/Mg weld, as seen in Fig. 6.6. Such a hardness change in each zone of the weld corresponded well to the variation in the grain sizes of the HAZ, TMAZ, and SZ (i.e., Fig. 6.1(c) → 6.1(e)). According to the Hall-Petch relationship in the welded AZ31B-H24 Mg alloy [52,53,58], the finer grain structure would result in a higher value of hardness in the SZ as compared to the TMAZ and HAZ. Since the grain boundaries were the main obstacle to the slip of dislocations, the material with a smaller grain size would have a stronger resistance to the localized plastic deformation due to the presence of more grain boundaries, giving rise to a higher hardness or strength. As shown in Fig. 6.7, the SZ below the bottom of keyhole in the Al/Mg dissimilar weld had much higher hardness values lying in-between 120 and 150 HV. This higher hardness was predominantly due to the presence of hard and brittle IMCs (Al_3Mg_2 and $Al_{12}Mg_{17}$ phases), as identified by XRD (Fig. 6.3). Similar results

were also reported by other researchers [71,137,138,142-144]. Therefore, the microhardness test results provided a further corroboration for the occurrence of hard IMCs in the Al/Mg dissimilar weld, which could become an easy fracture path as presented in the later sections.
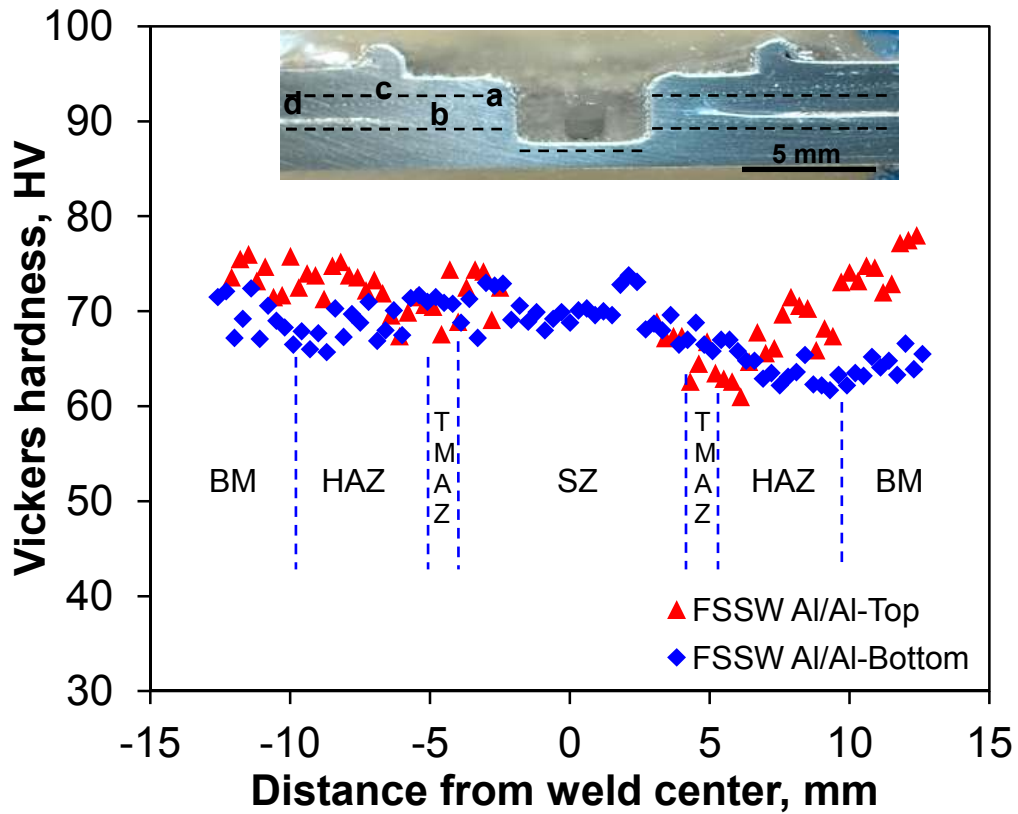
Fig.6.5 Typical microhardness profile across an Al/Al similar FSS weld along the top and bottom sheets, where (a) stir zone (SZ), (b) thermo-mechanical affected zone (TMAZ), (c) heat-affected zone (HAZ), and (d) base metal (BM) are indicated.
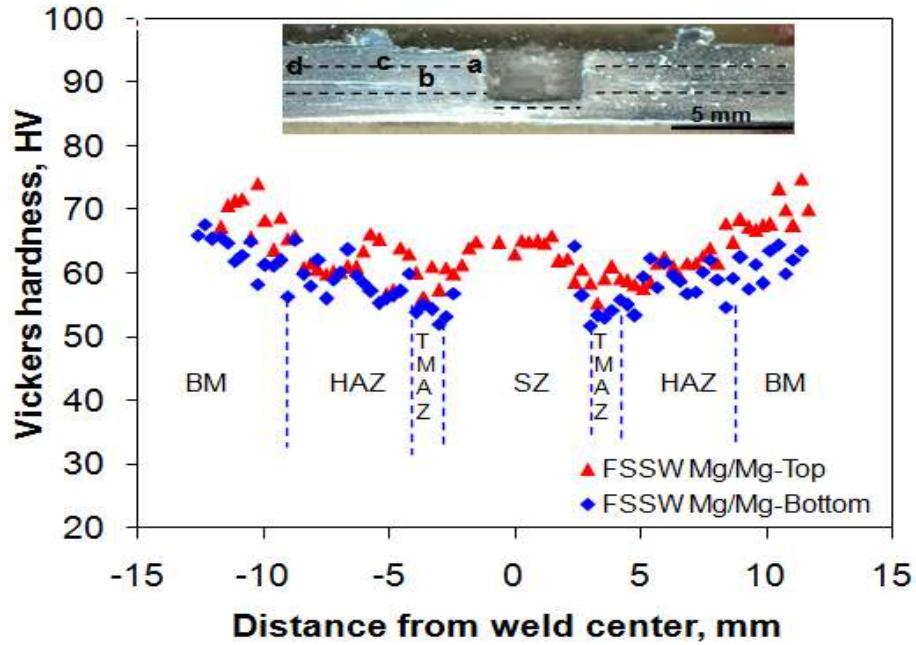
Fig.6.6 Typical microhardness profile across a Mg/Mg similar FSS weld along the top and bottom sheets, where (a) stir zone (SZ), (b) thermo-mechanical affected zone (TMAZ), (c) heat-affected zone (HAZ), and (d) base metal (BM) are indicated.
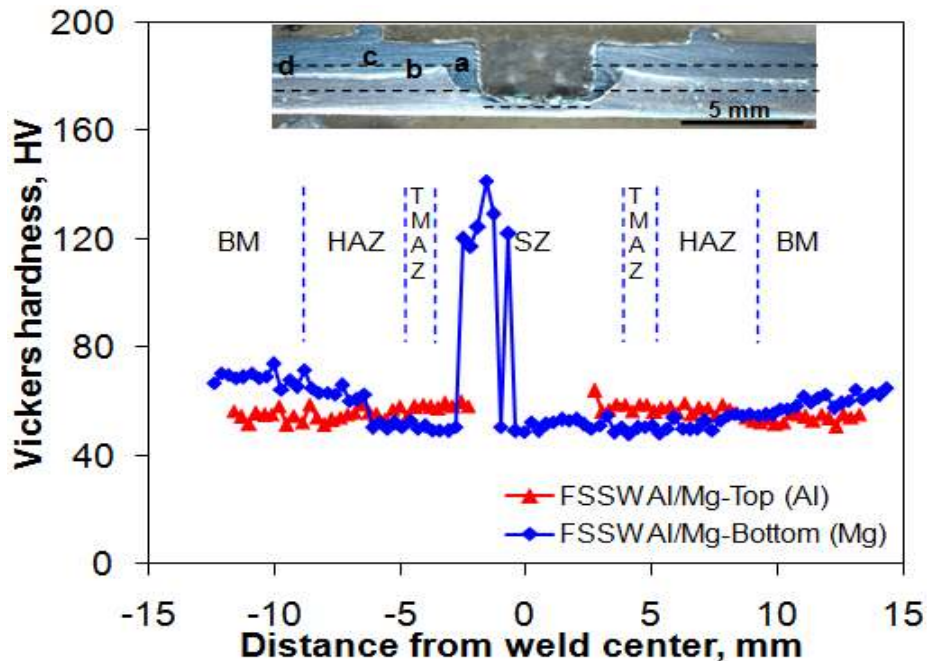
Fig.6.7 Typical microhardness profile across an Al/Mg dissimilar FSS weld along the top and bottom sheets, where (a) stir zone (SZ), (b) thermo-mechanical affected zone (TMAZ), (c) heat-affected zone (HAZ), and (d) base metal (BM) are indicated.

81

6.3 Lap shear strength

Typical load vs. displacement curves of the Al/Al and Mg/Mg similar welds, and Al/Mg dissimilar welds tested at a crosshead speed of 10 mm/min are shown in Fig. 6.8(a). It is clear that both the Mg/Mg and Al/Al similar welds were much stronger than the Al/Mg dissimilar weld, and the Mg/Mg similar weld was further stronger than the Al/Al similar weld. However, the Al/Al similar weld could endure longer. The evaluated maximum lap shear load is shown in Fig. 6.8(b). It is clear that the maximum lap shear load of the Mg/Mg similar weld was higher than that of the Al/Al similar weld, which was further higher than that of the Al/Mg dissimilar weld. The considerably lower maximum lap shear load in the Al/Mg dissimilar weld was obviously attributed to the formation of a brittle IMC layer (Figs 6.2, 6.3 and 6.7). A similar observation on the maximum lap shear load was also reported by Miller *et al*. [145] for FSS weld 1.5-mm thick Al 6111-T4 alloy sheets reinforced with ancorsteel particles, where they reported that the maximum lap shear load increased by 25% for the steel particle reinforced metal matrix composites (MMC) as compared to that of the base metal. To characterize more completely the lap shear characteristics of the welds, the failure energy was estimated, where the failure energy was defined as the area below the load-displacement curve shown in Fig. 6.8(a). When the tensile lap shear remained continuous after reaching the maximum load without failure (i.e., in the case of Al/Al similar weld in the present study), the failure energy was only calculated corresponding to the maximum load in a more conservative manner. The evaluated results are plotted in Fig. 6.8(c). While the failure energy of the Al/Al similar weld was greater than that of the Mg/Mg similar weld, the failure energy of the Mg/Mg and Al/Al similar welds was substantially higher than that of the Al/Mg dissimilar weld. There exists a direct correlation between the failure energy in the lap shear tensile tests and impact tests. This implies that the

Al/Al similar weld would have a higher impact resistance than that of the Mg/Mg similar weld. Furthermore, nugget pullout failure was observed for the Mg/Mg and Al/Al similar welds while nugget debonding failure was observed for the Al/Mg dissimilar weld during lap shear tensile tests (Fig. 6.8(a)).
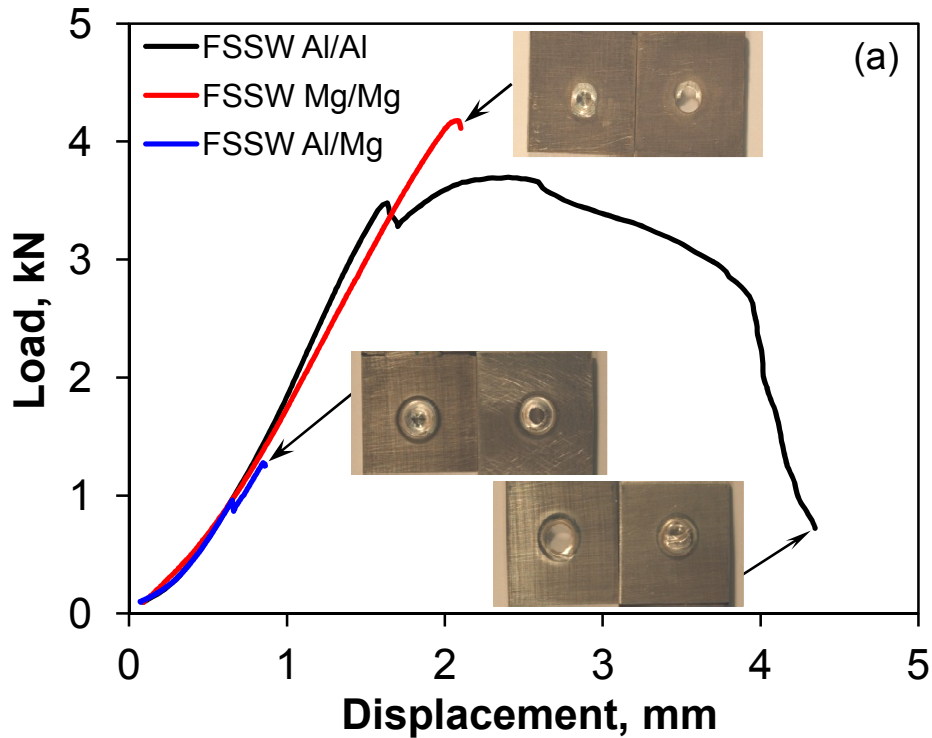
Fig.6.8 Lap shear properties of the Al/Al and Mg/Mg similar FSS welds, and Al/Mg dissimilar FSS welds tested at a crosshead speed of 10 mm/min.(a) load vs. displacement curve, (b) maximum lap shear load, and (c) failure energy mapping. (continued)
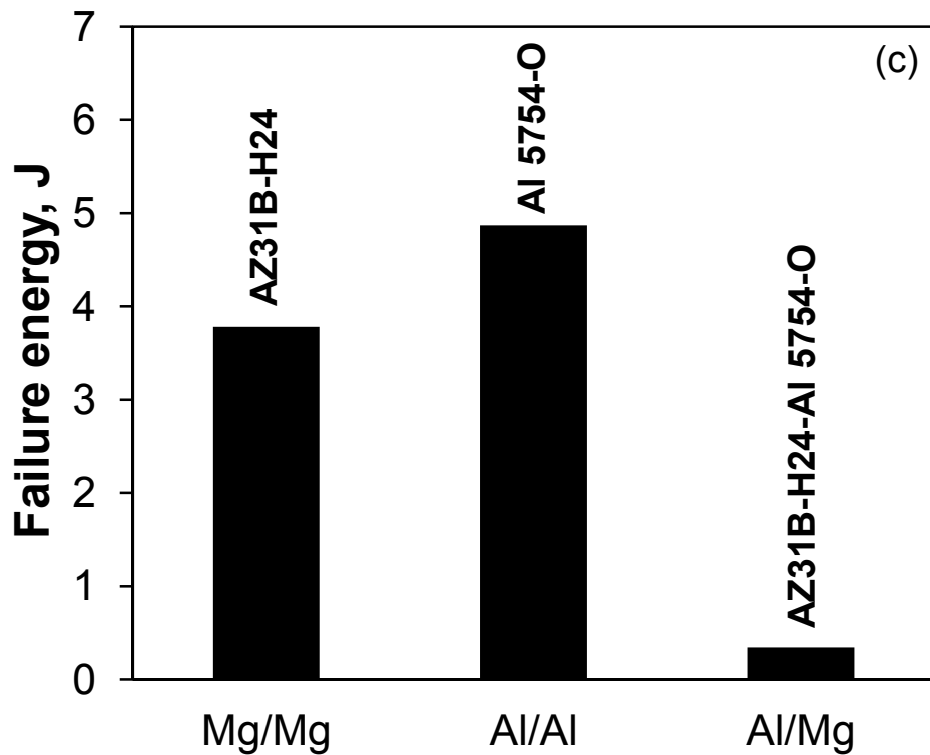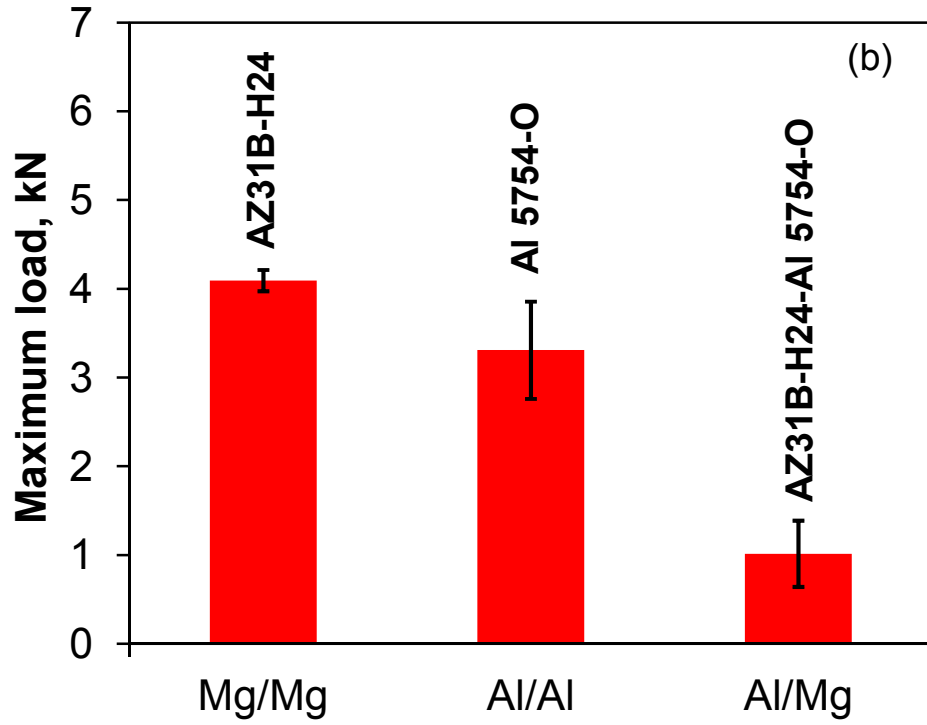
Fig.6.8 Lap shear properties of the Al/Al and Mg/Mg similar FSS welds, and Al/Mg dissimilar FSS welds tested at a crosshead speed of 10 mm/min.(a) load vs. displacement curve, (b) maximum lap shear load, and (c) failure energy mapping.

6.4 Fatigue behavior and failure mode

Fatigue test results of the Mg/Mg and Al/Al similar welds, and Al/Mg dissimilar welds obtained at RT, R=0.2, and 50 Hz are plotted in Fig. 6.9. Like the failure energy (Fig. 6.8(c)), the fatigue life of the 5754-O Al/Al similar welds was in general longer than that of the AZ31B-H24 Mg/Mg similar welds in spite of the presence of a relatively large experimental scatter. A longer fatigue life for the Al 5754-O similar weld was reported in comparison with that of the Al 6111-T4 similar weld under the same cyclic loading condition (R=0.2, f =10 Hz) [18]. The fatigue life of the Al/Mg dissimilar welds was much lower and more scattered than that of both the Al/Al and Mg/Mg similar welds especially at the maximum cyclic load higher than 1 kN. Again, this was due to the formation of IMCs at the interface between the Mg and Al alloys during FSSW (Figs 6.2, 6.3, and 6.7). The weld nugget was pulled out of the top sheet of the Mg/Mg and Al/Al similar welds at the maximum cyclic load of 4 kN, as shown by the inserted images in Fig. 6.9. The nugget pullout failure occurred as the crack propagated circumferentially around the nugget. The shear stress in the remaining area of the nugget increased with each advancement of the crack front. After the crack had propagated around half of the nugget with a keyhole the shear stresses acting in the area were such that the remaining cross section could not sustain the shear overload, then the nugget pullout failure occurred. In contrast, the failure of the Al/Al and Mg/Mg similar welds occurred nearly at a right angle to the loading direction at the maximum cyclic load below 1.5 kN (Fig. 6.9). This suggests that the fatigue failure was caused by the opening of the keyhole through crack initiation in the TMAZ and HAZ, due to the significant microstructural change or grain coarsening (Fig. 6.1(c) and Fig. 6.1(d)) and the lower hardness (Fig. 6.5 and Fig. 6.6), and then propagated perpendicular to the loading direction that indeed resulted in normal tensile failure mode. Nugget debonding failure mode was observed in the

Al/Mg dissimilar welds as a consequence of the presence of an interfacial IMC layer in the Al/Mg dissimilar welds (Figs 6.2, 6.3, and 6.7).
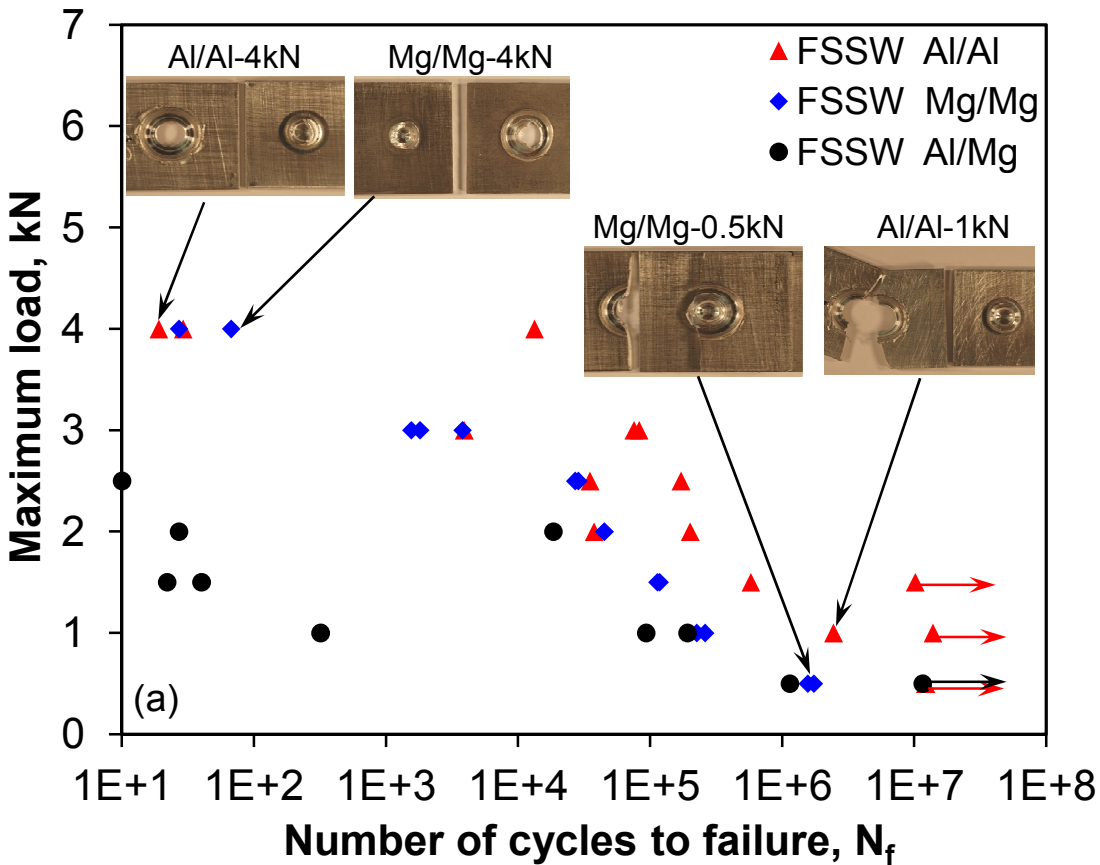
Fig. 6.9 S-N curves of the Al/Al and Mg/Mg similar FSS welds, and Al/Mg dissimilar FSS welds tested at R=0.2, 50 Hz and room temperature. (a) Maximum load vs. the number of cycles to failure (N_f) in the semi-log scale for all three types of welded joints.

Fig. 6.9(b) and Fig. 6.9(c) could be used to characterize better the fatigue data and failure mode obtained in the present study where the maximum cyclic load vs. the number of reversals to failure ($2N_f$) was plotted in a double-log scale for the Mg/Mg and Al/Al similar welds. It should be noted that the run-out data for which no failure occurred at or over 1×10^7 cycles were not included in the fitting. As shown in Fig. 6.9(b) and Fig. 6.9(c) for the Mg/Mg and Al/Al similar welds, a longer fatigue life was observed at the lower maximum load, where the slope was

steeper corresponding to the normal tensile failure mode, than that at the higher maximum load where the slope was flatter in line with the failure mode of nugget pullout.
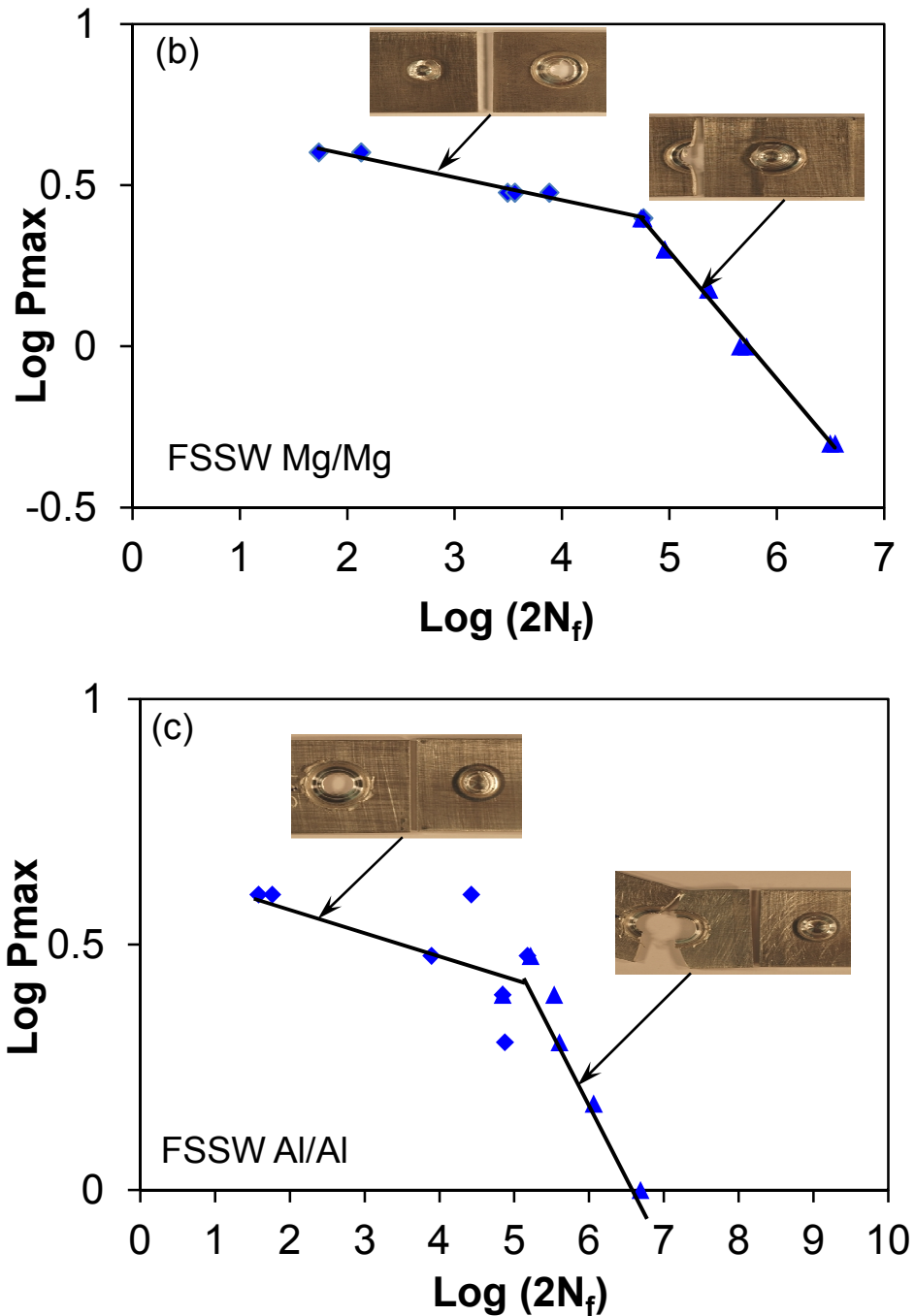
Fig.6.9 S-N curves of the Al/Al and Mg/Mg similar FSS welds, and Al/Mg dissimilar FSS welds tested at R=0.2, 50 Hz and room temperature. (b) Maximum load vs. the number of reversals to failure ($2N_f$) in the double-log scale for the Mg/Mg similar FSS welds (c) Maximum load vs. the number of reversals to failure ($2N_f$) in the double-log scale for the Al/Al similar FSS welds.

6.5 Fractography

Figs 6.10 and 6.11 show SEM images of the fatigue fracture surfaces of the Mg/Mg and Al/Al similar welds and the load dependence of failure mode. At a lower level of maximum cyclic loads, as shown in Fig 6.10(a)-(c) and Fig. 6.11(a)-(c), fatigue cracking was caused by the opening of the keyhole through the TMAZ and HAZ and then propagated at right angles to the loading direction. Fatigue crack propagation was mainly characterized by the formation of fatigue striations (Fig. 6.10(c) and Fig. 6.11(c)) in conjunction with secondary cracks, which appeared usually perpendicular to the fatigue crack propagation direction. Fatigue striations normally occurred by a repeated plastic blunting-sharpening process in the face-centered cubic materials, stemming from the glide of dislocations on the slip plane along the slip direction within the plastic zone ahead of a fatigue crack tip [110]. The formation of fatigue striations in the magnesium alloys with a hexagonal close-packed crystal structure was expected to be additionally associated with the occurrence of twinning-detwinning process [11,64,111,112,146,147], since the number of slip systems in magnesium alloys is limited at room temperature. On the other hand, at the higher maximum cyclic load as shown in Fig 6.10(d)-(e) and Fig. 6.11(d)-(e), a fatigue crack initiated in region A, propagated towards region B along circumferential direction and finally fractured in the mode of nugget pullout in region C located in the SZ. The ridge in region A had roots in the upward material flow of the lower sheet [148], but it should be noted that only a small amount of the lower sheet material underneath the hook flowed upward into the upper sheet. A lot of elongated dimples, e.g., as seen in Fig 6.10(e) for region B, indicated the occurrence of shear fracture prior to the nugget pullout during fatigue tests at the higher maximum cyclic load.
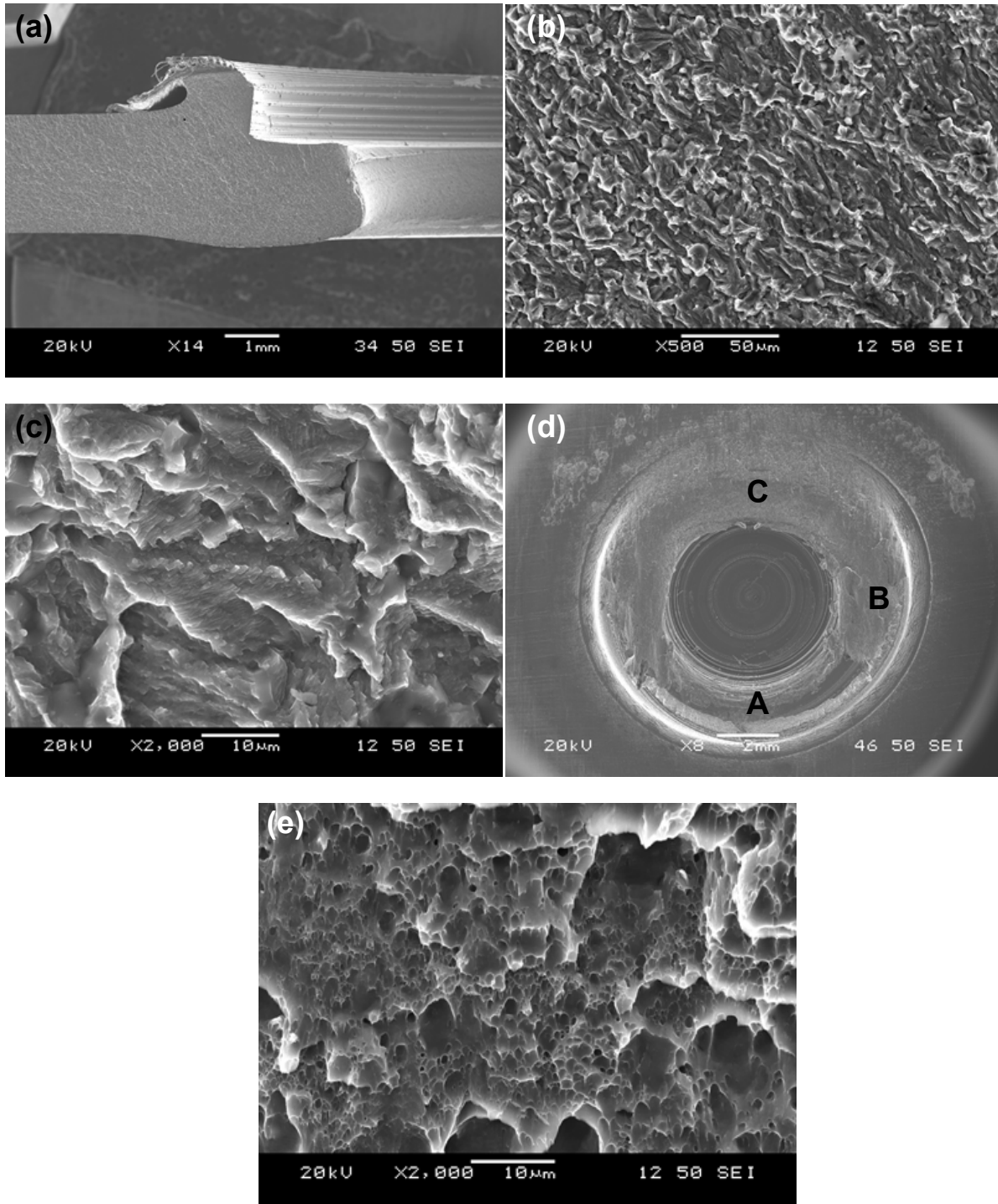
Fig.6.10 Typical SEM images of fatigue fracture surface of the Al/Al similar FSS weld, (a) normal tensile fracture surface at a lower P_{max}=1 kN, (b) crack propagation zone at a lower P_{max}=1 kN, (c) fatigue striations in the crack propagation zone at a higher magnification, (d) overall view of shear fracture surface at a higher P_{max}=4 kN, and (e) shear fracture of region B in (d) at a higher magnification.
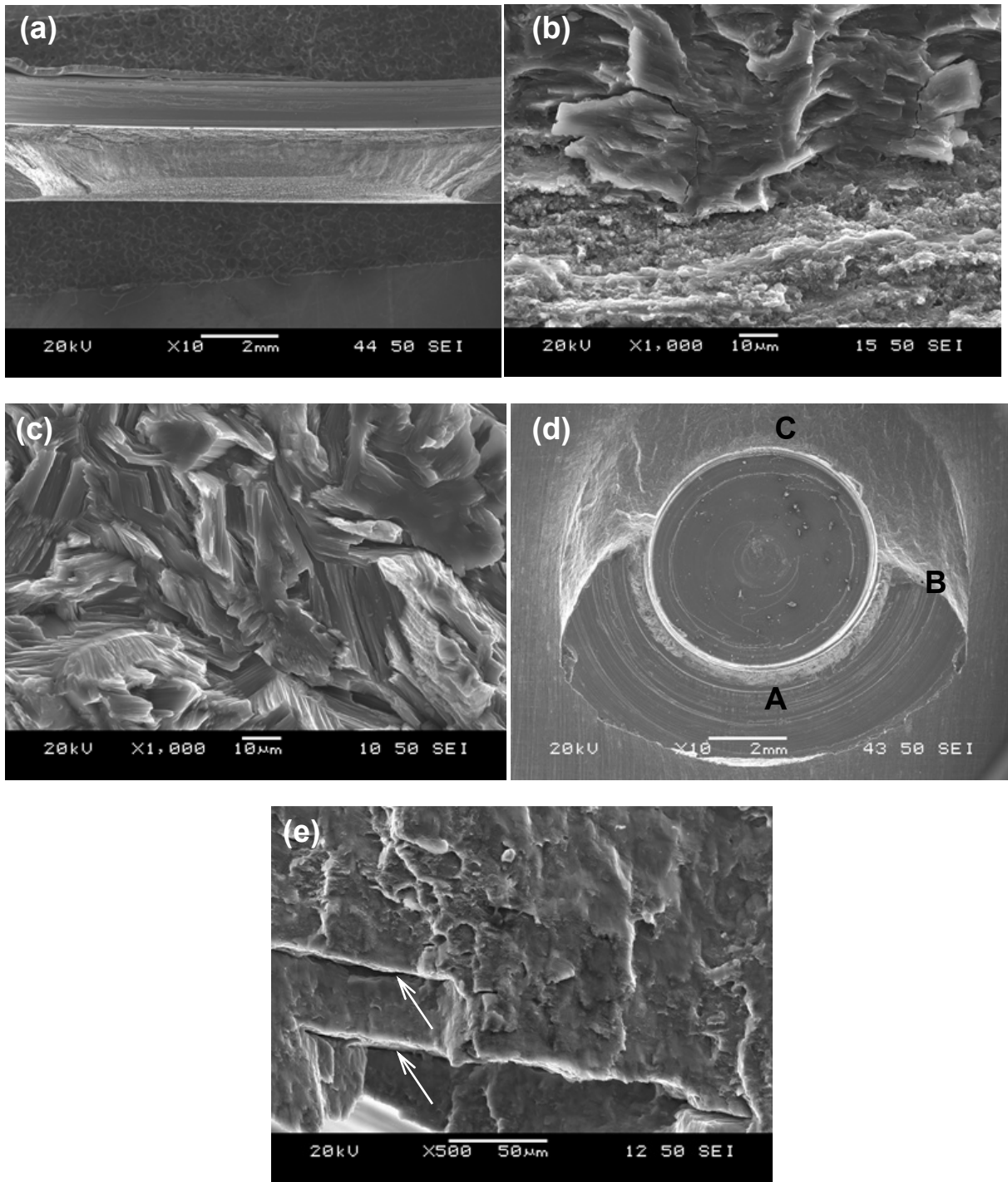
Fig.6.11 Typical SEM images of fatigue fracture surface of the Mg/Mg similar FSS weld, (a) normal tensile fracture surface at a lower P_{max}=0.5 kN, (b) crack propagation zone at a lower P_{max}=0.5 kN, (c) fatigue striation s in the crack propagation zone at a higher magnification, (d) overall view of shear fracture surface at a higher P_{max}=2.5 kN, and (e) secondary cracks at a higher magnification as indicated by an arrows during shear button pullout fracture.

Fig. 6.12 shows SEM images of the fatigue fracture surface of the Al/Mg dissimilar weld. For the dissimilar weld, nugget debonding fracture was observed, as seen in Fig 6.12(a) and Fig. 6.12(b), showing that the faying surface between the upper and lower sheets was torn off, and leaving a relatively smooth fracture surface. At all cyclic load levels, nugget debonding first took place near the keyhole and then the crack propagated towards the circumferential side, causing the whole nugget in the circumferential side to pull-out from the lower sheet. This was mainly attributed to the presence of IMC layers of Al_3Mg_2 and $Al_{12}Mg_{17}$ phases, as observed via SEM/EDS (Fig. 6.2) and identified via XRD (Fig. 6.3), along with the additional Al-Mn particles as shown in Fig. 6.12(c) and Fig. 6.12(d), which thus considerably decreased the fatigue life of the Al/Mg dissimilar weld. The fatigue striations were also observed at the Mg side of fracture surface at the lower maximum cyclic load (Fig. 6.12(f)).
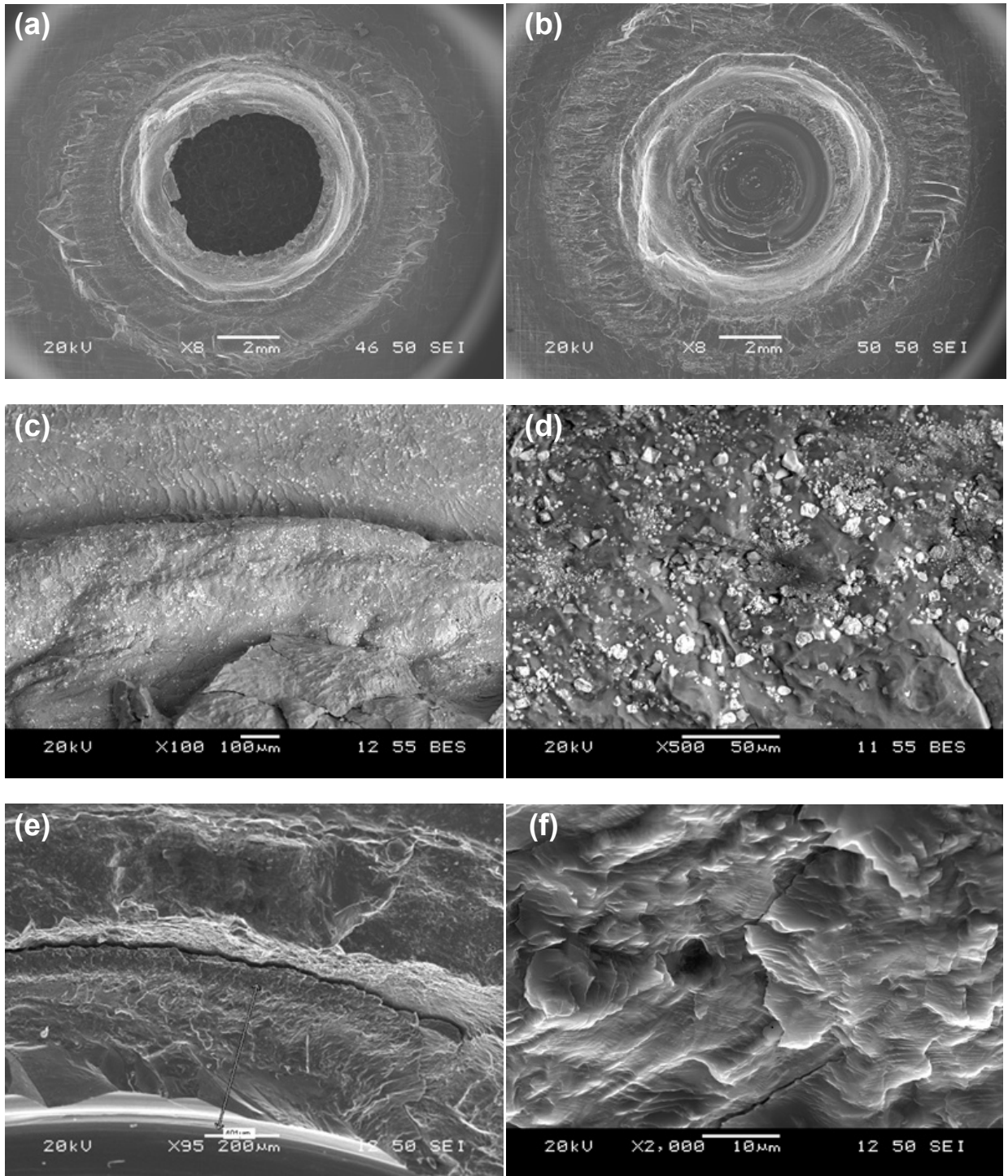
Fig.6.12 Typical SEM images of fatigue fracture surface of the Al/Mg dissimilar FSS weld, (a) nugget debonding fracture surface of Al side, (b) nugget debonding fracture surface of Mg side, (c) Al-Mn particle at Al side, (d) Al-Mn particle at Mg side, (e) Al-Mn particle location at fracture surface of Mg side, and (f) fatigue striations on the fracture surface of Mg side at a lower P_{max}.

CHAPTER 7

LAP SHEAR STRENGTH AND FATIGUE BEHAVIOR OF FRICTION STIR SPOT WELDED DISSIMILAR AZ31 MAGNESIUM/AA5754-O ALUMINUM ALLOY WITH ADHESIVE

7.1 Microstructure

Typical base metal (BM) microstructures for the AZ31B-H24 Mg alloy and the AA5754-O Al alloy are shown in Fig. 7.1(a) and Fig. 7.1(b), respectively. As shown in Fig. 7.1(a), elongated and pancake-shaped grains with varying sizes were observed in the BM of the Mg alloy due to both the deformation of the 2 mm thick sheet by rolling and incomplete dynamic recrystallization (partial annealing) [52,53,58].

Typical optical images at the interface of the dissimilar Al/Mg and Mg/Al adhesive welds are shown in Fig. 7.1(c) and Fig. 7.1(d), respectively. For the Al/Mg weld, the interface was marked by the presence of an interfacial layer which covered most of the boundary of the interface but the thickness of the interfacial layer varied. However, it was different for Mg/Al adhesive weld where the interface was marked by both the adhesive and interfacial layer. Fig. 7.2(a) shows a SEM image of the interface taken from the cross-section of an Al/Mg weld. A distinguishable interlayer with a thickness up to ~20 µm was observed at the interface between the Mg (at the left side in Fig. 7.2(a)) and the Al (at the right side in Fig. 7.2(a)) alloys. The EDS line analysis revealed the mutual presence of Al and Mg across the reaction layer, suggesting that the intermetallic (IMC) layer formed at the Al/Mg interface during FSSW. As shown by the

corresponding EDS line analysis of the image in Fig. 7.2(b), the presence of the adhesive in the

Mg/Al adhesive weld interface decreased the thickness of the IMC layer.
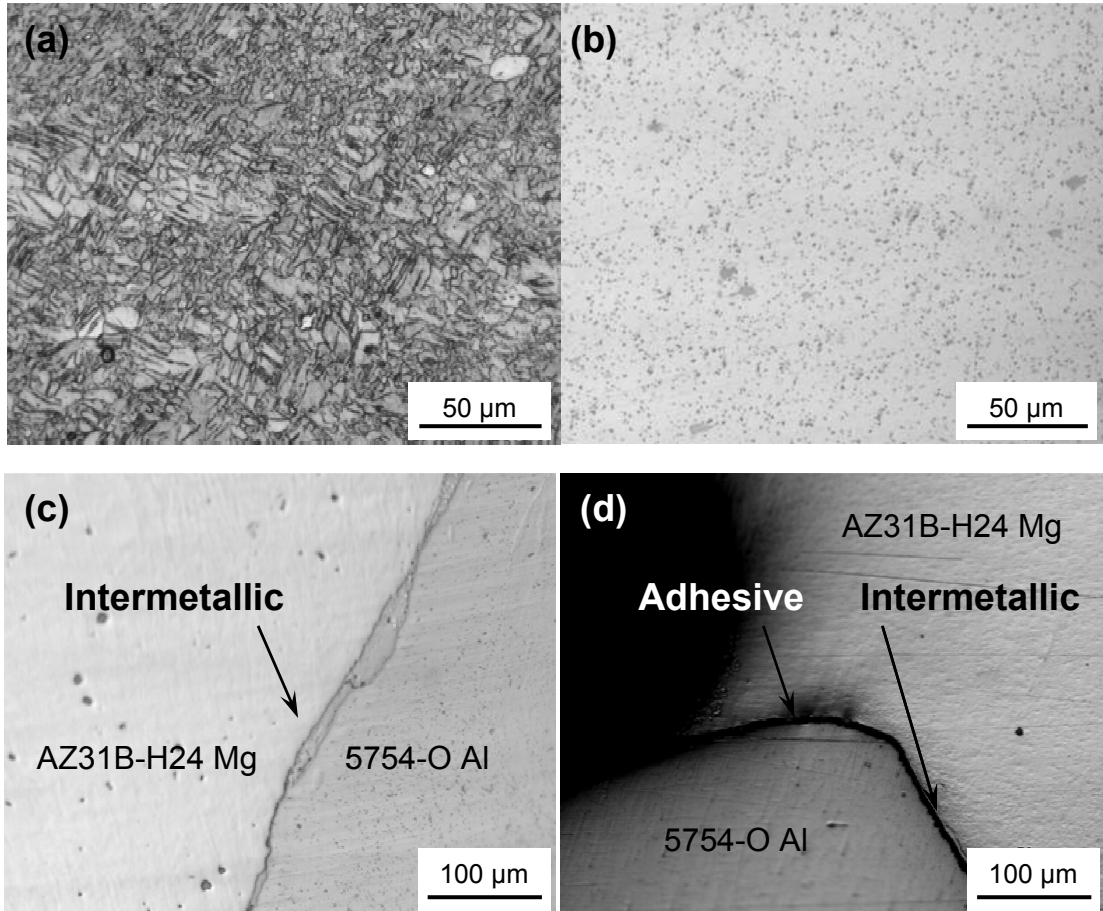
Fig.7.1 Typical microstructures of a FSS weld of AZ31B-H24 Mg alloy to AA5754-O Al alloy; (a) base metal of AZ31B-H24 Mg alloy, (b) base metal of AA5754-O Al alloy, (c) presence of intermettalic at the interface of a dissimilar Al/Mg weld, and (d) presence of intermettalic at the interface of a dissimilar Mg/Al adhesive weld.
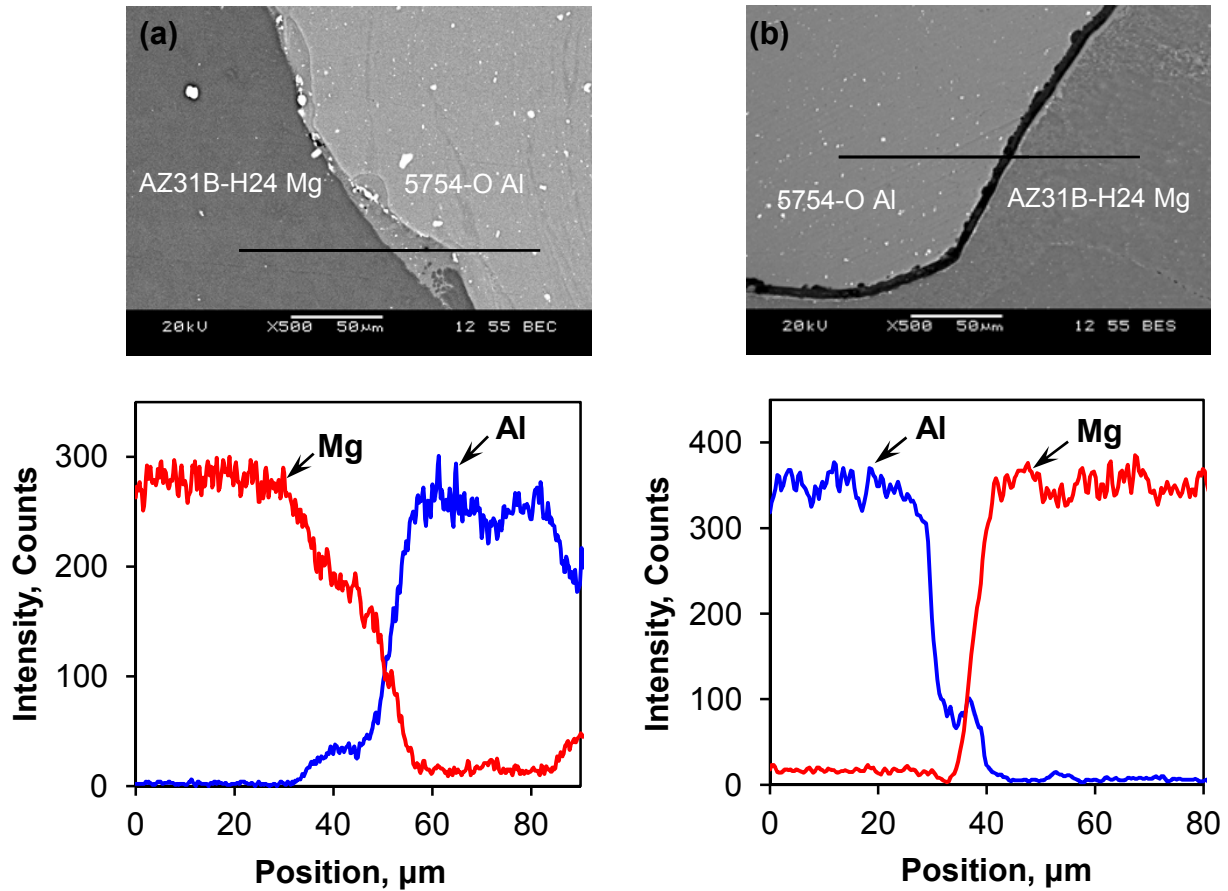
Fig.7.2 SEM micrographs of the Al-Mg phase at the interfaces of dissimilar (a) Al/Mg weld, (b) Mg/Al adhesive weld and the corresponding EDS line scans across the interface showing the compositional variations of Al and Mg.

An X-ray diffraction pattern obtained from the fracture surface of the Mg/Al adhesive weld (Mg alloy side) is shown in Fig. 7.3. Besides Mg, Al_3Mg_2 and $Al_{12}Mg_{17}$ were observed on the fracture surface of the Mg alloy side. Similar results were also reported by Sato *et al.* [71] and Choi *et al.* [141] for FSSW of AZ31 to AA5083 and AA6K21 alloys. The formation of those intermetallic compounds in the Al/Mg dissimilar welds was due to the constitutive liquation during FSSW [71,141]. Gerlich *et al.* [139] conducted FSSW of AA6111 to AZ91 alloys and reported that the peak temperature in the vicinity of the tool rapidly reached the α-Mg and $Al_{12}Mg_{17}$ eutectic

temperature of 437°C, at which the eutectic microstructure formed. According to the Al-Mg phase diagram [140], a wide range in the chemical composition exhibited a low melting temperature in the Al-Mg system which most likely assists in the formation of the inhomogeneous interfacial layer in the SZ of the Al/Mg as well as the Al/Mg and Mg/Al adhesive welds.
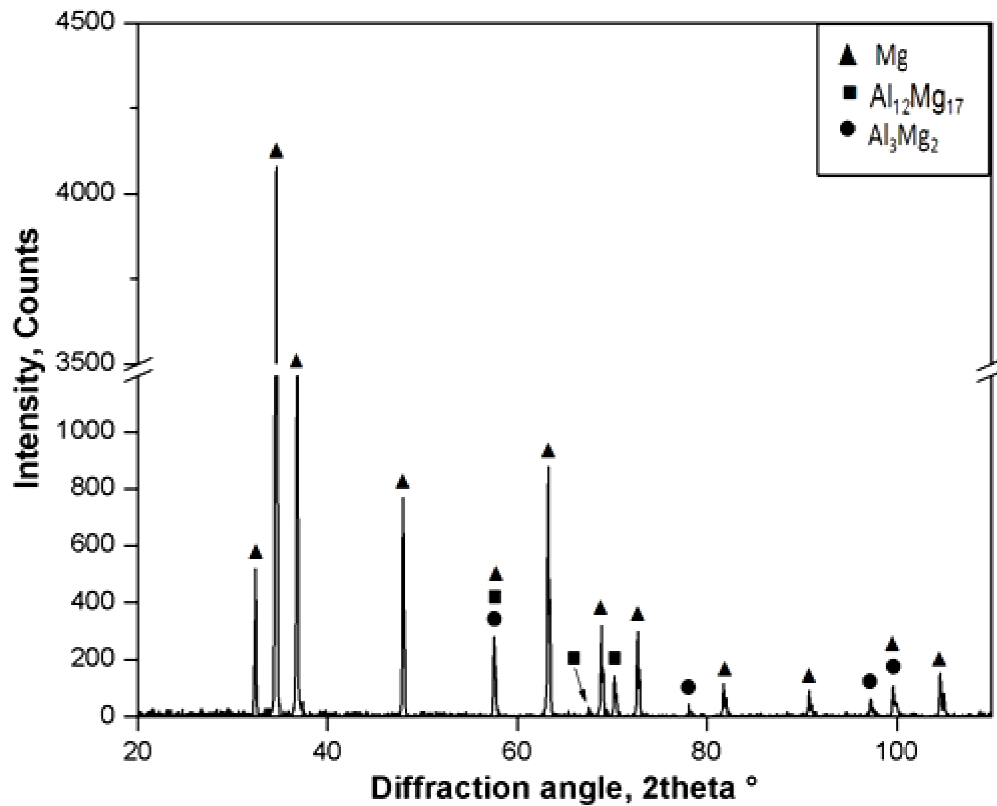
Fig.7.3 X-ray diffraction pattern obtained from the fracture surface of the dissimilar Mg/Al adhesive weld on the Mg side.

7.2 Microhardness

The hardness distribution across the Al/Mg and Mg/Al adhesive welds obtained from the upper and lower sheets is shown in Fig 7.4(a) and Fig. 7.4(b), respectively. There was only a small

difference in hardness between the upper and lower sheets and the hardness increased progressively close to the keyhole periphery. As shown in Fig. 7.4(a), the hardness distribution of the Al/Mg adhesive weld was observed to be nearly symmetric with respect to the center of the keyhole. As shown in Fig. 7.4(a) and Fig. 7.4(b), the SZ in the Al/Mg and Mg/Al adhesive welds had much higher hardness values lying in-between 90 and 125 HV. This higher hardness was predominantly due to the presence of hard and brittle IMCs (Al_3Mg_2 and $Al_{12}Mg_{17}$ phases), as identified by XRD (Fig. 7.3). Similar results were also reported by other researchers [71,137-138,142-144]. Therefore, the microhardness test results provided a further corroboration for the occurrence of hard IMCs in the Al/Mg and Mg/Al adhesive welds, which may become an easy fracture path to be discussed in the sections below.
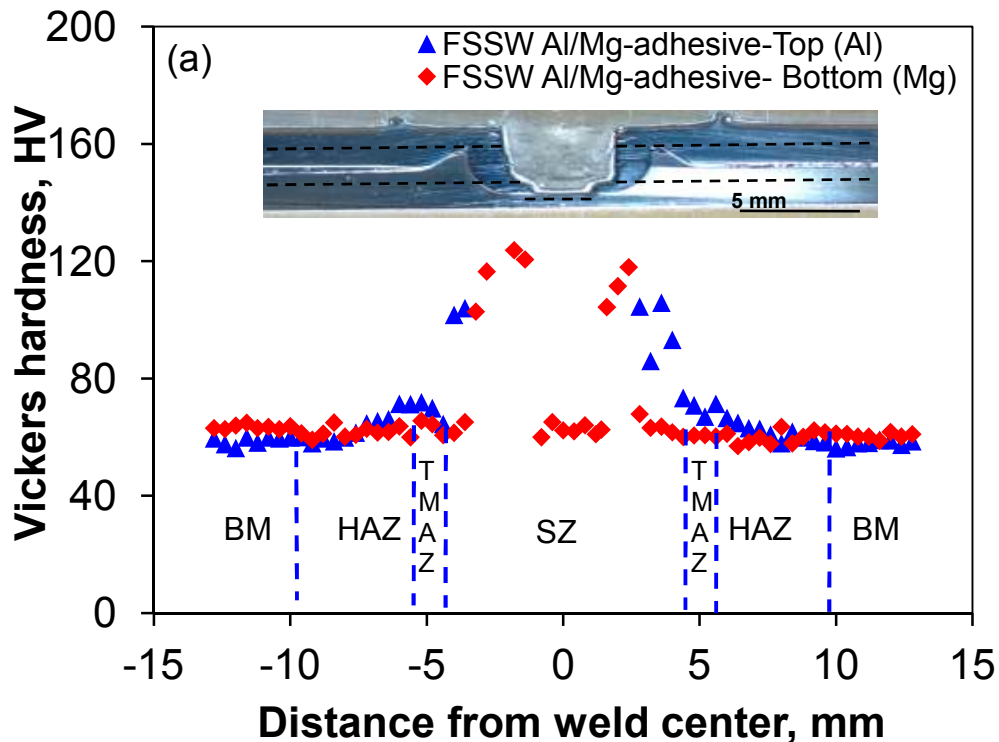
Fig.7.4 Typical microhardness profiles of the dissimilar (a) Al/Mg, and (b) Mg/Al adhesive welds at different locations. (continued)
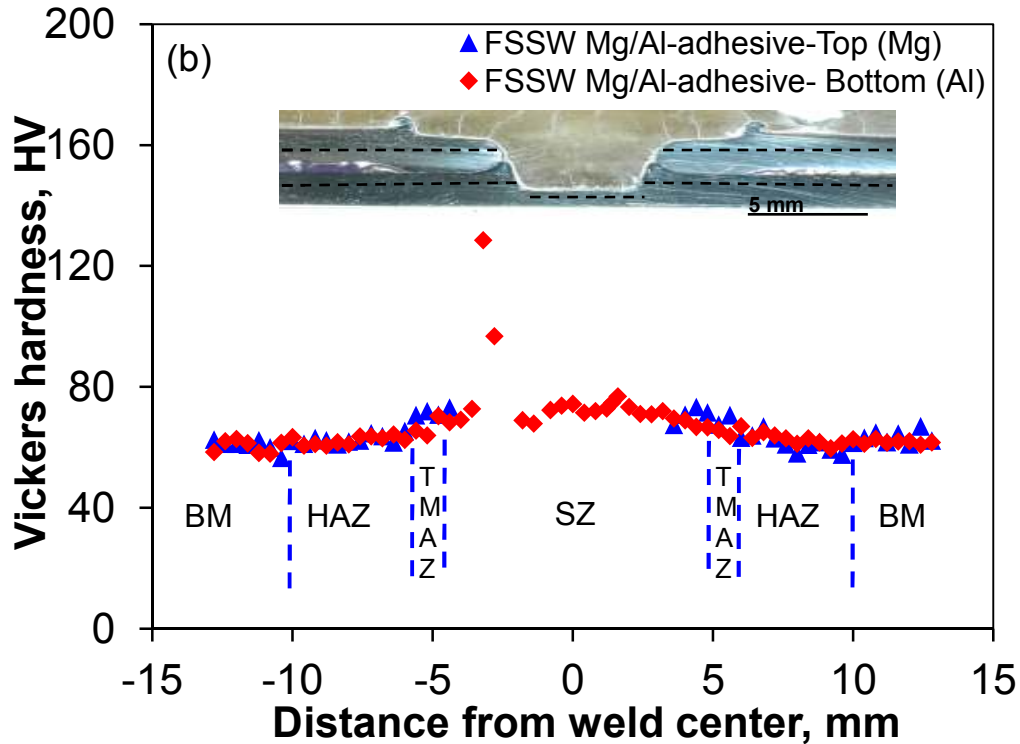
Fig.7.4 Typical microhardness profiles of the dissimilar (a) Al/Mg, and (b) Mg/Al adhesive welds at different locations.

7.3 Lap shear strength

Typical load vs. displacement curves for the Al/Mg as well as the Al/Mg and Mg/Al adhesive welds are shown in Fig. 7.5(a). It is seen that both the Al/Mg and Mg/Al adhesive welds were much stronger than the Al/Mg weld, and the Mg/Al adhesive weld was in turn stronger than the Al/Mg adhesive weld. The maximum lap shear load that was obtained is shown in Fig. 7.5(b). It is clear that the maximum lap shear load of the Mg/Al adhesive weld was higher than that of the Al/Mg adhesive weld, which was in turn higher than that of the Al/Mg weld. The considerably lower maximum lap shear load in the Al/Mg weld is obviously attributed to the formation of the brittle IMC layer at the interface and decreasing the extent of IMC formation at the interface by using an adhesive in the Mg/Al adhesive weld resulted in a higher lap shear load. A similar

observation of the maximum lap shear load was also reported by Liu and Ren [78] for 1.5-mm thick MIG spot adhesive welded AZ31 to AA 6061 sheets; they reported that the maximum lap shear load increased by three times compared to that of the MIG welded joint without the adhesive. Higher lap shear loads for laser adhesive welding of AZ31 to AA6061 alloy was also reported [79,80]. To characterize more completely the lap shear characteristics of the welds, failure energy was estimated in the present work, where the failure energy was defined as the area below the load-displacement curve shown in Fig. 7.5(a). When the tensile lap shear remained continuous after reaching the maximum load without failure (i.e., in the case of Al/Mg and Mg/Al adhesive welds in the present study), the failure energy was only calculated corresponding to the maximum load in a more conservative manner. The failure energy results are plotted in Fig. 7.5(c). The failure energy of the Mg/Al adhesive weld (~26.5 J) was greater than that of the Al/Mg adhesive weld (~9.5 J) and both of these values were substantially greater than than that of the Al/Mg weld (~0.34 J). Hence the application of an adhesive during FSSW influences markedly the joint stability through the presence of a large lap bonded area. Also, since there exists a direct correlation between the failure energy in the lap shear tensile tests and impact tests, it is expected that the Mg/Al adhesive weld would have a higher impact resistance than that of the Al/Mg adhesive weld. Furthermore, nugget pullout failure was observed for the Al/Mg and Mg/Al adhesive welds while nugget debonding failure was observed for the Al/Mg weld during lap shear tensile tests (Fig. 7.5(a)). Therefore, the presence of adhesive provided a further corroboration on a higher lap shear strength for the Al/Mg and Mg/Al adhesive weld which attributed with different failure modes to be seen in the later sections.
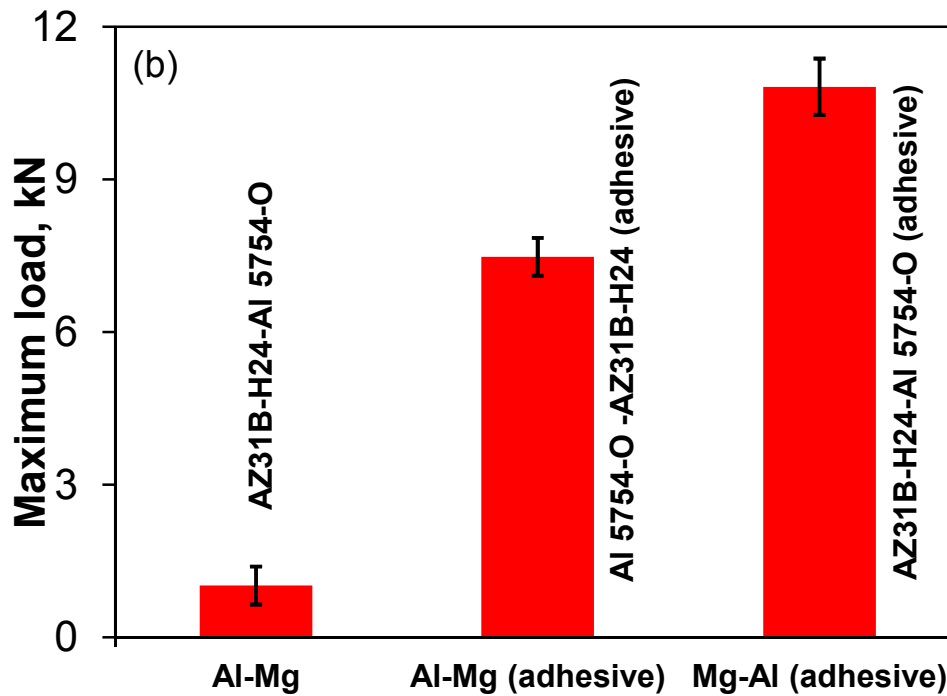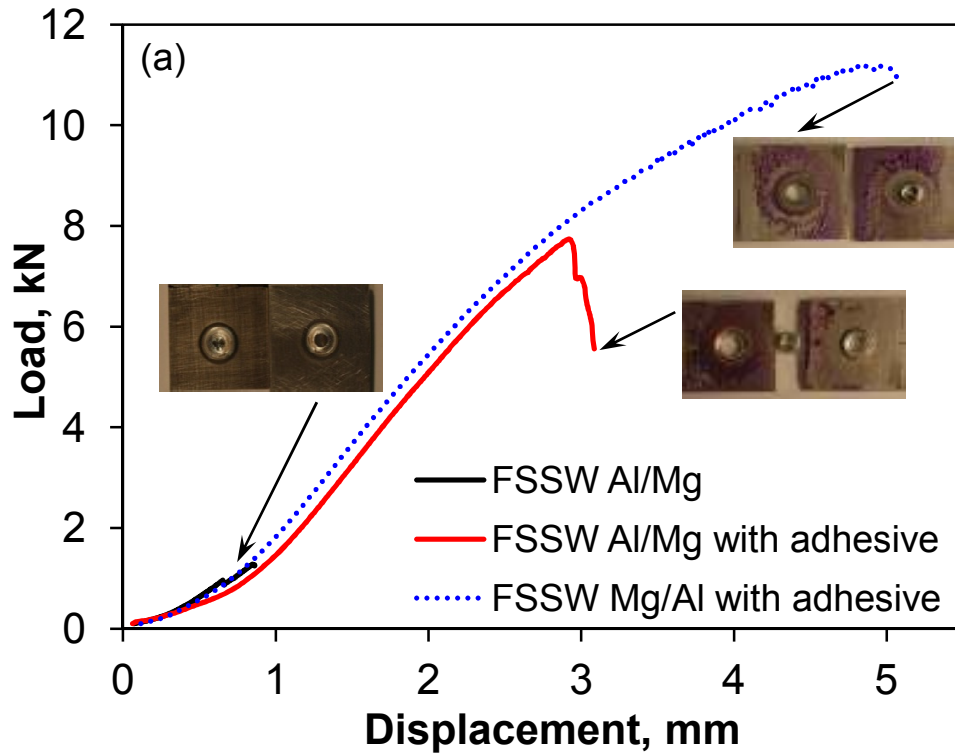
Fig.7.5 Lap shear properties of the dissimilar Al/Mg weld, Al/Mg adhesive weld and Mg/Al adhesive weld tested at a crosshead speed of 10 mm/min (a) load vs. displacement curves, and (b) maximum load, and (c) failure energy.(continued)
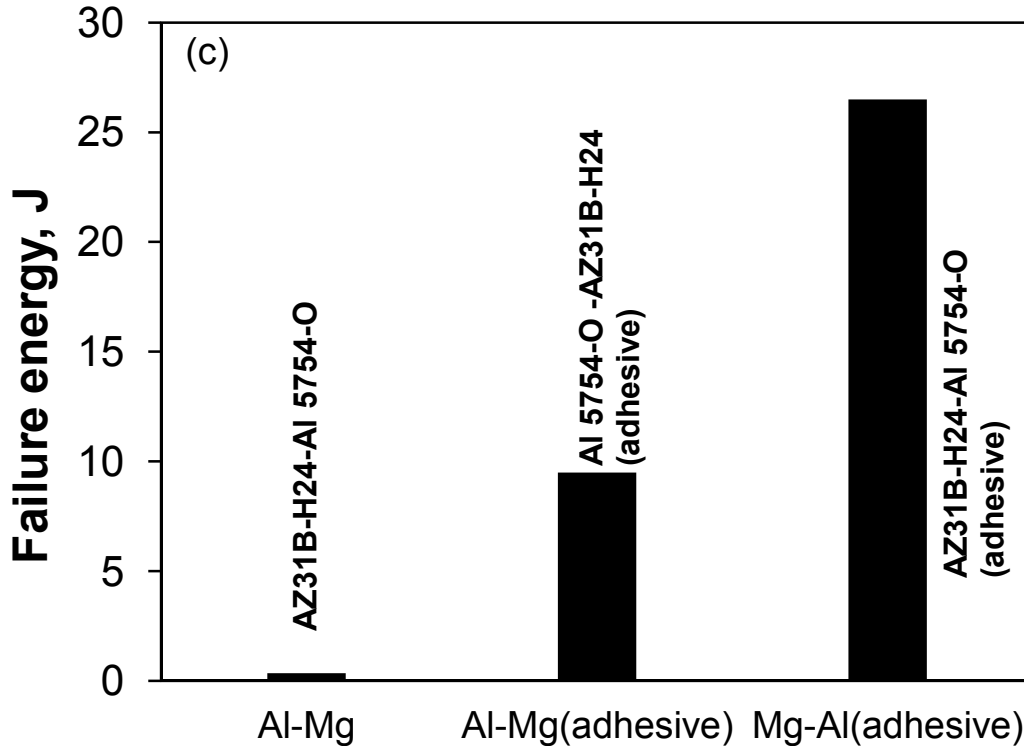
Fig.7.5 Lap shear properties of the dissimilar Al/Mg weld, Al/Mg adhesive weld and Mg/Al adhesive weld tested at a crosshead speed of 10 mm/min (a) load vs. displacement curves, and (b) maximum load, and (c) failure energy.

7.4 Fatigue behavior and failure mode

Fatigue test results of the Al/Mg, as well as the Al/Mg and Mg/Al welds with an adhesive obtained at RT, R=0.2, and 50 Hz are plotted in Fig. 7.6. Resembling the maximum load and failure energy (Fig. 7.5(a) and Fig. 7.5(c)), the fatigue life of the Mg/Al adhesive weld was in general longer than that of the Al/Mg adhesive weld. The fatigue life of the Al/Mg dissimilar weld was much lower and more scattered than that of both the Mg/Al and Al/Mg adhesive welds especially at a maximum cyclic load higher than 1 kN. The greatly improved fatigue resistance of the Mg/Al and Al/Mg adhesive welds was primarily attributed to the elimination of stress concentration surrounding the weld nugget as a result of large lap bonded area which may lessen the formation of IMC layer at the interface and lead to uniform stress distribution in the lap joint

during fatigue testing. Similarly, a longer fatigue life for the resistance spot adhesive welded AZ31 to HSLA steel sheets was reported in comparison with that of joint assembled without an adhesive under the same cyclic loading condition (R = 0.2, f = 50 Hz) [85].
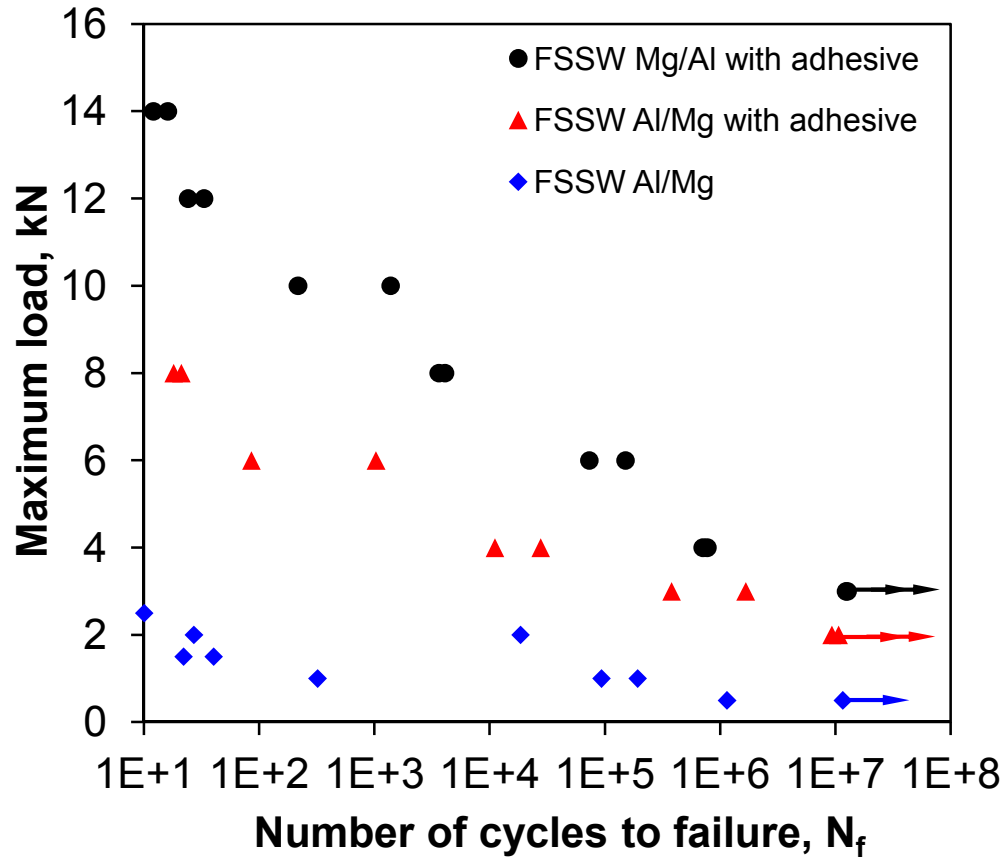
Fig.7.6 S-N curves of the dissimilar Al/Mg weld, Al/Mg adhesive weld and Mg/Al adhesive weld tested at R = 0.2, 50 Hz and room temperature.

Fig. 7.7(a) reveals the onion ring shaped weld nugget (Al 87 wt%, Mg 13 wt% determined by EDS) that was pulled out from the top and bottom sheets of the Al/Mg adhesive welds at the maximum cyclic load of 8 kN. The nugget pullout failure occurred as the crack propagated circumferentially around the nugget. The shear stress in the remaining area of the nugget increased with each advancement of the crack front. After the crack had propagated around half

of the nugget with a keyhole, the shear stresses acting in the area were such that the remaining cross section could not sustain the shear overload, then the nugget pullout failure occurred. In contrast, the failure of the Al/Mg adhesive weld occurred nearly at a right angle to the loading direction at the maximum cyclic load below 3 kN (Fig. 7.7(b)). Nugget pull out failure mode was observed in the Mg/Al adhesive weld for both high and low cyclic loads (Fig. 7.8(a) and Fig.7.8(b)).

7.5 Fractography

Figs.7.7 and 7.8 show SEM images of the fatigue fracture surfaces of the Al/Mg and Mg/Al adhesive welds and the load dependence of the failure mode. At a lower level of maximum cyclic loads as shown in Fig.7.7(b)-(e) for the Al/Mg adhesive weld, fatigue cracking was caused by the opening of the keyhole through crack initiation and then propagation progressed at right angles to the loading direction. Fatigue crack propagation was mainly characterized by the formation of fatigue striations (Fig. 7.7(e) and Fig. 7.8(e)) in conjunction with secondary cracks, which appeared usually perpendicular to the fatigue crack propagation direction. The fatigue striations usually occurred by a repeated plastic blunting-sharpening process in the face-centered cubic materials, stemming from the glide of dislocations on the slip plane along the slip direction within the plastic zone ahead of a fatigue crack tip [110]. The formation of fatigue striations in the magnesium alloys with a hexagonal close-packed crystal structure was expected to be additionally associated with the occurrence of twinning-detwinning process [11,64,111,112,146,147], since there exist a lower number of slip systems in magnesium alloys at room temperature. On the other hand, at the higher maximum cyclic load for Al/Mg adhesive weld, as shown in Fig 7.7(f), and at both higher and lower maximum cyclic load for Mg/Al adhesive weld (Fig.7.8(c)-(d)), the fatigue crack initiated in region A, propagated towards region

B along the circumferential direction and finally fractured in the mode of nugget pullout in region C located in the SZ. The ridge in region A had roots in the upward material flow of the lower sheet [148], but it should be noted that only a small amount of the lower sheet material underneath the hook flowed upward into the upper sheet. In a previous study by the authors [149], nugget debonding fracture mode was observed for the Al/Mg dissimilar weld. Again, the presence of IMC layers of Al_3Mg_2 and $Al_{12}Mg_{17}$ phases, as observed via SEM/EDS (Fig.7.9) and identified via XRD (Fig.7.3)on the fracture surface of the Mg/Al adhesive weld (Mg side), which considerably decreased the fatigue life of the Mg/Al adhesive weld.
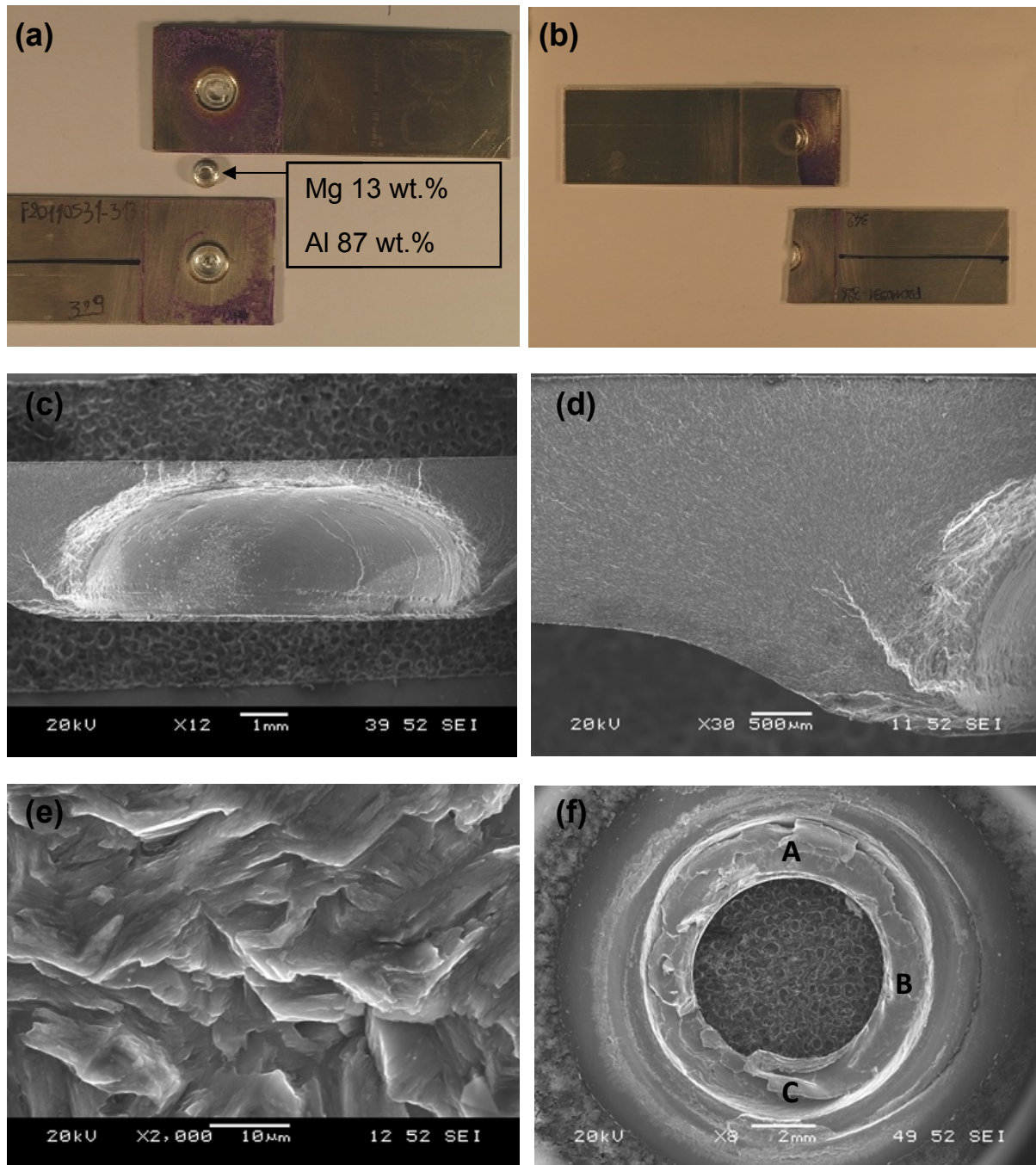
Fig.7.7 Typical macroscopic and SEM images of the fatigue fracture surface of the dissimilar Al/Mg adhesive weld (a) failure pattern at a higher maximum load P_{max}=8 kN, (b) failure pattern at a lower maximum load P_{max}=3 kN, (c) normal tensile fracture surface at a lower P_{max}=3 kN, (d) crack initiation site at a weld nugget, (e) fatigue striations in the crack propagation zone at a higher magnification, and (f) nugget pull out fracture surface at a higher P_{max}=8 kN.
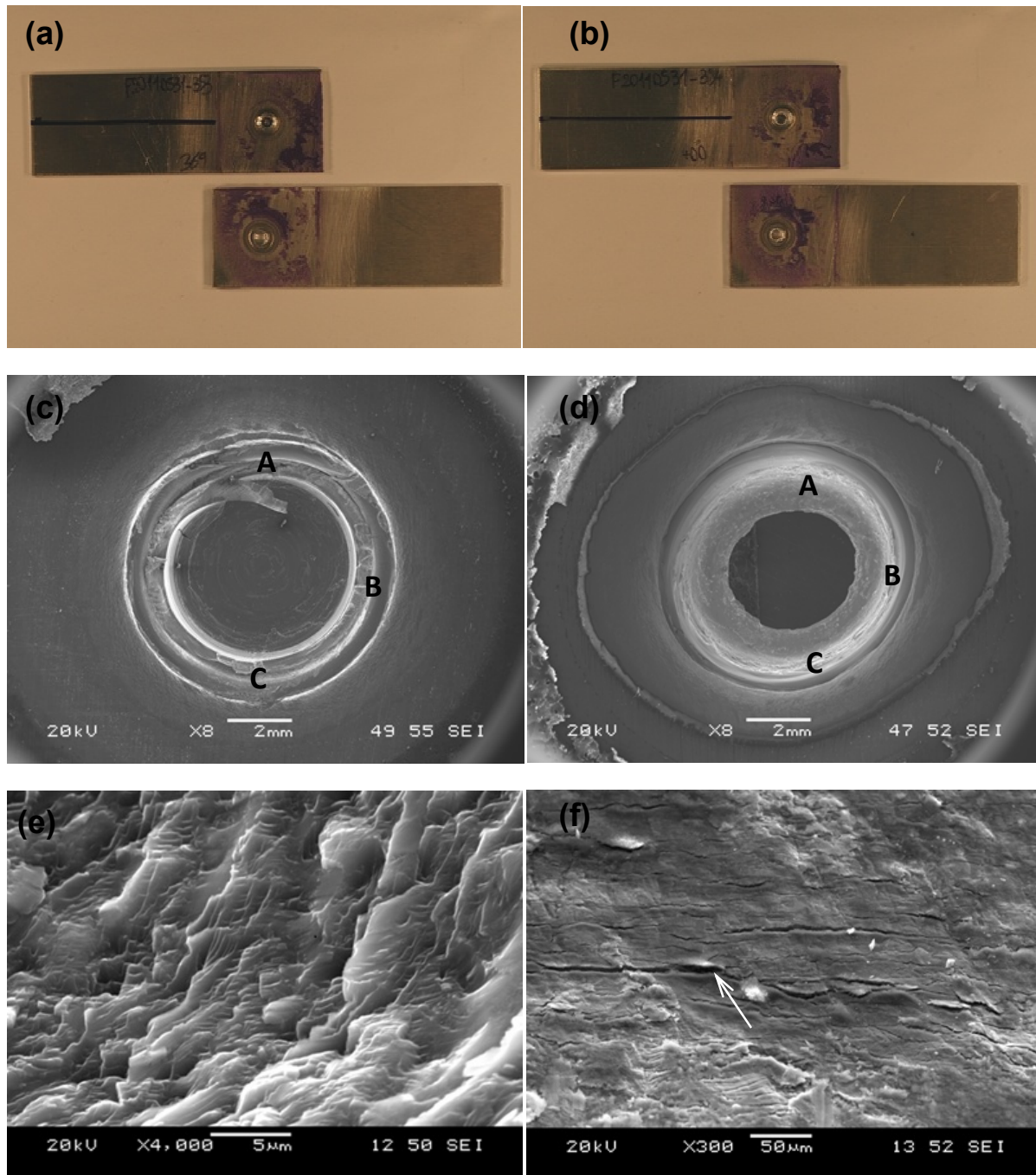
Fig.7.8 Typical macroscopic and SEM images of the fatigue fracture surface of the dissimilar Mg/Al adhesive weld (a) failure pattern at a lower maximum load P_{max}=4 kN, (b) failure pattern at a higher maximum load P_{max}=8 kN, (c) nugget pull out fracture surface at a lower P_{max} =4 kN, (d) nugget pull out fracture surface at a higher P_{max} =8 kN, (e) fatigue striations in the crack propagation zone at a higher magnification, and (f)secondary crack at a higher magnification as indicated by an arrow at a higher P_{max} =8 kN.
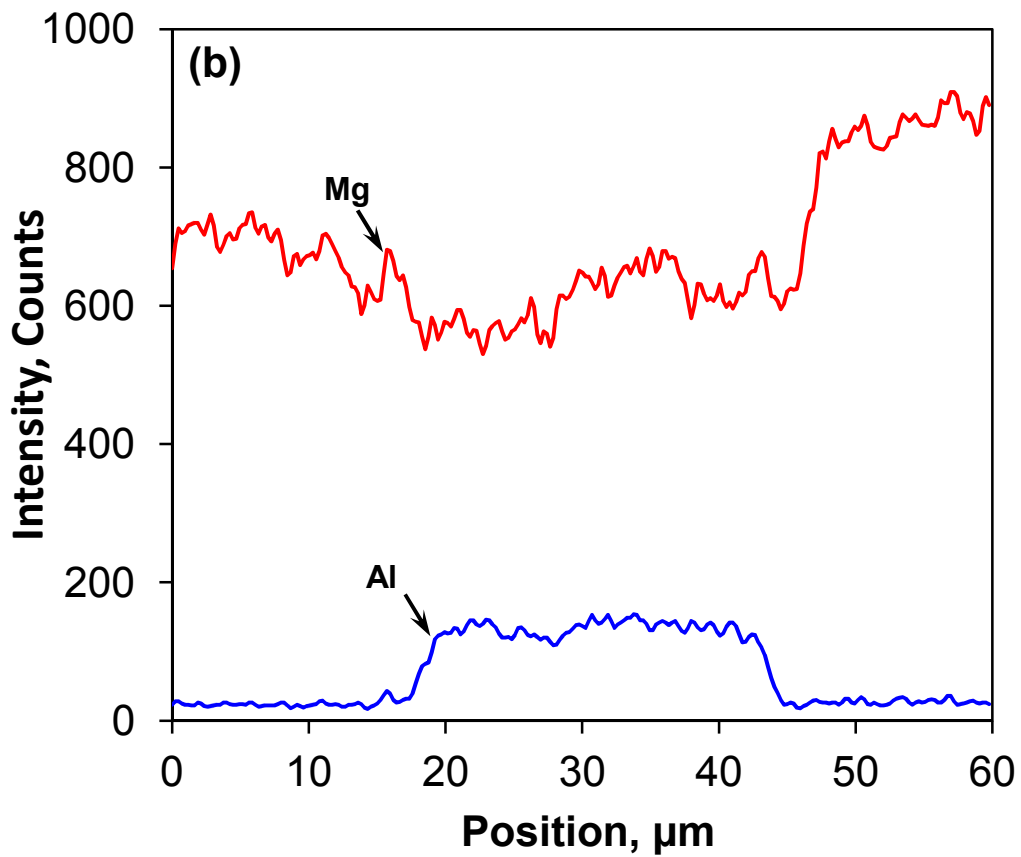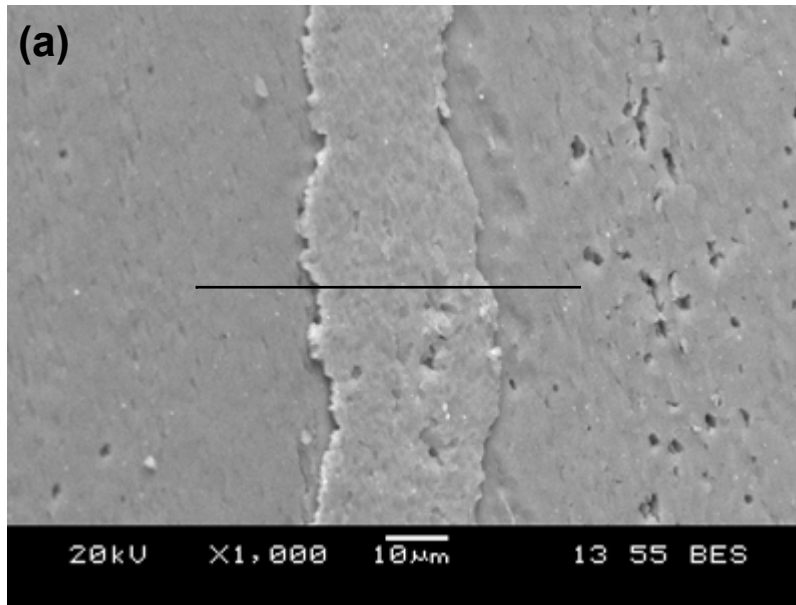
Fig.7.9 (a) A typical SEM micrograph of the Al-Mg phase on the fracture surface of dissimilar Mg/Al adhesive weld (Mg side), and (b) EDS line scan across the intermetallic indicated in (a) showing the Al and Mg compositional variations.

CHAPTER 8

SUMMARY AND FUTURE WORK

8.1 Summary

1. The microstructure of the as-received AZ31B-H24 magnesium alloy sheet consisted of some deformed and twinned grains. Fiber laser welding (FLW) of AZ31B-H24 Mg alloy at both welding speeds of 50 mm/s and 100 mm/s led to the formation of characteristic equiaxed dendrites in the center of fusion zone (FZ) and columnar dendrites near the fusion zone boundary, coupled with a large number of divorced eutectic β-$Mg_{17}Al_{12}$ particles existing mainly in the interdendritic and intergranular regions, while recrystallized grains emerged in the heat-affected zone (HAZ). The fusion zone was wider, and both the dendrite cell size in the fusion zone and the grain size in the heat-affected zone became larger at a welding speed of 50 mm/s than 100 mm/s. After friction stir welding (FSW) the grains in the stir zone (SZ) became recrystallized with an equiaxed shape with the grain size decreased with increasing welding speed and decreasing rotational rate.

2. After friction stir spot welding (FSSW) the elongated grains in the base Mg alloy became equiaxed as a result of dynamic recrystallization in the SZ of the Mg/Mg similar FSS weld, with partial recrystallization occurring in the TMAZ and HAZ. The Al/Mg dissimilar FSS weld was characterized by the formation of a distinctive interfacial layer consisting of $Al_{12}Mg_{17}$ and Al_3M_{g2} intermetallic compounds.

3. The base Mg alloy contained a strong crystallographic texture, with the basal plane (0002) largely parallel to the sheet plane and <11$\bar{2}$0> direction aligned in the rolling direction (RD). After FSW the basal planes in the SZ were slightly tilted toward the TD determined from the

sheet normal direction (top surface) and also slightly inclined toward the RD determined from the transverse direction (cross section) due to the intense shear plastic flow near the pin surface. The prismatic planes $(10\bar{1}0)$ and pyramidal planes $(10\bar{1}1)$ formed mainly fiber textures. With increasing tool rotational rate or decreasing welding speed, the maximum pole intensities of (0002) and $(10\bar{1}0)$ poles decreased.

4. After fiber laser welding (FLW) and friction stir welding (FSW) of AZ31B-H24 Mg alloy the lowest hardness appeared at the center of fusion zone (FZ) and stir zone (SZ) respectively. The microhardness profile of the Mg/Mg FSS weld exhibited a W-shaped appearance, where the hardness gradually increased towards the keyhole direction. A much higher hardness with values in-between 120 and 150 HV was observed in the stir zone underneath the bottom of the keyhole in the Al/Mg dissimilar FSS weld due to the presence of an intermetallic compound layer.

5. While fiber laser welding (FLW) resulted in a certain extent of reduction in the yield strength, ductility, and fatigue life of FLWed AZ31B-H24 Mg alloy, the decrease of the ultimate tensile strength was moderate. A joint efficiency of about 89% at a welding speed of 50 mm/s and about 91% at a welding speed of 100 mm/s was achieved. The hardening capacity and strain hardening exponent increased after laser welding. A higher welding speed led to a higher yield strength and longer fatigue life, but slightly lower strain hardening exponent and hardening capacity due to the smaller grain size coupled with the eutectic structure containing β-Mg$_{17}$Al$_{12}$ precipitates in the fusion zone and smaller recrystallized grain size in the heat-affected zone.

6. Both the strength and ductility of the AZ31B-H24 Mg alloy after friction stir welding (FSW) decreased at all the strain rates, with a joint efficiency lying in-between about 75% and 82%.

A slight increase of YS and UTS with increasing strain rate was observed, while the ductility in the base alloy decreased significantly. The welding speed and rotational rate had a stronger effect on the YS than the UTS. A higher welding speed of 20 mm/s and lower rotational rate of 1000 rpm led to higher YS, but lower ductility, strain-hardening exponent and hardening capacity. This was due to the smaller recrystallized grains in the low-hardness SZ arising from the lower heat input.

7. Both Mg/Mg and Al/Al similar FSS welds had significantly higher lap shear strength and failure energy than the Al/Mg dissimilar FSS weld. While the Mg/Mg similar FSS weld exhibited a further higher lap shear strength than the Al/Al similar FSS weld, the Al/Al similar FSS weld could endure longer since the failure energy of the Al/Al similar FSS weld was greater than that of the Mg/Mg similar FSS weld. The Mg/Al and Al/Mg adhesive FSS welds had significantly higher lap shear strength and failure energy than the Al/Mg dissimilar FSS weld. The failure energy of the Mg/Al adhesive FSS weld was higher than that of the Al/Mg adhesive FSS weld.

8. While the fatigue life of the Al/Al similar FSS weld was generally higher than that of the Mg/Mg similar FSS weld, both the Al/Al and Mg/Mg similar FSS welds had a much longer fatigue life than the Al/Mg dissimilar FSS weld especially at higher cyclic load levels. The Mg/Al and Al/Mg dissimilar adhesive FSS welds had a much longer fatigue life than the Al/Mg dissimilar FSS weld especially at higher cyclic load levels.

9. All the tensile fracture basically occurred in the fusion zone while fatigue failure occurred mainly in-between the heat-affected zone and fusion zone. Cleavage-like flat facets together with tear ridges and river marking were observed in the welded samples. Small pores on the fracture surface of the fiber laser welded joints were observed. Fatigue crack initiated from

the near-surface welding defect. At lower stress amplitudes, single crack initiation was observed while multiple crack initiation was more evident at higher stress amplitudes. Fatigue crack propagation was characterized by the formation of fatigue striations with the spacing increased with increasing distance from the initiation site, in conjunction with the presence of secondary cracks.

10. Two distinct failure modes were observed to be dependent on the cyclic load level in the similar FSS welds and dissimilar adhesive FSS welds. At higher cyclic loads nugget pullout failure occurred since fatigue crack propagated circumferentially around the nugget, while at lower cyclic loads fatigue failure occurred perpendicular to the loading direction due to the opening of the keyhole through crack initiation and then propagating at right angles to the loading direction. Fatigue crack propagation was characterized mainly by the formation of fatigue striations as well. Nugget debonding failure mode was observed in the Al/Mg dissimilar FSS weld. as a consequence of the presence of an intermetallic compound layer.

8.2. Major Contributions

The prime novel results in this study include:

1. After fiber laser welding (FLW) of AZ31B-H24 Mg alloy, the fusion zone (FZ) containing divorced eutectic β-$Mg_{17}Al_{12}$ particles as identified by XRD technique and the columnar dendrite zone near the FZ boundary were wider at a slower welding speed, and both the dendrite cell size in the FZ and heat-affected zone (HAZ) become larger which corresponding to the lower hardness, yield strength and shorter fatigue life.

2. After friction stir welding (FLW) of AZ31B-H24 Mg alloy, the basal planes (0002) in the stir zone (SZ) tilted toward the transverse direction (TD) and rolling direction (TD), and the

prismatic planes ($10\bar{1}0$) and pyramidal planes ($10\bar{1}1$) formed fiber textures due to the severe shear plastic flow near the pin surface. Despite the lower ductility and hardening capacity, higher yield strength is achieved at a higher welding speed and lower rotational rate due to the smaller recrystallized grains and stronger basal texture in the stir zone.

3. After friction stir spot welding (FSSW) and friction stir spot adhesive welding of AZ31B-H24 Mg alloy and 5754-O Al alloy, the Al/Mg dissimilar FSS welds with/without adhesive were characterized by the formation of a distinctive interfacial layer consisting of $Al_{12}Mg_{17}$ and Al_3Mg_2 intermetallic compounds. The microhardness profile of the Mg/Mg similar FSS weld exhibited a W-shaped appearance, where the hardness gradually increased towards the keyhole direction. The Al/Al and Mg/Mg similar FSS welds and Al/Mg dissimilar adhesive FSS welds had significantly higher lap shear strength, failure energy and longer fatigue life than the Al/Mg dissimilar weld. Nugget pullout failure and fatigue failure were observed to be dependent on the cyclic load level in the Al/Al and Mg/Mg similar welds and Al/Mg dissimilar adhesive FSS welds. Nugget debonding failure mode was observed in the Al/Mg dissimilar weld.

8.3 Recommendation for Future Work

In the present study a number of joining methods were studied with special attention to the microstructural changes and mechanical properties. Different groups of FLWed and FSWed joints were compared and tested to identify the optimum welding parameters for maximizing the joint efficiency. The lap shear strength and fatigue resistance of the friction stir spot welded similar AZ31B-H24 and AA5754-O alloy, and dissimilar AZ31-to-AA5754 alloy joints with and

without adhesive were also evaluated and compared. However, more studies are needed in the aspect of joining technology on the Mg AZ31 alloy and Al 5754 alloy.

1. In the FLW process only two welding conditions were utilized to evaluate the microstructure and mechanical properties. More systematic studies need to be done by increasing or decreasing the welding speed. It is assumed that after FLW, texture of the welding zone was changed completely or partly from the BM. Texture identification on the fracture surface or weld zone by XRD would be a piece of interesting research work.

2. In the FSW the mechanical properties among the three groups of joints were not significantly different. This might be related to the base material having only 2 mm thickness. Thicker material should be welded with a large change of welding parameters to better examine the change in the mechanical properties among the FSWed joints made with different welding parameters.

3. In the present study, the YS and UTS were observed to increase with increasing welding speed and decreasing rotational rate during FSW. However, the optimal welding parameters to achieve the maximum YS and UTS need to be identified.

4. The lap shear strength and fatigue resistance of the friction stir spot welded similar AZ31B-H24 and AA5754-O alloy, and dissimilar AZ31-to-AA5754 alloy joints with and without adhesive were conducted by using one welding condition only. More studies with varying welding parameters are needed.

REFERENCES

[1] T.M. Pollock, Weight Loss with Magnesium Alloys, Science, 2010, 328, 986-87.

[2] M. Wise, K. Calvin, A. Thomson, L. Clarke, B. Bond-Lamberty, R. Sands, S.J. Smith, A. Janetos, and J. Edmonds, Implications of limiting CO_2 concentrations for land use and energy, Science, 2009, 324, 1183-86.

[3] E. Alonso, T.M. Lee, C. Bjelkengren, R. Roth, and R.E. Kirchain, Evaluating the potential for secondary mass savings in vehicle lightweighting, Environ. Sci. Technol., 2012 dx.doi.org/10.1021/es202938m, in print.

[4] H.-J. Kim, G.A. Keoleian, and S.J. Skerlos, Economic assessment of greenhouse gas emissions reduction by vehicle lightweighting using aluminum and high-strength steel, J. Ind. Ecol., 2011, 15(1), 64-80.

[5] H.-J. Kim, C. McMillan, G.A. Keoleian, and S.J. Skerlos, Greenhouse gas emissions payback for lightweighted vehicles using aluminum and high-strength steel, J. Ind. Ecol., 2010, 14(6), 929-46.

[6] D. Shindell, G. Faluvegi, M. Walsh, S.C. Anenberg, R.V. Dingenen, N.Z. Muller, J. Austin, D. Koch, and G. Milly, Climate, health, agricultural and economic impacts of tighter vehicle-emission standards, Nature Clim. Change, 2011, 1, 59-66.

[7] D.A. Howey, A challenging future for cars, Nature Clim. Change, 2012, 2, 28-29.

[8] Z. Zhang, X. Yang, J. Zhang, G. Zhou, X. Xu, and B. Zou, Effect of welding parameters on microstructure and mechanical properties of friction stir spot welded 5052 aluminum alloy, Mater. Des., 2011, 32, 4461-70.

[9] J.B. Jordon, J.B. Gibson, M.F. Horstemeyer, H.EI. Kadiri, J.C. Baird, and A.A. Luo, Effect of twinning, slip, and inclusions on the fatigue anisotropy of extrusion-textured AZ61 magnesium alloy,Mater. Sci. Eng. A, 2011, 528(22-23), 6860-71.

[10] Q. Yu, J.X. Zhang, Y.Y. Jiang, and Q.Z. Li,Effect of strain ratio on cyclic deformation and fatigue of extruded AZ61A magnesium alloy, Int. J. Fatigue, 2012, 36, 47-58.

[11] S. Begum, D.L. Chen, S. Xu, and A.A. Luo, Effect of strain ratio and strain rate on low cycle fatigue behavior of AZ31 wrought magnesium alloy,Mater. Sci. Eng. A, 2009, A517(1-2), 334-43.

[12] C.L. Fan, D.L. Chen, and A.A. Luo, Dependence of the distribution of deformation twins on strain amplitudes in an extruded magnesium alloy after cyclic deformation, Mater. Sci. Eng. A, 2009, A519(1-2), 38-45.

[13] H.Y. Wu, J.C. Yang, J.H. Liao, and F.J. Zhu, Dynamic behavior of extruded AZ61 Mg alloy during hot compression, Mater. Sci. Eng. A, 2012, 535, 68-75.

[14] H. Kang, I. Accorsi, B. Patel, and E. Pakalnins, Fatigue performance of resistance spot welds in three sheet stack-ups, Procedia Eng., 2012, 2, 129-38.

[15] H.Y. Wang, L.M. Liu, and Z.Y. Jia, The influence of adhesive on the Al alloy in laser weld bonding Mg–Al process, J. Mater. Sci., 2011, 46, 5534-40.

[16] S.J. Liang, H.F. Sun, and Z.Y. Liu, E. Wang, Mechanical properties and texture evolution during rolling process of an AZ31 Mg alloy, J. Alloy Compd., 2009, 472, 127-32.

[17] J.B. Jiang and Z.D. Zhang,The study on the plasma arc weld bonding process of magnesium alloy, J. Alloy Compd., 2008, 466, 368-72.

[18] V.X. Tran, J. Pan, and T. Pan, Fatigue behavior of aluminum 5754-O and 6111-T4 spot friction welds in lap-shear specimens, Int. J. Fatigue, 2008, 30, 2175-90.

[19] Y. Sakai, K. Nakata, T. Tsumura, M. Ueda, T. Ueyama, and K. Akamatsu, Fiber laser welding of noncombustible magnesium alloy,Mater. Sci. Forum, 2008, 580-582, 479-82.

[20] J. Liu, J.H. Dong, and K. Shinozaki, Microstructures and properties of fiber laser welded ACM522 magnesium alloy joint, Mater. Sci. Forum, 2009, 610-613, 911-14.

[21] L. Yu, K. Nakata, and J. Liao, Weld porosity in fibre laser weld of thixomolded heat resistant Mg alloys, Sci. Technol. Weld. Joining, 2009, 14, 554-58.

[22] J.A. Gann and A.W. Winston, Magnesium and Its Alloys, Ind. Eng. Chem.,1927, 19(10), 1193–01.

[23] H.E. Friedrich and B.L. Mordike, Magnesium Technology-Metallurgy, Design Data, Applications, Springer-Verlag Berlin Heidelberg, Germany, 2006.

[24] S.H. Chowdhury, D.L. Chen, S.D. Bhole, X. Cao and P. Wanjara, Friction stir welded AZ31 magnesium alloy: Microstructure, texture and tensile properties, Metall. Mater. Trans. A, 2012, submitted.

[25] C. Grard, Aluminum and Its alloy, Constable and company ltd., 1921, 3-226

[26] J.R. Kissell, Aluminum alloys, Handbook of materials for product design, McGraw-Hill, 2001, 2.1-2.178

[27] K.U. Kainer, Magnesium Alloys and Technology, Wiley-VCH, Cambridge, 2003.

[28] W.F. Smith, Structure and properties of Engineering alloys, McGraw-Hill, Inc, New York, 1993.

[29] W.M. Thomas, E.D. Nicholas, J.C. Needham, M.G. Church, P. Templesmith and C.J. Dawes, GB Patent Application No. 9125978.9, 1991.

[30] S.A. Emam and A.E. Domiaty, A refined energy-based model for friction-stir welding, Eng. Technol., 2009, 53, 1016-22.

[31] W. Xu, D. Westerbaan, S.S. Nayak, D.L. Chen, F. Goodwin, E. Biro, Y. Zhou, Microstructure and fatigue performance of single and multiple linear fiber laser weled DP980 dual phase steel, Mater. Sci. Eng. A, 2012, 553, 51-58.

[32] S.H. Chowdhury, D.L. Chen, S.D. Bhole, E. Powidajko, D.C. Wechman and Y. Zhou, Fiber laser welded AZ31 magnesium alloy: Effect of welding speed on microstructure and mechanical properties, Metall. Mater. Trans. A, 2012, 43A, 2133-47.

[33] P. Thornton, A.R. Krause, and R.G. Davies, The aluminum spot weld, Weld. J. (Miami, FL, US), 1996, 75, 101-8.

[34] A. Gean, S.A. Westgate, J.C. Kucza, and J.C. Ehrstorm, Static and fatigue behavior of spot-welded 5182-O aluminum alloy sheet, Weld. J. (Miami, FL, US), 1999, 78, 80-86.

[35] L. Liu, L. Xiao, J.C. Feng, Y.H. Tian, S.Q. Zhou, and Y. Zhou, Resistance-spot-welded AZ31 magnesium alloys: Part II: Effects of welding current on microstructure and mechanical properties, Metall. Mater. Trans. A, 2010, 41(10), 2642-50.

[36] L. Xiao, L. Liu, Y. Zhou, and S. Esmaeili, Resistance-spot-welded AZ31 magnesium alloys: Part I. Dependence of fusion zone microstructures on second-phase particles, Metall. Mater. Trans. A, 2010, 41A, 1511-22.

[37] D.Q. Sun, B. Lang, D.X. Sun, and J.B. Li, Microstructure and mechanical properties of resistance spot welded magnesium alloy joints, Mater. Sci. Eng.A, 2007, 460-461, 494-98.

[38] L. Xiao, L. Liu, D.L. Chen, S. Esmaeili, and Y. Zhou, Resistance spot weld fatigue behavior and dislocation substructures in two different heats of AZ31 magnesium alloy, Mater.Sci. Eng. A, 2011, 529, 81-87.

[39] R.S. Mishra and M.W. Mahoney, Friction stir welding and processing, ASM international, 2007, 235-72.

[40] A. Weisheit, R. Galun, and B.L. Mordike, CO2 laser beam welding of magnesium-based alloys, Weld. J., 1998, 77, 149-54.

[41] H. Zhao and T. Debroy, Pore formation during laser beam welding of die-cast magnesium alloy AM60B - Mechanism and remedy, Weld. J., 2001, 80, 204-10.

[42] Z. Sun, D. Pan, and J. Wei, Comparative evaluation of tungsten inert gas and laser *welding* of AZ31 magnesium alloy, Sci. Technol. Weld. Joining, 2002, 7, 343-51.

[43] Y.J. Quan, Z.H. Chen, X.S. Gong, and Z.H. Yu, Effect of heat input on microstructure and tensile properties of laser welded magnesium alloy AZ31, Mater. Character., 2008, 59, 1491-97.

[44] L.M. Liu and C.F. Dong, Gas tungsten-arc filler welding of AZ31 magnesium alloy, Mater. Lett., 2006, 60, 2194-97.

[45] J. Zhu, L. Li, and Z. Liu,CO_2 and diode laser welding of AZ31 magnesium alloy, Appl. Surf. Sci., 2005, 247, 300-6.

[46] L. Quintino, A. Costa, R. Miranda, D. Yapp, V. Kumar, and C.J. Kong, Welding with high power fiber lasers - A preliminary study, Mater. Des., 2007, 28 (4), 1231-37.

[47] X. Cao and M. Jahazi, Effect of welding speed on the quality of friction stir welded butt joints of a magnesium alloy, Mater. Des., 2009, 30, 2033-42.

[48] S.H. Kim, B.S. You, B.S. You and C.D. Yim, The effect of rolling conditions on the microstructure and texture evolution of AZ31 Mg alloy sheets, Mater. Forum, 2005, 29, 530-35.

[49] R. Johnson, Friction stir welding of magnesium alloys, Mater. Sci. Forum, 2003, 419-422, 365-70.

[50] X.H. Wang and K. Wang, Microstructure and properties of friction stir butt-welded AZ31 magnesium alloy, Mater. Sci. Eng. A, 2006, 431, 114-17.

[51] S.H.C. Park, Y.S Sato, and H. Kokawa, Effect of micro-texture on fracture location in friction stir weld of Mg alloy AZ61 during tensile test, Scripta Mater., 2003, 49, 161-66.

[52] M. Fairman, N. Afrin, D.L. Chen, X.J. Cao, and M. Jahazi, Microstructural evaluation of friction stir processed AZ31B-H24 magnesium alloy, Can. Metall. Quart., 2007, 46, 425-32.

[53] N. Afrin, D.L. Chen, X. Cao, and M. Jahazi, Microstructure and tensile properties of friction stir welded AZ31B magnesium alloy, Mater. Sci. Eng.A, 2008, 472, 179-86.

[54] M. Pareek, A. Polar, F. Rumiche, and J.E. Indacochea, Metallurgical evaluation of AZ31B-H24 magnesium alloy friction stir welds, J. Mater. Eng. Perform., 2007, 16, 655-62.

[55] S. Lim, S. Kim, C.G. Lee, C.D. Yim, and S.J. Kim, Tensile behavior of friction-stir-welded AZ31-H24 Mg alloy, Metall. Mater. Trans. A, 2005, 36, 1609-12.

[56] W. Woo, H. Choo, M.B. Prime, Z. Feng, and B. Clausen, Microstructure, texture and residual stress in a friction-stir-processed AZ31B magnesium alloy, Acta Mater., 2008, 56, 1701-11.

[57] L. Commin, M. Dumont, J.E. Masse, and L. Barrallier, Friction stir welding of AZ31 magnesium alloy rolled sheets: Influence of processing parameters, Acta Mater., 2009, 57, 326-34.

[58] N. Afrin, D.L. Chen, X. Cao, and M. Jahazi, Strain hardening behaviour of a friction stir welded magnesium alloy, Scripta Mater., 2007, 57, 1004-07.

[59] T.U. Seidel and A.P. Reynolds, Visualization of the material flow in AA2195 friction-stir welds using a marker strain technique, Metall. Mater. Trans. A, 2001, 32, 2879-84.

[60] R.S. Mishra and Z.Y. Ma, Friction stir welding and processing, Mater. Sci. Eng. R, 2005, 50, 1-78.

[61] R. Nandan, T. DebRoy, and H.K.D.H. Bhadeshia, Recent advances in friction-stir welding - process, weldment structure and properties, Prog. Mater. Sci., 2008, 53, 980-23.

[62] S.H.C. Park, Y.S. Sato, and H. Kokawa, Basal plane texture and flow pattern in friction stir weld of a magnesium alloy, Metall. Mater. Trans. A, 2003, 34, 987-94.

[63] J. Liao, N. Yamamoto, and K. Nakata, Effect of dispersed Intermetallic particles on microstructural evolution in the friction stir weld of a fine-grained magnesium alloy, Metall. Mater. Trans. A, 2009, 40, 2212-19.

[64] X.Z. Lin and D.L. Chen,Strain hardening and strain-rate sensitivity of an extruded magnesium alloy, J. Mater. Eng. Perform., 2008, 17, 894-01.

[65] U.F. Kocks and H. Mecking, Physics and phenomenology of strain hardening: the FCC case, Prog. Mater. Sci., 2003, 48, 171-273.

[66] J.A. del Valle, F. Carreno, and O.A. Ruano, Influence of texture and grain size on work hardening and ductility in magnesium-based alloys processed by ECAP and rolling, Acta Mater., 2006, 54, 4247-59.

[67] J.A. del Valle and O.A. Ruano, Influence of the grain size on the strain rate sensitivity in an Mg-Al-Zn alloy at moderate temperatures, Scripta Mater., 2006, 55, 775-78.

[68] M. Fujimoto, S. Koga, N. Abe, Y.S. Sato, and H. kokawa, Microstructural analysis of stir zone of Al alloy produced by friction stir spot welding, Sci. Technol. Weld. Joining, 2008, 13, 663-70.

[69] R.W. Fonda, J.F. Bingert, and K.J. Colligan, Development of grain structure during friction stir welding, Scripta Mater., 2004, 51, 243-48.

[70] C.I. Chang, C. J. Lee, and J.C. Huang, Relationship between grain size and Zener-Holloman parameter during friction stir processing in AZ31 Mg alloys, Scripta Mater., 2004, 51, 509-14.

[71] Y.S. Sato, A. Shiota, H. Kokawa, K. Okamoto, Q. Yang, and C. Kim, Effect of interfacial microstructure on lap shear strength of friction stir spot weld of aluminium alloy to magnesium alloy, Sci. Technol. Weld. Joining, 2010, 15(4), 310-24.

[72] J.B. Jordon, M.F. Horstemeyer, S.R. Daniewicz, H. Badarinarayan, and J. Grantham, Material characterization and modeling of friction stir spot welds in a magnesium AZ31 alloy, J. Eng. Mater. Technol., 2010, 132, 041008-1-10

[73] P.C. Lin, J. Pan, and T. Pan, Failure modes and fatigue life estimations of spot friction welds in lap shear specimens of aluminum 6111-T4 sheets. Part 1: Welds made by a concave tool, Int. J. Fatigue, 2008, 30(1), 74-89.

[74] S. Lathabai, M.J. Painter, G.M.D. Cantin, and V.K. Tyagi, Friction Spot Joining of an Extruded Al-Mg- Si Alloy, Scripta Mater., 2006, 55, 899-02.

[75] Y. Tozaki, Y. Uematsu, and K. Tokaji, Effect of tool geometry on. microstructure and static strength in friction stir spot welded aluminum alloys, Int. J. Mach. Tool. Manu., 2007, 47, 2230-36.

[76] P.K. Mallick and L. Agarwal, Fatigue of spot friction welded joints of Mg-Mg, Al-Al and Al-Mg alloys, Society of Automotive Engineers, Warrendale, PA, SAE Technical Paper No. 2009-01-0024, 2009.

[77] Y.H. Yin, A. Ikuta, and T.H. North, Microstructural features and mechanical properties of AM60 and AZ31 friction stir spot welds, Mater. Des., 2010, 31, 4764-76.

[78] L. Liu and D. Ren, A novel weld-bonding hybrid process for joining Mg alloy and Al alloy, Mater. Des., 2011, 32, 3730-3735.

[79] H.Y. Wang, L.M. Liu, M.L. Zhu, and H. Wang, Laser weld bonding of A6061Al alloy to AZ31B Mg alloy, Sci. Technol. Weld. Joining, 2007, 12(3), 261-65.

[80] L. Liu, H. Wang, G. Song, and J. Ye, Microstructure characteristics and mechanical properties of laser weld bonding of magnesium alloy to aluminum alloy, J. Mater. Sci., 2007, 42, 565-72.

[81] ASTM Standard E8/E8M, 2008, Standard Test Methods for Tension Testing of Metallic Materials, ASTM International, West Conshohohocken, PA, 2008, doi: 10.1520/E0008/E0008M-08, www.astm.org.

[82] S.M. Chowdhury, D.L. Chen, S.D. Bhole, X. Cao, E. Powidajko, D.C. Weckman, and Y. Zhou, Microstructure and mechanical properties of fiber and diode laser welded AZ31 magnesium alloy, Metall. Mater. Trans. A, 2011, 42A, 1974-89.

[83] L.M. Liu, G. Song, and M.L. Zhu, Low-power laser/arc hybrid welding behavior in AZ-based Mg alloys, Metall. Mater. Trans. A, 2008, 39, 1702-11.

[84] S.M. Chowdhury, D.L. Chen, S.D. Bhole, X. Cao, E. Powidajko, D.C. Weckman, and Y. Zhou, Tensile properties and strain hardening behavior of double-sided arc welded and friction stir welded AZ31B magnesium alloy, Mater. Sci. Eng. A, 2010, 527, 2951-61.

[85] W. Xu, D.L. Chen, L. Liu, H. Mori, and Y. Zhou, Microstructure and mechanical properties of weld-bonded and resistance spot welded magnesium-to-steel dissimilar joints, Mater. Sci. Eng. A, 2012, 537, 11-24.

[86] D. Gery, H. Long, and P. Maropoulos, Effects of welding speed, energy input and heat source distribution on temperature variations in butt joint welding, J. Mater. Process.Technol., 2005, 167, 393-01.

[87] N. Kishore Babu and M. Ashfaq, Influence of welding speed on microstructure and mechanical properties of AZ31 magnesium alloy laser weldments, Pract. Metall., 2010, 47 (8), 426-42.

[88] C.H. Fan, Z.H. Chen, W.Q. He, J.H. Chen, and D. Chen, Effects of the casting temperature on microstructure and mechanical properties of the squeeze-cast Al–Zn–Mg–Cu alloy, J. Alloys Compd., 2010, 504 (2), L42-45.

[89] H.W. Wang, B. Li, J.C. Jie, and Z.J. Wei, Influence of thermal rate treatment and low temperature pouring on microstructure and tensile properties of AlSi7Mg alloy, Mater. Des., 2011, 32, 2992-96.

[90] Y.H. Xiong, A.M. Yang, P.J. Li, and L. Liu, Investigation on grain structure refinement of superalloy K4169,J. Aero. Mater., 2001, 21 (3), 24-28.

[91] I. Gilath, J.M. Signamarcheix, and P. Bensussan, A comparison of methods for estimating the weld-metal cooling rate in laser welds, J. Mater. Sci., 1994, 29, 3358-62.

[92] S. Kou, Welding Metallurgy, 2nd ed., Wiley, New York, NY, 2003.

[93] M.S. Turhal and T.S. Kan, Relationships between secondary dendrite arm spacing and mechanical properties of Zn-40Al-Cu alloys, J. Mater. Sci., 2003, 38, 2639-46.

[94] R.C. Zeng, W. Dietzel, R. Zettler, J. Chen, and K. U. Kainer, Microstructure evolution and tensile properties of friction-stir-welded AM50 magnesium alloy, Trans. Nonferrous Met. Soc. China, 2008, 18, S76-80.

[95] G. Padmanaban, V. Balasubramanian, and J.K. Sarin Sundar, Influences of welding processes on microstructure, hardness, and tensile properties of AZ31B magnesium alloy, J. Mater. Eng. Perform., 2010, 19 (2), 155-65.

[96] W.D. Callister Jr., Materials Science and Engineering - An Introduction, 8th ed., John Wiley & Sons, Inc., New York, USA, 2010.

[97] J. Luo, Z. Mei, W. Tian, and Z. Wang, Diminishing of work hardening electroformed polycrystalline copper with nano-sized and uf-sized twins, Mater. Sci. Eng. A, 2006, 441, 282-90.

[98] J.H. Hollomon,Tensile deformation, Trans. AIME., 1945, 162, 268-89.

[99] X.H. Chen and L. Lu, Work hardening of ultrafine-grained copper with nanoscale twins, Scripta Mater., 2007, 57, 133-36.

[100] P. Ludwik, Elemente der Technologischen Mechanik, Springer-Verlag OHG, Berlin, 1909, 32.

[101] C.W. Sinclair, W.J. Poole, and Y. Brechet, A model for the grain size dependent work hardening of Copper, Scripta Mater., 2006, 55, 739-42.

[102] I. Kovacs, N.Q. Chinh, and E. Kovacs-Csetenyi, Grain size dependence of the work hardening process in Al 99.99, Phys. Stat. Sol. A, 2002, 194, 3-18.

[103] J. Balik, P. Lukac, Z. Drozd, and R. Kuzel, Strain-hardening behaviour of AZ31 magnesium alloys, Int. J. of Mater. Res., 2009, 100 (3), 322-5.

[104] G.E. Dieter, Mechanical Metallurgy, 3 rd ed., McGraw-Hill, MA, USA, 1986.

[105] G. Padmanaban and V. Balasubramanian, Fatigue performance of pulsed current gas tungsten arc, friction stir and laser beam welded AZ31B magnesium alloy joints, Mater. Des., 2010, 31, 3724-32.

[106] L.D. Scintilla, L. Tricarico, M. Brandizzib, and A.A. Satrianoc, Nd:YAG laser weldability and mechanical properties of AZ31 magnesium alloy butt joints, J. Mater. Process. Technol., 2010, 210, 2206-14.

[107] X. Cao, M. Jahazi, J.P. Immarigeon, and W. Wallace, A review of laser welding techniques for magnesium alloys, J. Mater. Process. Technol., 2006, 171, 188-04.

[108] Y. Yu, C. Wang, X. Hu, J. Wang, and S. Yu, Porosity in fiber laser formation of 5A06 aluminum alloy, J. Mech. Sci. Technol., 2010, 24, 1077-82.

[109] K.S. Chan, Y.M. Pan, D.L. Davidson, and R.C. McClung, Fatigue crack growth mechanisms in HSLA-80 steels, Mater. Sci. Eng. A, 1997, 222, 1-8.

[110] C. Laird, Fatigue Crack Propagation, ASTM STP, 1967, 415, 131-68.

[111] S. Begum, D.L. Chen, S. Xu, and A.A. Luo, Low cycle fatigue properties of an extruded AZ31 magnesium alloy, Int. J. Fatigue, 2009, 31, 726-35.

[112] S. Begum, D.L. Chen, S. Xu, and A.A. Luo, Strain-controlled low-cycle fatigue properties of a newly developed extruded magnesium alloy, Metall. Mater. Trans. A, 2008, 39, 3014-26.

[113] A.H. Feng, D.L. Chen, and Z.Y. Ma, Microstructure and cyclic deformation behavior of a friction stir welded 7075 Al alloy, Metall. Mater. Trans. A, 2010, 41, 957-71.

[114] A.H. Feng, D.L. Chen, and Z.Y. Ma, Microstructure and low cycle fatigue of a friction stir welded 6061 aluminum alloy, Metall. Mater. Trans. A, 2010, 41A, 2626-41.

[115] A.H. Feng, D.L. Chen, and Z.Y. Ma, Effect of welding parameters on microstructure and tensile properties of friction stir welded 6061 Al joints, Mater. Sci. Forum, 2009, 618-619, 41-44.

[116] G. Gottstein and T. A. Samman, Texture development in pure Mg and Mg alloy AZ31, Mater. Sci. Forum, 2005, 495-497, 623-632.

[117] Y.N. Wang and J.C. Huang, Texture analysis in hexagonal materials, Mater. Chem. Phys., 2003, 81, 11-26.

[118] T.A. Samman and G. Gottstein, Room temperature formability of a magnesium AZ31 alloy: Examining the role of texture on the deformation mechanisms, Mater. Sci. Eng. A, 2008, 488, 406-14.

[119] I. Ulacia, S. Yi, M.T. Perez-Prado, N.V. Dudamell, F. Galvez, D. Letzig, and I. Hurtado, Texture evolution of AZ31 magnesium alloy sheet at high strain rates, 4th Inter. Conf. on High Speed forming, Columbus, Ohio, March 9-10, 2010, 189-97.

[120] K.U. Kainer, Magnesium, Proc. 7th Inter. Conf. on Magensium Alloys and Their Application, Dresden, Germany, November 6-9, 2006, 161-163.

[121] X. Li, F. Jiao, T. Al-Samman, and S. G. Chowdhury, Influence of second-phase precipitates on the texture evolution of Mg-Al-Zn alloys during hot deformation, Scripta Mater., 2012, 66, 159-62.

[122] X. Li, T. Al-Samman, S. Mu, and G. Gottstein, Texture and microstructure development during hot deformation of ME20 magnesium alloy: Experiments and simulations,Mater. Sci. Eng. A, 2011, 528, 7915-25.

[123] S.M. Chowdhury, D.L. Chen, S.D. Bhole, and X. Cao, Tensile properties of a friction stir welded magnesium alloy: effect of pin tool thread orientation and weld pitch, Mater. Sci. Eng. A, 2010, 527(21-22), 6064-75.

[124] J. Yang, B.L. Xiao, D. Wang, and Z.Y. Ma, Effects of heat input on tensile properties and fracture behavior of friction stir welded Mg-3Al-1Zn alloy,Mater. Sci. Eng. A, 2010, 527, 708-14.

[125] A. Couret and D. Caillard, An in situ study of prismatic glide in magnesium - I. The rate controlling mechanism, Acta.Metall., 1985, 33, 1447-54.

[126] L. Helis, K. Okayasu, and H. Fukutomi, Microstructure evolution and texture development during high-temperature uniaxial compression of magnesium alloy AZ31, Mater.Sci. Eng. A, 2006, 430, 98-103.

[127] H.T. Jeong and T.K. Ha, Texture development in a warm rolled AZ31 magnesium alloy J. Mater. Process.Technol., 2007, 187-188, 559-61.

[128] R.W. Fonda and K.E. Knipling, Texture development in friction stir welds, Sci. Technol. Weld. Joining, 2011, 16, 288-94.

[129] W.B. Lee, Y.M. Yeon, and S.B. Jung, Joint properties of friction stir welded AZ31B- H24 magnesium alloy, Mater. Sci. Technol., 2003, 19, 785-90.

[130] W. Woo and H. Choo, Softening behaviour of friction stir welded Al 6061-T6 and Mg AZ31B alloys, Sci. Technol. Weld. Joining, 2011, 16, 267-72.

[131] C. Hamilton, A. Sommers, and S. Dymek, A thermal model of friction stir welding applied to Sc-modified Al–Zn–Mg–Cu alloy extrusions, Int. J. Mach. Tool. Manu., 2009, 49, 230-38.

[132] W. Woo, H. Choo, D.W. Brown, P.K. Liaw, Z. Feng, M.B. Prime, and Z. Feng, Texture variation and its influence on the tensile behavior of a friction-stir processed magnesium alloy, Scripta Mater., 2006, 54, 1859-64.

[133] Z. Yu, H. Choo, Z. Feng, and S.C. Vogel, Influence of thermo-mechanical parameters on texture and tensile behavior of friction stir processed Mg alloy, Scripta Mater., 2010, 63, 1112-15.

[134] X.H. Chen, F.S. Pan, J.J. Mao, J.F. Wang, D.F. Zhang, A.T. Tang, and J. Peng, Effect of heat treatment on strain hardening of ZK60 Mg alloy, Mater. Des., 2011, 32, 1526-30.

[135] J. Shen, D. Min, and D. Wang, Effects of heating process on the microstructures and tensile properties of friction stir spot welded AZ31 magnesium alloy plates, Mater. Des., 2011, 32, 5033-5037.

[136] C. Ding, Y. Ni, C. Guo, G. Quan, and J. Ge, Study on procedure of bonding-FSSW hybrid joints of AZ31 magnesium alloy, Adv. Mat. Res., 2011, 314-316, 953-56.

[137] Y.S. Sato, S.H.C. Park, M. Michiuchi, and H. Kokawa,Constitutional liquation during dissimilar friction stir welding of Al and Mg alloys,Scripta Mater., 2004, 50, 1233-36.

[138] Y.C. Chen, K. Nakata, Friction stir lap joining aluminum and magnesium alloys Scripta Mater., 2008, 58, 433-436.

[139] A. Gerlich, P. Su, and T.H. North, Peak temperatures and microstructures in aluminium and magnesium alloy friction stir spot welds, Sci. Technol. Weld. Joining, 2005, 10, 647-52.

[140] J.L. Murray, Phase diagrams of binary magnesium alloys, 17, ASM International, Materials Park, OH, 1988.

[141] D.H. Choi, B.W. Ahn, C.Y. Lee, Y.M. Yeon, K. Song, and S.B. Jung, Formation of intermetallic compounds in Al and Mg alloy interface during friction stir spot welding, Intermetallics, 2011, 19, 125-30.

[142] D. Dietrich, D. Nickel, M. Krause, T. Lampke, M.P. Coleman, and V. Randle, Formation of intermetallic phases in diffusion-welded joints of aluminium and magnesium alloys, J. Mater. Sci., 2011, 46, 357-64.

[143] V.K. Patel, S.D. Bhole, and D.L. Chen, microstructure and mechanical properties of dissimilar welded Mg-Al joints by ultrasonic spot welding technique, Sci. Technol. Weld. Joining, 2011, 10, 647-52.

[144] V.K. Patel, S.D. Bhole, and D.L. Chen, Influence of ultrasonic spot welding on microstructure in a magnesium alloy, Scripta Mater., 2011, 65(10), 911-14.

[145] S.F. Miller, S.G. Arul, G.H. Kruger, T.Y. Pan, and A.J. Shih, Effect of localized metal matrix composite formation on spot friction welding joint strength, J. Eng. Mater. Technol., 2011, 133, 031009-1-10.

[146] H.A. Patel, D.L. Chen, S.D. Bhole, and K. Sadayappan, Cyclic deformation and twinning in a semi-solid processed AZ91D magnesium alloy, Mater. Sci. Eng. A, 2010, 528(1), 208-19.

[147] H.A. Patel, N. Rashidi, D.L. Chen, S.D. Bhole, and A.A. Luo, Cyclic deformation behavior of a super-vacuum die cast magnesium alloy, Mater. Sci. Eng. A, (2012), in print.

[148] Y. Tozaki, Y. Uematsu, and K. Tokaji, A newly developed tool without probe for friction stir spot welding and its performance, J. Mater. Process. Technol., 2010, 210, 844-51.

[149] S.H. Chowdhury, D.L. Chen, S.D. Bhole, X. Cao, and P. Wanjara, Lap shear strength and fatigue life of friction stir spot welded AZ31 magnesium and 5754 aluminum alloys, Mater. Sci. Eng. A, 2012, accepted.

APPENDIX

LIST OF PUBLICATIONS (over the past two years during my MASc study)

A. Refereed journal papers (accepted or under review):

1) **S.H. Chowdhury**, D.L. Chen, S.D. Bhole, E. Powidajko, D.C. Wechman and Y. Zhou, Fiber laser welded AZ31 magnesium alloy: Effect of welding speed on microstructure and mechanical properties, Metallurgical and Materials Transactions A, Vol 43A, June 2012, pp 2133-2147.
2) **S.H. Chowdhury**, D.L.Chen, S.D. Bhole, X. Cao and P. Wanjara, Lap Shear Strength and Fatigue Life of Friction Stir Spot Welded AZ31 Magnesium and 5754 Aluminum Alloys, Materials Science and Engineering A, 2012, in press, corrected proof, Available online on July 11, 2012.
3) **S.H. Chowdhury**, D.L.Chen, S.D. Bhole, X. Cao and P. Wanjara, Friction stir welded AZ31 magnesium alloy: Microstructure, texture and tensile properties, Metallurgical and Materials Transactions A, 2012, in press, with the proofs corrected on August 16, 2012.
4) **S.H. Chowdhury**, D.L.Chen, S.D. Bhole, X. Cao and P. Wanjara, Lap Shear Strength and Fatigue Behavior of Friction Stir Spot Welded Dissimilar AZ31 Magnesium/AA5754-O Aluminum Alloy with adhesive, under review (internal review).

B. Conference paper:

1) **S.H. Chowdhury**, D.L. Chen, S.D. Bhole, X. Cao, P. Wanjara, E. Powidajko, D. Weckman, and Y. Zhou, Mechanical properties of friction stir welded and fiber laser welded AZ31 magnesium joints, Proceedings of Mg2012 - 9th International Conference on Magnesium Alloys and their Applications (Vancouver, BC, Canada, July 8-12, 2012), edited by W.J.Poole and K.U.Kainer, 2012, pp.821-826.

C. Poster presentations:

1) **S.H. Chowdhury**, D.L. Chen, S.D. Bhole, and Y. Zhou, Fiber laser welded AZ31 magnesium alloy: Effect of welding speed on microstructure and mechanical properties, 12th ASM Ontario Poster Night, University of Toronto, Toronto, Canada, March 08, 2011
2) F.A. Mirza, S.M. Chowdhury, **S.H. Chowdhury**, D.L. Chen, S.D. Bhole, X. Cao, E. Powidajko, D. Weckman, and Y. Zhou, Microstructure and mechanical properties of AZ31 magnesium alloy after different welding processs, *International Workshop on Welding* and Joining of Magnesium Alloys, NSERC-MagNET, University of Waterloo, Waterloo, Ontario, July 28-29, 2011.
3) **S.H. Chowdhury**, F.A. Mirza, V.K. Patel, D. Sarkar and W. Xu, Fatigue and reliability of welded magnesium joints, APMA-AUTO21 Annual Conference, Ottawa, Quebec, May 25-27, 2011.
4) **S.H. Chowdhury**, F.A. Mirza, V.K. Patel, D. Sarkar, B.S. Naik, and W. Xu, Strength improvement of dissimilar welded Joints using novel process, APMA-AUTO21 Annual Conference, Montreal, Quebec, May 29-31, 2012.